OPTIMIZATION AND PARAMETRIC STUDY OF GROUND PENETRATING RADAR WAVE'S RAY-PATH MODELS ON BURIED OBJECTS

HE WENCHAO

PhD

The Hong Kong Polytechnic University

2025

The Hong Kong Polytechnic University

Department of Land Surveying and Geo-informatics

Optimization and Parametric Study of Ground Penetrating Radar Wave's Ray-path Models on Buried Objects

HE Wenchao

A thesis submitted in partial fulfillment of the requirement for the degree of Doctor of Philosophy

August 2024

Certificate of Originality

I hereby declare that this thesis is my own work and that, to the best of my knowledge and belief, it reproduces no materials previously published or written, nor materials that have been accepted for the award of any other degree or diploma, except where due knowledge has been made in the text.

HE Wenchao

Abstract

In densely populated urban environments, the complex network of buried objects, such as pipelines and cables, is indispensable to the daily functioning of the city, supporting everything from basic water supply and waste management to sophisticated communication and power distribution systems. The precision in locating and maintaining these hidden assets is crucial to prevent costly disruptions and facilitate urban planning and development. As a result, efficient and accurate methods for detecting underground structures are essential for minimizing the risk of damage during construction activities and for the timely repair of aging infrastructure. Ground Penetrating Radar (GPR) stands out as an indispensable technology in this field due to its ability to provide detailed insights into the subsurface landscape without the need for physical excavation. Utilizing high-frequency electromagnetic waves, GPR scans the underground to create an image of the subsurface features, reflecting variations in material properties. This technology is particularly effective for identifying the depth and position of buried utilities, assessing their condition, and detecting anomalies such as voids or leaks. Its capability to operate across various soil types and to detect non-metallic as well as metallic objects expands its utility, making GPR an essential tool in the toolkit of urban infrastructure management.

A critical aspect of GPR analysis is the interpretation of hyperbolic reflections, which occur when electromagnetic waves are reflected from cylindrical objects like pipes and cables. The precise analysis of these hyperbolic patterns, through a process known as hyperbolic fitting, is essential for accurately determining the location, depth, and material characteristics of subsurface utilities. Hyperbolic fitting involves adjusting mathematical models to match the curved reflections observed in GPR data, allowing for the estimation of key subsurface parameters. Despite its capabilities, the application of GPR faces limitations due to the absence of unified, quantitative hyperbolic fitting models that can adapt to the varied and complex conditions of urban subsurface environments. The prevalent assumptions of perpendicular survey lines and

homogenous media do not reflect the real-world complexities, leading to inaccuracies in data interpretation and necessitating advanced methodologies to handle non-ideal conditions and incomplete data effectively. This research has advanced hyperbolic fitting techniques for GPR applications, addressing core challenges and expanding the method's utility in complex environments. By incorporating global optimization algorithms and introducing novel methods such as angle-correction and depth-weighted velocity corrections, the thesis has enhanced the accuracy and adaptability of GPR for detecting and analyzing subsurface structures under varied conditions. Furthermore, it has established robust methods for assessing and managing uncertainties in GPR data, effectively bridging the gap between theoretical advancements and practical implementation in urban infrastructure management and archaeological assessments.

This thesis contributed to the GPR research and engineering/surveying community in the following four facets imminently. Firstly, it undertakes a rigorous evaluation of various hyperbolic fitting models, developing strategic recommendations for model selection that adapt to changes in target characteristics such as radius and antenna separation, and demonstrating how variations in subsurface conditions affect GPR data interpretation. Secondly, it introduces angle-corrected hyperbolic fitting models that incorporate pipeline orientation, significantly improving the precision of parameter estimations and extending GPR applicability through validated simulation and field experiments. Thirdly, the study develops a depth-weighted velocity correction algorithm that refines velocity estimations in layered media, addressing the inaccuracies caused by non-homogeneous underground environments. This algorithm has been proven through extensive numerical and laboratory tests to enhance the accuracy of subsurface evaluations. Lastly, the research investigates the impact of hyperbolic data integrity on fitting accuracy, revealing robustness against data alterations and providing empirical insights that guide the handling of incomplete or sparse GPR data. Collectively, this study advances GPR from a basic detection tool to a measurement instrument capable of providing precise measurements in diverse

environmental conditions, enhancing subsurface mapping for archaeological research and civil engineering.

List of Publications

He, W., Lai, W. W. L., Sui, X., & Giannopoulos, A. (2023). Delamination characterization in thin asphalt pavement structure using dispersive GPR data. *Construction and Building Materials*, *402*, 132834.

He, W., & Lai, W. W. L. (2024). Unified optimization-based analysis of GPR hyperbolic fitting models. *Tunnelling and Underground Space Technology*, *146*, 105633.

He, W., & Lai, W. W. L. (2024). Angle-corrected GPR hyperbolic fitting models for improved parameter estimation. *Tunnelling and Underground Space Technology*, *147*, 105741

He, W., & Lai, W. W. L. (2024). Impact of Hyperbolic Integrity on Uncertainties in GPR Measurement using Hyperbolic Fitting. *Journal of Nondestructive Evaluation*, under review.

He, W., & Lai, W. W. L. (2024). Depth-Weighted Velocity Correction: Approach to Hyperbolic Fitting in Multi-Layered GPR Surveys. *Construction and Building Materials*, under review.

Acknowledgment

Completing this PhD has been an enriching journey, made possible by the support and encouragement of many. I am deeply grateful to everyone who contributed to this phase of my academic and personal growth.

First and foremost, I extend my thanks to my supervisor, Prof. Wallace Lai, whose guidance was invaluable throughout this journey. Prof. Wallace Lai not only provided me with the opportunity to pursue my doctoral research but also supported me in mastering the technical skills necessary for my experiments and offered insightful feedback on my research. His patience and comprehensive support have been pivotal in my development as a researcher.

I am also thankful to Prof. Antonis Giannopoulos for his engaging discussions and constructive advice on electromagnetic wave dispersion and GPR numerical simulations. His enthusiasm and approachability made our complex research topics accessible and stimulating.

I am especially thankful to the external examiners, Dr. Craig Warren and Prof. Anja Klotzsche, for their meticulous reviews and valuable participation in my defense. Their insightful comments and constructive criticism have greatly contributed to enhancing the quality of this thesis and have provided me with a deeper understanding of my research area.

A special thanks goes to my senior colleague, Fei Xie, whose pioneering work on GPR hyperbolic fitting laid the groundwork for my thesis. His research was a major source of inspiration and provided a clear direction for my own studies. Additionally, I am grateful to my senior, Tess Luo, for the enriching scientific discussions that greatly benefited my research approach. My appreciation also extends to Sonia. Collaborating with Sonia Santos Assuncao on GPR fieldwork was not only enjoyable but also informative, as I gained numerous practical insights and tips.

I would like to acknowledge my group members—Rene Kwan, Janet Sham, Ray Chang, Fei Xie, Tess Luo, Phoebe Wong, Sahib Singh, Yimin Zhou, Samuel Yu, Lydia Chiu, Alex Cheng, Tom Lau, Marco Lam—for their collaboration and camaraderie, which have made my PhD experience both enjoyable and fulfilling. Their support and friendship have been a constant source of encouragement.

Last but not least, I owe my deepest gratitude to my girlfriend, Rene Kwan, and my family, whose unwavering support and belief in my abilities have sustained me throughout my PhD journey. Their love and encouragement have been my anchor, and I dedicate this achievement to them.

Table of Contents

ABSTRACT **4**

LIST OF PUBLICATIONS **7**

ACKNOWLEDGMENT **8**

TABLE OF CONTENTS **10**

LIST OF FIGURES **14**

LIST OF TABLES **21**

1. CHAPTER 1: INTRODUCTION: **1**

1.1. BACKGROUND 1

1.2. RESEARCH OBJECTIVES AND METHODOLOGY 6

1.2.1. Research Objectives *6*

1.2.2. Research Methodology *7*

1.3. THESIS STRUCTURE 9

2. CHAPTER 2: LITERATURE REVIEW **11**

2.1. CIVIL ENGINEERING APPLICATION OF GPR 11

2.2. BASIC ELECTROMAGNETIC PRINCIPLES 12

2.2.1. Maxwell's Equations *12*

2.2.2. Constitutive Equations *13*

2.3. MATERIAL PROPERTIES 15

2.3.1. Permittivity *16*

2.3.2. Conductivity *19*

2.3.3. Magnetic Permeability *20*

2.4. GPR THEORY 21

2.4.1. GPR Antennas *22*

2.4.2. Types of GPR Waves *24*

2.4.3. GPR Survey *26*

2.4.4. GPR Survey Considerations *27*

2.4.5. Hyperbolic Reflection of Cylindrical Utilities *30*

2.4.6. Basic GPR Signal Processing *31*

2.5. GPR Ray-path Models in Hyperbolic Fitting 33
2.5.1. GPR Ray-path Model 1 (M1) *36*
2.5.2. GPR Ray-path Model 2 (M2) *37*
2.5.3. GPR Ray-path Model 3 (M3) *38*
2.5.4. GPR Ray-path Model 4 (M4) *39*
2.5.5. GPR Ray-path Model 5 (M5) *40*
2.5.6. Summary of Five Models *41*
2.6. Hyperbolic Fitting Algorithm 42
2.6.1. Extraction of Hyperbolic Reflection *42*
2.6.2. Establishment of the Cost Function and Levenberg-Marquardt Nonlinear Least-Squares Solution *43*
2.6.3. Global Optimization for Hyperbolic Fitting *45*
2.7. Finite Difference Time Domain (FDTD) Modelling of GPR 49
3. CHAPTER 3: UNIFIED OPTIMIZATION-BASED ANALYSIS OF HYPERBOLIC FITTING MODELS 52
3.1. Chapter Overview 52
3.2. Historical Development of Hyperbolic Fitting Models in GPR 52
3.3. Evaluation Metric: The Cost Function Value (C-Value) 54
3.4. Numerical Simulations 54
3.5. Laboratory and Field Experiments 66
3.5.1. Laboratory Experiments *66*
3.5.2. Field Experiments *75*
3.6. Summary and Contribution 77
4. CHAPTER 4: ANGLE-CORRECTED HYPERBOLIC FITTING MODELS FOR IMPROVED PARAMETER ESTIMATION 79
4.1. Chapter Overview 79
4.2. Introduction to Angle-Corrected Hyperbolic Fitting 79
4.3. Methodology 80
4.3.1. GPR Measurement and Oblique Angle *80*
4.3.2. Hyperbolic Fitting Model 1 (M1) *81*

4.3.3. Hyperbolic-like Fitting Model 5 (M5) *82*

4.3.4. Establishment of Optimization Problems *82*

4.4. NUMERICAL SIMULATION 84

4.5. FIELD EXPERIMENTS 93

4.5.1. Experimental Setup and Data Acquisition *93*

4.5.2. Hyperbolic Reflection Analysis *96*

4.5.3. Parameter Estimation and Model Performance *96*

4.6. SUMMARY AND CONTRIBUTION 102

5. CHAPTER 5: DEPTH-WEIGHTED VELOCITY CORRECTION: APPROACH TO HYPERBOLIC FITTING IN MULTI-LAYERED GPR SURVEYS 104

5.1. CHAPTER OVERVIEW 104

5.2. INTRODUCTION 104

5.3. METHODOLOGY 105

5.3.1. Extended Common Midpoint Method (XCMP) *106*

5.3.2. Depth-weighted Velocity Correction *109*

5.4. NUMERICAL SIMULATION 110

5.4.1. Single Overlying Layer Cases *111*

5.4.2. Double Overlying Layer Cases *117*

5.5. LABORATORY EXPERIMENTS 120

5.6. SUMMARY AND CONTRIBUTION 125

6. CHAPTER 6: IMPACT OF HYPERBOLIC INTEGRITY ON HYPERBOLIC FITTING IN GPR MEASUREMENT 127

6.1. CHAPTER OVERVIEW 127

6.2. INTRODUCTION 127

6.3. METHODOLOGY 128

6.3.1. Statistical Parameters for Analyzing Hyperbolic Integrity Impact *129*

6.4. NUMERICAL SIMULATION 131

6.4.1. Effects of Hyperbolic Fitting Models and Deletion Methods *132*

6.4.2. Effects of Burial Depth, Relative Permittivity, and Target Radius *135*

6.5. FIELD EXPERIMENT 140

6.6. DISCUSSION 148
6.7. SUMMARY AND CONTRIBUTION 149
7. CHAPTER 7: CONCLUSION 151
7.1. MAIN FINDING 151
7.2. CHALLENGES AND FUTURE WORK 153
REFERENCE 156

List of Figures

Figure 2-1. Conceptual diagram illustrating the process of energy storage/release, charge polarization, and the development of a dipole moment occurring when an EM wave propagates through a material (Jol, 2008). 17
Figure 2-2. When the ground permittivity changes, the patterns change. The TE pattern is shown for permittivities ranging from ice (low) to water (high) (Jol, 2008). 24
Figure 2-3. Propagation of GPR wave in underground layered materials with dielectric contrast (Giannopoulos, 1998). 25
Figure 2-4. GPR wave travel paths of various antenna geometries (Giannopoulos, 1998). 27
Figure 2-5. Illustration of A-scan, B-scan, and C-scan in GPR survey (Kaniewski and Kraszewski, 2023) 29
Figure 2-6. The construction of hyperbolic reflection in underground utility survey by GPR (Xie et al., 2021) 30
Figure 2-7. Radargram with reflections from metal pipes in the sand trench (Xie et al., 2021). 31
Figure 2-8. Possible positions of time-zero in the direct wave of A-scan waveform (Xie et al., 2021b). 33
Figure 2-9. Illustration of GPR signal paths for Model 1. Key parameters are color-coded for clarity: the burial depth (D_0) of the target is shown in red. The TTT at positions x_i (any point along the traverse) and x_0 (directly above the target) is denoted by t_i and t_0, respectively. Here, x_i represents the lateral distance between the antenna and x_0. 36
Figure 2-10. Illustration of GPR signal paths for Model 2. The distance (D_1) between the receiving antenna and the target in purple, and the distance (D_2) between the transmitting antenna and the target in green 37
Figure 2-11. Illustration of GPR signal paths for Model 3. 38
Figure 2-12. Illustration of GPR signal paths for Model 4. 39
Figure 2-13. Illustration of GPR signal paths for Model 5. 40

Figure 2-14. The selection of the hyperbolic pattern. 43
Figure 2-15. (a) Hyperbolic reflections calculated from different parameter combinations and (b) the cost curve of the model. The red dot and arrow indicate the parameter combination of the smallest cost function. 48
Figure 3-1. Hyperbolic reflection picking results and noisy data of the simulation model with varying radius of targets. 58
Figure 3-2. The C-value of different hyperbolic fitting models of simulation models with varying (a) radius of target, (b) antenna separation, (c) buried depth, and (d) relative permittivity. 60
Figure 3-3. Errors in parameter estimation for simulation models with varying radii. Ed – Errors in the estimated depth from raw data; Ed_N – Errors in the estimated depth from data with added noise; Ev – Errors in the estimated wave velocity from raw data; Ev_N – Errors in the estimated wave velocity from data with added noise. The 'noisy data' refers to the original hyperbolic data mixed with additional noise components. 61
Figure 3-4. Errors in parameter estimation for simulation models with varying antenna separation. 62
Figure 3-5. Errors in parameter estimation for simulation models with varying buried depth. 63
Figure 3-6. Errors in parameter estimation for simulation models with varying relative permittivity. 64
Figure 3-7. Computational time (seconds) of the models for all simulation data. Panels: (a) Raw data and (b) noise-added data of separation simulation; (c) Raw data and (d) noise-added data of depth simulation; (e) Raw data and (f) noise-added data of radius simulation; (g) Raw data and (h) noise-added data of permittivity simulation. 65
Figure 3-8. Laboratory experiments setup. 67
Figure 3-9. Radargrams using a 2 GHz GPR system. Here, the number in the lower left corner of each figure represents the experimental number in Table 3-5. 69

Figure 3-10. Radargrams using 900 MHz GPR system. Here, the number in the lower left corner of each figure represents the experimental number in Table 3-5. 69
Figure 3-11. The extracted hyperbolic signatures of all experiments. Note: the number of experiments can be related to Table 3-5. 70
Figure 3-12. The C-value of laboratory experiments. Note: the number of experiments can be related to Table 3-5. 71
Figure 3-13. Errors of parameter estimation of laboratory experiments. 72
Figure 3-14. The comparison between simulation and laboratory experiments. The numerical experiments were set as same as the 18 laboratory experiments. 18 experiments were divided into 6 groups according to the variation of depth from 0.5m to 1.5m. The detailed parameter setting can be seen in Table 3-5. 74
Figure 3-15. Radargram with reflections from metal pipes in the sand trench. 76
Figure 4-1. Illustration of the GPR measurement with the oblique angle. 81
Figure 4-2. Top view of the simulation models and the scanning line. 86
Figure 4-3. Radargrams and corresponding hyperbolic reflection picking results with varying pipe orientations. 86
Figure 4-4. C-value analysis for simulation models with varying pipe radius. For M1: (a) C-value considering pipe orientation; (c) C-value without considering pipe orientation. For M5: (b) C-value considering pipe orientation; (d) C-value with varying target radius, without considering pipe orientation. 87
Figure 4-5. C-value analysis for simulation models with varying buried depth. For M1: (a) C-value considering pipe orientation; (c) C-value without considering pipe orientation. For M5: (b) C-value considering pipe orientation; (d) C-value with varying target radius, without considering pipe orientation. 87
Figure 4-6. Errors in parameter estimation for simulation models with varying radius and pipe orientation. Ea – Errors in estimated pipe orientation; Ed – Errors in estimated depth; Ev – Errors in estimated wave velocity. 90

Figure 4-7. Errors in parameter estimation for simulation models with varying depth and pipe orientation. Ea – Errors in estimated pipe orientation; Ed – Errors in estimated depth; Ev – Errors in estimated wave velocity. 91
Figure 4-8. Geophysical test site at IFSTTAR, Nantes, France..... 94
Figure 4-9. Metal pipe reflections in 1.184 m (a), 1.659 m (b), and 2.395 m (c), from 15° to 90° oblique angles in sand trench. 95
Figure 4-10. Reflections of the metal pipe in 2.395 m at different oblique angles in 270 MHz antenna. 96
Figure 4-11. Errors of parameter estimation of field experiments using 270 MHz antenna. Ea – Errors in estimated pipe orientation; Ed – Errors in estimated depth; Ev – Errors in estimated wave velocity. 99
Figure 4-12. Errors of parameter estimation of field experiments using 400 MHz antenna. Ea – Errors in estimated pipe orientation; Ed – Errors in estimated depth; Ev – Errors in estimated wave velocity. 100
Figure 5-1. Procedure of the proposed method. 106
Figure 5-2. XCMP setup and geometry using two bistatic GPR systems: (a) reflection in a single layer; and (b) reflection and refraction in double layers. 107
Figure 5-3. The simulations cases with a single overlying layer. 112
Figure 5-4. Percentage error in velocity estimations with and without correction across models (a) M1 and (b) M5 for single-layer cases with varying relative permittivity. 115
Figure 5-5. Percentage error in velocity estimations with and without correction across models (a) M1 and (b) M5 for single-layer cases with varying layer thickness. 116
Figure 5-6. Percentage error in depth estimation across models (a) M1 and (b) M5 for single-layer cases. 117
Figure 5-7. The simulations cases with double overlying layers. 118

Figure 5-8. Percentage error in velocity estimations with and without correction across models (a) M1 and (b) M5 for double-layer cases with varying relative permittivity. 120
Figure 5-9. Percentage error in velocity estimations with and without correction across models (a) M1 and (b) M5 for double-layer cases with varying layer thickness. 120
Figure 5-10. Percentage error in depth estimation across models (a) M1 and (b) M5 for double-layer cases. 120
Figure 5-11. Laboratory experiments setup. 122
Figure 5-12. Radargrams of the three scenarios and the extracted hyperbolic reflections. Red lines indicate the interface between asphalt and sand. The yellow line donates the interface of POM and asphalt. 123
Figure 6-1. Original hyperbolic dataset with the datasets post-fifth and tenth deletion iterations utilizing two distinct methodologies for hyperbolic integrity disruption. "Del 1" and "Del 2" denote the first and second methods respectively, while "5th batch" and "10th batch" refer to the deletion of 50% and 95% of the original hyperbolic points, correspondingly. 132
Figure 6-2. Empirical distributions of burial depth and wave velocity using Model 1. 133
Figure 6-3. Empirical distributions of burial depth and wave velocity using Model 5. 134
Figure 6-4. Variation in mean depth and wave velocity, including thrice the standard deviation, across different deletion batches. 135
Figure 6-5. R-squared values derived from parameter estimations at varying levels of data deletion. 135
Figure 6-6. Differential impact on parameter estimates due to variations in burial depth with altered hyperbolic integrity. '1st Dataset' (solid lines): Illustrates the changes in estimated parameters when the burial depth is modified from 0.3m to 0.9m across varying levels of hyperbolic integrity disruption. '2nd Dataset' (dashed lines):

Showcases the changes in estimated parameters with a further increase in burial depth from 0.9m to 1.5m, also across varying levels of hyperbolic integrity disruption. ... 138
Figure 6-7. Differential impact on parameter estimates due to variations in relative permittivity with altered hyperbolic integrity. '1st Dataset' (solid) reflects adjustments from permittivity of 3 to 5, and '2nd Dataset' (dashed) from 5 to 9. ... 139
Figure 6-8. Differential impact on parameter estimates due to variations in object radius with altered hyperbolic integrity. '1st Dataset' (solid) reflects radius adjustments from 0.02m to 0.1m, and '2nd Dataset' (dashed) from 0.1m to 0.3m. ... 139
Figure 6-9. Original hyperbolic data for the metal pipe buried at 2.395 m, alongside datasets after the fifth and tenth deletion iterations, demonstrating two methods of hyperbolic integrity disruption. ... 141
Figure 6-10. Field-derived empirical distributions of burial depth and wave velocity using Model 1. ... 142
Figure 6-11. Field-derived empirical distributions of burial depth and wave velocity using Model 5. ... 142
Figure 6-12. Mean values and thrice the standard deviation of hyperbolic reflections across various deletion batches from field experiment 1. ... 144
Figure 6-13. R-squared values for parameter estimates across different deletion batches from field experiment 1. ... 144
Figure 6-14. Resolution and Residue Length versus Deletion Batch. The resolution, measured in centimeters, represents the spacing between A-scans at different deletion batch and is shown by the bule line and red point. The red line and blue points depict the residue length, also in centimeters, of the remaining hyperbolic sections at different deletion batch. ... 145
Figure 6-15. Empirical distributions of burial depth and wave velocity as estimated using Model 1 in field experiment 2. ... 146
Figure 6-16. Empirical distributions of burial depth and wave velocity as estimated using Model 5 in field experiment 2. ... 147

Figure 6-17. The mean value and corresponding 3 times standard deviation of the hyperbolic reflections at different deletion batches obtained from field experiment 2. 148
Figure 6-18. R-squared of the parameters estimated at different deletion batches obtained from field experiment 2..... 148

List of Tables

Table 2-1. Typical values of relative permittivity (real component) and static conductivity for common subsurface materials at an antenna frequency of 100 MHz (Jol, 2008). 18

Table 2-2. Summary of parameters required for five hyperbolic-fitting methods..... 41

Table 3-1. Simulation models with the varying radius of the target..... 56

Table 3-2. Simulation models with varying antenna separation..... 56

Table 3-3. Simulation models with varying buried depths..... 57

Table 3-4. Simulation models with varying relative permittivity..... 57

Table 3-5. The parameters of laboratory experiments..... 68

Table 3-6. Estimated depth of the five models. 76

Table 4-1. Simulation models varying in target radius..... 85

Table 4-2. Simulation models varying in buried depth..... 85

Table 4-3. Parameter estimation results using 270 MHz GPR. Est. O, Est. D, and Est. V are the estimated pipe orientation Sin(θ), buried depth D, and wave velocity V, respectively. Abs. Err. O and Err. O (%) are the absolute error of the estimation of the pipe orientation Sin(θ), and the corresponding percentage error, respectively. 101

Table 4-4. Parameter estimation results using 400 MHz GPR. 101

Table 4-5. Mean Absolute Error (MAE) of the optimized results. 102

Table 4-6. Root Mean Square Error (RMSE) of the optimized results. 102

Table 5-1. Parameters for single overlying layer simulation cases. Case Num. is the number of the case. P_1 and P_2 are the relative permittivity of layer 1 and the layer enveloping the target, respectively. H_1 and H_2 are the thicknesses of layer 1 and the layer enveloping the target, respectively. 111

Table 5-2. Parameter estimation results of two hyperbolic fitting models in the single layer simulations. Model is the number of the hyperbolic model. The case represents the number of simulation cases (Figure 5-3). Vt is the import value of the EM wave velocity in the layer containing the target. Ve is the bulk velocity estimated by the

hyperbolic fitting and Err_Ve is the corresponding percentage error. CV is the velocity corrected by the proposed method (Equation (3.17)) and Err_CV is the corresponding percentage error. H is the total depth estimated by hyperbolic fitting and Err_H is the corresponding percentage error.....113
Table 5-3. Parameters for double overlying layer simulation cases. Case Num. is the number of the case. P_1, P_2, and P_3 are the relative permittivity of layer 1, layer 2, and the layer enveloping the target, respectively. H_1, H_2, and H_3 are the thickness of layer 1, layer 2, and the layer enveloping the target, respectively. 117
Table 5-4. Parameter estimation results of two hyperbolic fitting models in the double-layer simulations. 119
Table 5-5. Parameters of different layers. H and P are the thickness and relative permittivity of the corresponding material, respectively. 121
Table 5-6. Parameter estimation results of laboratory experiments. Ht indicates the reference value of the burial depth, measured by tape.....125
Table 6-1. Three sets of simulation models with varying burial depth, relative permittivity, and pipe radius. 136

1. Chapter 1: Introduction:

1.1. Background

The underground infrastructure in major urban areas, such as Hong Kong, is characterized by a high density of essential utilities, including water supply lines (Chan et al., 2020; Chen, 2001; Yue and Tang, 2011), sewer systems (Liang et al., 2019a; Liang et al., 2019b), telecommunications cables (Pitt et al., 1999), and electrical conduits (Wan et al., 2009). These utilities are critical for the operation of the city, ensuring the provision of fundamental services and the overall well-being of its inhabitants. Accurate detection and maintenance of these underground networks are paramount to prevent disruptions and hazards (Ellis, 1998; Wallace and Ng, 2016). Rapid urbanization has led to a complex network of underground utilities where old and new infrastructures intertwine, posing significant challenges for urban management. Inaccurate mapping and unplanned excavations can result in severe consequences, such as water supply disruptions (Chan and Ho, 2019), gas leaks (Guo et al., 2004), and telecommunication failures (Tong, 2013), causing substantial economic losses and posing risks to public safety. Effective management and maintenance of these underground systems are crucial to mitigate urban hazards like land subsidence, infrastructure collapse, and flooding. Therefore, accurate estimation of pipe locations and the evaluation of their condition are essential.

The positioning of underground pipelines involves determining both their ground and underground locations. The three-dimensional positioning (x, y, D) of an underground utility consists of horizontal positioning (x, y) and vertical depth (D) estimation. Ground locations can be accurately established using mature surveying methods such as total stations, GPS systems, remote sensing, and LiDAR, all of which require a clear line of sight between the survey equipment and the target. However, for underground pipelines buried within opaque materials like soil, silt, and concrete, determining the vertical depth (D) is more complex as the subjects are out of sight. Methods for locating underground pipelines can be divided into destructive and non-destructive approaches.

Destructive methods, such as excavation, are invasive, time-consuming, costly, and disruptive to urban infrastructure (Forth, 2004). Non-destructive methods, such as using a pipe cable locator (PCL) (Kijima and Hattori, 2016), provide a less invasive alternative for detecting metallic utilities or those with tracing wires, but these methods fall short in EM interference and locating non-metallic underground utilities. The complexities and limitations of these techniques in accurately locating and assessing the condition of underground utilities necessitate further exploration of advanced non-destructive methods.

Ground Penetrating Radar (GPR) offers a powerful non-invasive and non-destructive method for surveying and mapping underground utilities (Daniels, 2004), providing an alternative to more invasive techniques such as excavation. A typical GPR system consists of an antenna, a control unit, and a display monitor (Jol, 2008). The antenna emits electromagnetic (EM) wave signals that penetrate the ground, traveling through various subsurface materials and reflecting off objects with significant dielectric contrasts relative to the surrounding medium. These reflected signals are captured by the receiver in the antenna. The control unit processes these signals by sampling and digitizing the received analog reflections. The system then registers the strength of these reflections at various time intervals, which are used to reconstruct the subsurface images known as radargrams. GPR's ability to detect and image subsurface features without disturbing the ground makes it invaluable for a variety of applications, from locating small rebars in concrete and detecting underground utilities to reconstructing buried stratigraphy and uncovering archaeological remains (Abueladas and Akawwi, 2020; Arosio et al., 2012; Aziz et al., 2016; Booth and Pringle, 2016). Its high resolution, effective data acquisition, and sensitivity to material properties have made GPR a popular choice among the available non-destructive testing methods.

In GPR detection, reflection signals can be categorized into layer reflections and hyperbolic reflections (Ding et al., 2021). Layer reflections occur when EM waves encounter stratified subsurface materials, while hyperbolic reflections are formed when waves are reflected from cylindrical objects such as pipes (Xie et al., 2022; Xie et al.,

2018). Hyperbolic fitting plays a crucial role in interpreting these reflections to accurately determine the location and properties of underground objects. This technique involves the mathematical modeling of the hyperbolic shape of the reflection in the radargram to estimate the depth and material characteristics of the target. The precision of hyperbolic fitting is fundamental for reliable subsurface mapping and utility detection (Cui et al., 2018; Jafrasteh and Fathianpour, 2017; Jaufer et al., 2022; Xie et al., 2021b; Zhang et al., 2016). A typical assumption in GPR measurements is that the survey lines are perpendicular to the linear and cylindrical objects, which results in symmetrical hyperbolic reflections (Dou et al., 2016; Lai et al., 2016b; Tanikawa et al., 2013; Xie et al., 2018). However, if the angle between the survey lines and the pipelines deviates from 90°, the shape of the hyperbolic reflections alters, complicating the interpretation. Additionally, there is an underlying assumption that the detected medium is homogenous, which is often not the case in real-world scenarios (Sagnard, 2017; Sagnard and Tarel, 2016; Wunderlich et al., 2022; Xie et al., 2021a).

The depth of buried objects and EM wave velocity can be estimated by fitting hyperbolic data (Al-Nuaimy et al., 2000; Shihab and Al-Nuaimy, 2005). This involves evaluating the GPR wave propagation velocity in the host material and measuring the two-way travel time (TTT) of the signal at the apex of the hyperbolic reflection. The depth of the target (D) can be calculated using the equation:

$$D = v * \frac{t}{2} \tag{1.1}$$

where v is the GPR wave propagation velocity and t is the TTT. The model of the GPR wave 'ray path' illustrates that when the antenna is not perpendicular to the pipe alignment, the TTT increases, altering the shape of the hyperbolic reflection observed in the radargram. This hyperbolic reflection provides the necessary information to locate underground utilities or any buried cylindrical objects.

Despite the proven efficacy of GPR in subsurface surveys, several significant research gaps in hyperbolic fitting methods still hinder its broader application, particularly in

complex urban settings. First, current models lack a unified, quantitative framework for evaluation, making it challenging to select the most effective method for specific conditions, and thus limiting the precision and reliability of GPR across different scenarios. Second, the conventional assumption that survey lines are perpendicular to pipelines often does not hold true, necessitating innovative methods to accurately account for non-ideal angles frequently encountered in real-world applications. Third, GPR typically assumes that the underground medium is homogeneous; however, most subsurface environments are heterogeneous and layered, which can lead to inaccuracies in estimating the velocity and depth of buried objects. This discrepancy necessitates the development of more sophisticated hyperbolic fitting models that can adapt to varying subsurface conditions. Fourth, factors such as environmental noise, dense utility networks, and signal attenuation often result in incomplete GPR data, introducing significant uncertainties in parameter estimation. These four challenges underscore the need for robust hyperbolic fitting models that can handle incomplete data effectively and provide reliable interpretations. Addressing these gaps under a rigorous physical and mathematical approach is crucial for enhancing the reliability, accuracy, and usability of GPR in complex subsurface environments, thereby improving safety and planning in urban infrastructure management.

Having introduced the fundamental role of GPR in non-destructive underground utility surveying, the structure of this thesis will be outlined next. This thesis is divided into five stages as detailed below.

Following a general introduction to the principles and application of GPR in underground utility detection (stage 1, Chapter 2), in stage 2 (Chapter 3), an extensive comparative analysis of two hyperbolic and three non-hyperbolic fitting models is presented and formulated as a common optimization problem. A value of cost function, the C-value, is introduced to quantitatively evaluate the performance of these models under varying conditions such as antenna separation, target radius, burial depth, and the relative permittivity of the host media. Practical insights and recommendations for

model selection are provided, aimed at enhancing the precision and reliability of both hyperbolic and non-hyperbolic fitting in various GPR studies.

In stage 3 (Chapter 4), a novel method that incorporates an angle correction index into the classical hyperbolic fitting model is developed to estimate the orientation and burial depth of pipes, as well as wave velocity, from the hyperbolic patterns observed in GPR data. This method, which is solved using a hybrid optimization approach combining the Multi-Verse Optimizer (MVO) and Gradient Descent (GD) algorithms, validates two distinct fitting models through numerical simulation and field experiments. The study also evaluates the impact of varying pipe radius and burial depth on the accuracy of parameter estimation at different pipe orientations. This stage offers a comprehensive framework for accurate and efficient parameter estimation, serving as a valuable reference for enhancing data quality in future GPR-based investigations.

Stage 4 (Chapter 5) introduces a depth-weighted velocity correction algorithm designed to improve velocity estimation within layered media. The algorithm adapts to two hyperbolic models based on the availability of target radius and antenna separation information, and its efficacy has been validated through extensive numerical and laboratory experiments. This stage significantly enhances the accuracy of wave velocity estimations, which is crucial for subsurface utility detection beneath complex overlays such as asphalt pavements and tunnel linings, as well as in air-coupled radar applications for extraterrestrial exploration.

In the final stage, stage 5 (Chapter 6), the impact of hyperbolic integrity on the accuracy of GPR fitting methods is investigated. It explores the impact of incomplete data on the accuracy of hyperbolic fitting, employing robust statistical methods to mitigate uncertainties. This stage employs two hyperbolic models to establish optimization problems for fitting hyperbolic data, which were deliberately subjected to two types of alterations: uniform point deletion and biased point removal. Utilizing statistical measures like mean value, standard deviation, and R-squared, a quantitative analysis of the uncertainties introduced by these alterations is conducted. The findings offer

insights into GPR hyperbolic fitting under varied environmental and measurement conditions, contributing to the field's understanding of how burial depth, relative permittivity, and target radius influence the uncertainty associated with hyperbolic integrity.

In summary, this research advances the field of GPR by enhancing hyperbolic fitting techniques for the detection and mapping of linear and cylindrical subjects. The thesis systematically progresses from analyzing various hyperbolic and non-hyperbolic fitting models to addressing practical challenges in real-world GPR applications. The improvements in GPR data processing and analysis presented in this thesis not only enhance the precision of underground utility detection but also pave the way for their broader application in complex urban environments.

1.2. Research Objectives and Methodology

1.2.1. Research Objectives

As outlined in Chapter 1.1, this research aims to enhance the accuracy and reliability of hyperbolic fitting techniques in GPR for detecting underground utilities. The objectives of this research are designed to address specific challenges and gaps identified in the current methodologies, ensuring more precise and reliable subsurface mapping. The research is divided into four main objectives reflecting the stages of the thesis:

(1) Conduct a comprehensive comparative analysis of existing hyperbolic and non-hyperbolic fitting models of common offset GPR wave transmission and reflection in any host dielectric materials and cylindrical objects. This involves formulating these models uniformly and introducing an index to quantitatively evaluate and compare their performance under various conditions.

(2) Develop innovative methods to correct the non-perpendicular alignment of GPR survey lines relative to underground pipelines. This includes integrating an angle correction index into classical hyperbolic fitting models and employing advanced

optimization algorithms to ensure accurate parameter estimation under real-world survey conditions.

(3) Propose and validate a depth-weighted velocity correction algorithm to improve the accuracy of velocity estimations within layered media.

(4) Investigate the impact of data integrity on hyperbolic fitting accuracy. This involves analyzing how the integrity of the hyperbolic reflection affects the estimation of key parameters such as burial depth and wave velocity.

1.2.2. Research Methodology

Research Resources: To ensure the reliability and accuracy of the research findings, the methodology employed comprehensive laboratory and field experiments. Laboratory tests were conducted at the underground utility survey laboratory in The Hong Kong Polytechnic University. The laboratory is equipped with a 5-meter long, 3-meter wide, and 1-meter-deep platform, simulating a controlled subsurface urban environment. This platform houses multiple utilities such as freshwater pipes, saltwater pipes, gas pipes, and power cables, all embedded within soil or sand to simulate real-world conditions. Field experiments were conducted at the geophysical test site at IFSTTAR, Nantes, France. The experimental setup included four trenches filled with different substrates—silt, sand, and two types of gravel—with nominal sizes ranging from 14mm to less than 20mm. Nine pipes were buried in each trench at varying depths, with each trench hosting three groups of pipes: PVC pipes filled with air, water, and three metal pipes.

Instrumentation for both laboratory and field experiments utilized advanced GPR equipment from renowned manufacturers. The setup included a 250MHz antenna from Sensors & Software Inc.; Ground Penetrating Radar Systems, Inc. (GSSI) equipment with antennas capable of 400MHz, 900MHz, and 2GHz frequencies; and IDS GeoRadar's Opera Duo with 200&600 MHz dual frequencies antennas. Data processing and analysis were supported by a comprehensive suite of software tools. Reflexw software is widely used for GPR data processing and visualization, GPRSlice offers

robust data interpretation capabilities, Geolitix provides geospatial analysis, and gprMax is an open-source software that simulates electromagnetic wave propagation. Additionally, MATLAB, a platform for mathematical computing and algorithms, was employed to further analyze the data.

This methodological framework supported a comprehensive analysis of GPR capabilities across different environments and configurations, allowing for both studies and validation studies.

Forward and Backward Methods: The forward study leverages controlled GPR simulations and laboratory experiments to model and understand the subsurface world. Due to the complex and often inaccessible nature of actual subsurface environments, numerical simulations play a crucial role in constructing models that closely replicate real-world conditions. This approach allows for the systematic study of GPR reflections from subsurface objects, helping quantify the relationships between GPR signals and the physical characteristics of the buried targets. Laboratory and simulation experiments serve as crucial platforms for predicting GPR responses under controlled conditions, aiding in the refinement and validation of GPR methodologies and techniques.

Conversely, the backward study focuses on the analysis of hyperbolic reflections from cylindrical targets embedded in various materials. These reflections are used to inversely calculate parameters such as the orientation and depth of targets, hosting material dielectric properties. By fitting these obtained hyperbolic reflections with different hyperbolic models, this research aims to reverse-engineer the data to deduce the characteristics of the subsurface objects. This inverse modeling process is vital for validating the applicability of the forward models and ensuring that the interpretations of GPR data are accurate and reflective of the actual subsurface conditions.

Together, these forward and backward approaches enable the understanding of the GPR-subsurface interaction, enhancing the reliability of GPR applications in different environment.

1.3. Thesis Structure

The thesis is structured into seven chapters, organized to systematically explore and address the objectives laid out in the research. The layout of the thesis progresses from foundational principles through detailed analyses and into practical applications, concluding with a comprehensive summary and future directions.

Chapter 1: Introduction

This initial chapter sets the stage by outlining the research scope, aims, and methodology. It provides justifications for the research focus and lays out the objectives throughout the study.

Chapter 2: GPR Fundamentals

This chapter offers a comprehensive overview of GPR, explaining its fundamental principles and the hyperbolic and non-hyperbolic fitting techniques utilized in evaluating underground utilities (stage 1).

Chapter 3: Comparative Analysis of Hyperbolic Fitting Models

Focusing on the 2nd research stage, this chapter presents an extensive comparative analysis of two hyperbolic and three non-hyperbolic fitting models. It introduces a novel cost function (C-value) to evaluate these models quantitatively, based on different parameters such as antenna separation, target radius, burial depth, and the relative permittivity of the host media. The findings from this study are expected to influence model selection and improve the precision and reliability of GPR studies.

Chapter 4: Correcting Non-Perpendicular Alignment in GPR Surveys

The fourth chapter addresses the 3rd research stage by developing methods to correct for the non-perpendicular alignment between GPR survey lines and underground pipelines. It details a novel approach that integrates an angle correction index into classical hyperbolic fitting models, utilizing advanced optimization algorithms to ensure accurate parameter estimations under real-world conditions.

Chapter 5: Velocity Estimation in Layered Media

In the 4th stage, this chapter introduces a depth-weighted velocity correction algorithm aimed at improving velocity estimations within layered media. This section validates the algorithm through extensive numerical and laboratory experiments, demonstrating its effectiveness in enhancing the accuracy of wave velocity estimations and its adaptability to different subsurface conditions.

Chapter 6: Analyzing the Impact of Data Integrity on Fitting Accuracy

This chapter delves into the 5th stage by examining how hyperbolic reflection integrity affects the accuracy of GPR fitting methods. Using statistical measures, this chapter evaluates the stability of parameter estimations under various conditions of data integrity and explores the influence of burial depth, dielectric constant, and target radius on fitting.

Chapter 7: Conclusion and Future Work

The final chapter summarizes the key findings from each stage of the research and discusses their implications for the field of GPR. It outlines the contributions to urban subsurface surveying, the challenges encountered, and recommendations for future research to further enhance GPR's reliability and utility in complex environments.

2. Chapter 2: Literature Review

2.1. Civil Engineering Application of GPR

The review paper written by W. W. Lai et al. (Lai et al., 2018) summarizes and details various applications of GPR for civil engineering. In the realm of building inspection, GPR is used extensively to explore and assess internal structural components. It is effective in locating embedded features such as reinforcing bars (Liu et al., 2020a; Liu et al., 2020b; Liu et al., 2022; Xu et al., 2013), tension cables (Anderson et al., 2010; Dérobert and Berenger, 2010; Garg and Misra, 2021; Gehrig et al., 2004), and conduits (Church et al., 2019; Church et al., 2020; Ryu et al., 2023), as well as utilities embedded within walls (Amer-Yahia and Majidzadeh, 2012), floors (Miccinesi et al., 2021), and ceilings (Ramírez-Blanco et al., 2008). By identifying these elements, GPR assists engineers and construction professionals in planning renovations and interventions without causing damage to critical structural components (Ristić et al., 2020; ter Huurne et al., 2024; Zajc and Grebenc, 2023). Additionally, GPR can detect areas of moisture intrusion and delamination within the concrete, providing valuable information for maintenance and repair strategies (Agred et al., 2018; Aziz et al., 2016; Bourdi et al., 2012; Liu et al., 2008).

GPR significantly enhances the maintenance and assessment of roads and pavements by providing detailed insights into the layer thickness and subsurface conditions (Loizos and Plati, 2007; Saarenketo and Scullion, 2000). For pavements, it can identify layer thickness (Willet and Rister, 2002), detect subsurface voids (Zhang et al., 2022), and assess the presence of moisture and frost susceptibility which can lead to structural failures if unaddressed (Cao et al., 2022). In bridge inspection, GPR contributes to the assessment of deck degradation (Parrillo et al., 2006), delamination (Janků et al., 2019), and the detection of voids within or beneath the concrete (Pollock et al., 2008), aiding in preventative maintenance measures to extend the lifespan of these critical structures.

GPR's role in the detection and mapping of underground utilities is critical for avoiding accidental utility strikes during excavation, which can lead to costly repairs and hazardous situations (Lai et al., 2018). It allows for the precise localization of pipes, conduits, and wiring, thereby facilitating more efficient utility management and maintenance (Ni et al., 2010). GPR helps in planning construction projects by providing clear mapping of existing utilities, reducing the risk of service interruptions, and enhancing worker safety during digging operations (Conyers, 2016).

In tunnel construction and maintenance, GPR is instrumental in assessing the condition of tunnel liners and surrounding materials (Parkinson and Ékes, 2008; Puntu et al., 2021). It is used to evaluate the thickness of the liner (Li et al., 2011), detect anomalies such as fractures, voids behind the liners (Kravitz et al., 2019), and areas of water ingress (Lin et al., 2020). These capabilities are crucial for ensuring the structural integrity and safety of tunnels, especially in urban environments where aging infrastructure presents ongoing challenges. GPR helps in pre-emptively identifying areas that may require reinforcement or repair, thereby aiding in the systematic maintenance and safety management of tunnel systems.

2.2. Basic Electromagnetic Principles

GPR utilizes EM waves to image and characterize subsurface features. The history of EM theory spans over two centuries and is documented extensively in scholarly texts (Kovetz, 2000). This foundational theory provides the quantitative basis necessary for working with GPR. Maxwell's equations, combined with material constitutive relationships, form the core of the theoretical framework that allows for the quantitative description of GPR signals.

2.2.1. Maxwell’s Equations

Maxwell's equations form the cornerstone of EM theory, providing a comprehensive mathematical framework that describes how electric and magnetic fields interact and propagate. These equations encapsulate the findings of numerous researchers and offer a compact way to understand a wide range of EM phenomena:

- **Faraday's Law of Induction** describes how a changing magnetic field over time induces an electric field. This is mathematically expressed as:

$$\overline{\nabla} \times \overline{E} = -\frac{\partial \overline{B}}{\partial t} \tag{2.1}$$

where E is the electric field vector, and B is the magnetic flux density vector.

- **Ampere's Law with Maxwell's addition** illustrates that electric currents and changes in electric fields produce magnetic fields. This relationship is given by:

$$\overline{\nabla} \times \overline{H} = \overline{J} + \frac{\partial \overline{D}}{\partial t} \tag{2.2}$$

where H is the magnetic field intensity, J is the electric current density vector, and D is the electric displacement vector.

- **Gauss's Law for Electricity** shows the relationship between electric charges and the electric field they produce:

$$\overline{\nabla} \cdot \overline{D} = q \tag{2.3}$$

with ρ representing the electric charge density.

- **Gauss's Law for Magnetism** states that magnetic monopoles do not exist:

$$\overline{\nabla} \cdot \overline{B} = 0 \tag{2.4}$$

These equations are fundamental in deriving the behavior of classical EM phenomena such as induction, radio waves, and resistivity when they are combined with materials' constitutive properties. They serve as the theoretical foundation for understanding and utilizing GPR, by linking EM fields to the electrical properties of the materials they encounter.

2.2.2. Constitutive Equations

Constitutive equations are fundamental in describing how a material responds to EM fields, playing a pivotal role in the practical application of GPR. These equations connect the electrical and magnetic properties of materials to the EM fields described by Maxwell's equations.

For GPR, understanding the electrical conductivity, dielectric permittivity, and magnetic permeability of the materials being surveyed is crucial. These properties are defined by the following constitutive equations:

$$\overline{J} = \tilde{\sigma}\overline{E} \tag{2.5}$$

where J is the current density, σ is the electrical conductivity, and E is the electric field. This equation characterizes how freely charges move under an electric field, contributing to the electrical current.

$$\overline{D} = \tilde{\varepsilon}\overline{E} \tag{2.6}$$

linking the electric displacement field D with the electric field E through the dielectric permittivity ε. This relationship is critical as it describes how charge displacement within a material stores energy when exposed to an electric field.

$$\overline{B} = \tilde{\mu}\overline{H} \tag{2.7}$$

where B is the magnetic flux density, μ is the magnetic permeability, and H is the magnetic field intensity. This equation illustrates how materials respond to magnetic fields, affecting how magnetic fields propagate through different media.

The properties described by these equations are typically treated as constants in simple GPR scenarios, but they can exhibit complex, nonlinear behaviors in more varied conditions. In detailed GPR analyses, the properties might need to be treated as tensor quantities or functions that vary with the electric field and especially under different frequencies.

Moreover, material properties can also demonstrate a dependence on the history of the incident EM field. This history dependence manifests when charges within a material respond at finite rates to changes in the field, appearing fixed under slow field changes and mobile under rapid changes. A more sophisticated representation of Ohm's Law to account for such time-dependent behavior is given by:

$$\overline{J}(t) = \int_{o}^{\infty} \tilde{\sigma}(\beta) \cdot \overline{E}(t-\beta) d\beta \tag{2.8}$$

This expression (Equation (2.8)) should be used when material properties are dispersive, i.e., when they change depending on the frequency of the incident EM field.

For most practical GPR applications, however, simpler models assuming constant scalar values for ε, μ, and σ are sufficient. Particularly important for GPR is the relative permittivity, often termed the dielectric constant (ε_r), defined as:

$$\varepsilon_r = \frac{\varepsilon}{\varepsilon_0} \tag{2.9}$$

where ε_0 is the permittivity of free space, a fundamental physical constant.

2.3. Material properties

Subsurface materials are generally categorized as dielectrics due to their specific electric properties, often termed as ‘dielectric properties.’ The term "dielectric" typically refers to non-conductive materials capable of supporting EM wave propagation by storing and releasing electric field energy without conducting electric current. True dielectrics, such as many crystalline solids, exhibit minimal free charge movement (Landau et al., 2013). However, real-world subsurface environments often contain materials with some level of free charge (from ions in the water in pores, for example), making them what are known as 'lossy dielectrics.' These materials demonstrate varying degrees of EM wave attenuation due to their ability to conduct electricity to some extent (Lowrie and Fichtner, 2020). This conductive property is particularly significant in environments with high salinity or high clay content, where

the presence of free charges leads to substantial EM energy loss during wave propagation, rendering GPR less effective.

2.3.1. Permittivity

Permittivity (ε) is a crucial material property that describes a material's ability to store and release EM energy under the influence of an electric field. It is typically expressed relative to the permittivity of free space (ε_0), known as relative permittivity or dielectric constant (ε_r), where:

$$\varepsilon_r = \frac{\varepsilon}{\varepsilon_0} \tag{2.10}$$

The permittivity of free space is a constant ($\varepsilon_0 = 8.8542\times10^{-12}$ F/m), and the relative permittivity of materials can vary significantly, especially in the presence of water, due to its high permittivity ($\varepsilon_r \approx 80$) and impact on the EM properties of the surrounding material.

The permittivity of materials is frequency-dependent and typically exhibits a complex nature due to the polarization processes involved. In subsurface materials, this complexity is evident with different polarization mechanisms contributing to the overall permittivity, including dipolar and Maxwell-Wagner polarization. For GPR applications, the most relevant is the dipolar polarization, which dominates in the typical GPR frequency range (Figure 2-2).

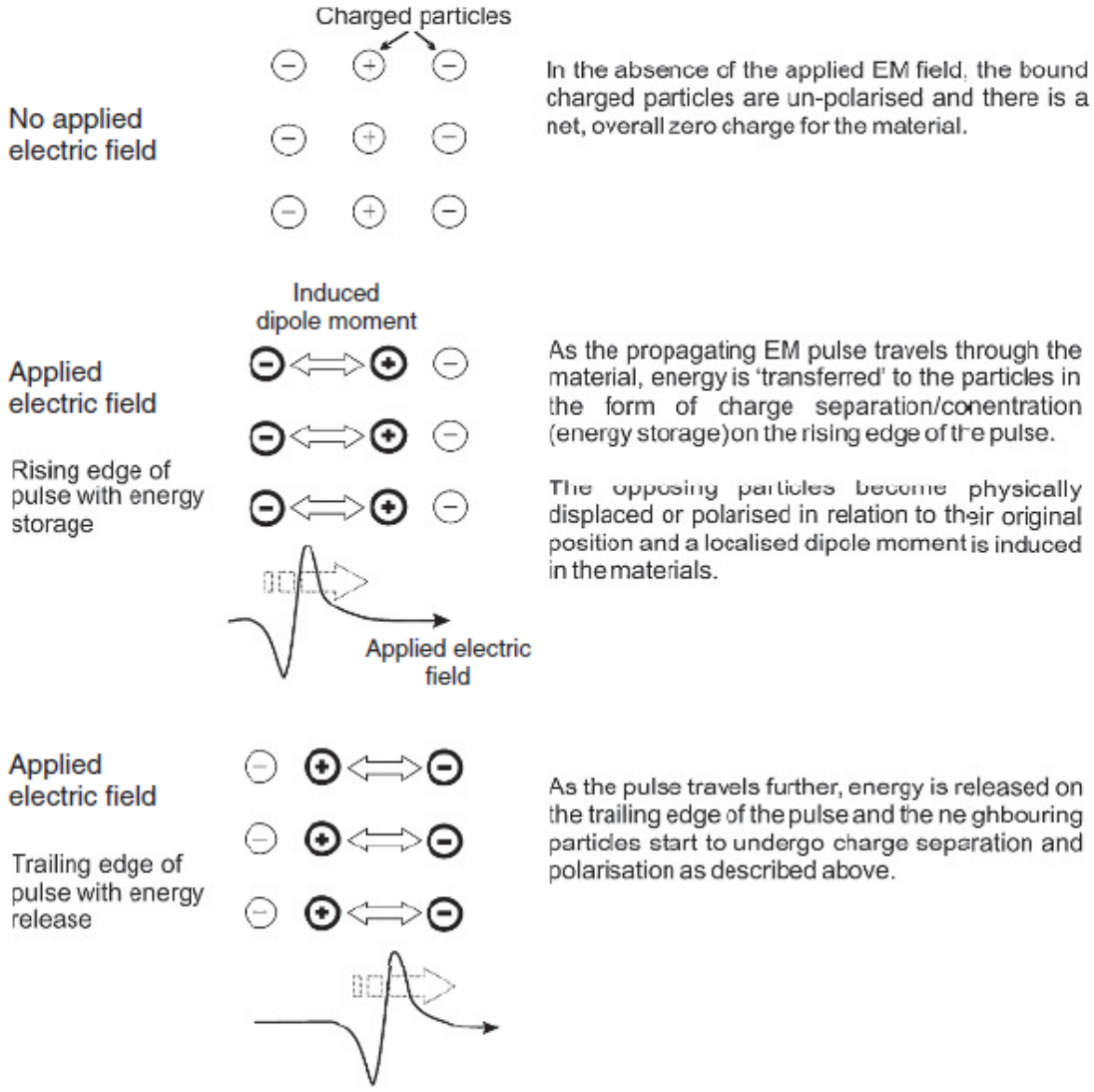

Figure 2-1. Conceptual diagram illustrating the process of energy storage/release, charge polarization, and the development of a dipole moment occurring when an EM wave propagates through a material (Jol, 2008).

Table 2-1 provides typical values of relative permittivity and conductivity for various subsurface materials at a standard GPR frequency of 100 MHz. These values are indicative of how materials respond under specific conditions, showing wide variation based on moisture content and material type—from dry sand to wet clay, each presents unique challenges and responses to GPR surveys.

Table 2-1. Typical values of relative permittivity (real component) and static conductivity for common subsurface materials at an antenna frequency of 100 MHz (Jol, 2008).

Material	Static Conductivity, σ_s (mS/m)	Relative Permittivity, ε_{ave}
Air	0	1
Clay – dry	1–100	2–20
Clay – wet	100–1000	15–40
Concrete – dry	1–10	4–10
Concrete – wet	10–100	10–20
Freshwater	0.1–10	78 (at 25 °C) – 88
Freshwater ice	1–0.000001	3
Seawater	4000	81–88
Seawater ice	10–100	4–8
Permafrost	0.1–10	2–8
Granite – dry	0.001–0.000001	5–8
Granite – fractured and wet	1–10	5–15
Limestone – dry	0.001–0.000001	4–7
Limestone – wet	10–100	6–15
Sandstone – dry	0.01–0.000001	4–7
Sandstone – wet	0.01–0.001	5–15
Shale – saturated	10–100	6–9
Sand – dry	0.0001–1	3–6
Sand – wet	0.1–10	10–30
Sand – coastal, dry	0.01–1	5–10
Soil – sandy, dry	0.1–100	4–6
Soil – sandy, wet	0.1–100	15–30
Soil – loamy, dry	0.1–1	4–6
Soil – loamy, wet	0.1–100	10–20
Soil – clayey, dry	0.1–100	4–6
Soil – clayey, wet	100–1000	10–15
Soil – average	5	16

The conceptual understanding of how EM energy interacts with material properties is illustrated in Figure 2-1. This figure demonstrates the storage and release of energy through the polarization of molecules under the influence of an EM field, depicting the

dynamic nature of the material response to applied EM fields, critical for interpreting GPR data effectively.

2.3.2. Conductivity

Conductivity is defined as the capacity of a material to conduct electric current, which occurs when free charge carriers such as electrons or ions move through the material under the influence of an electric field. In metallic materials, free electrons are the primary charge carriers (Mott, 1936), whereas, in ionic solutions such as those found in subsurface environments, ions act as charge carriers. When an electric field is applied, these ions rapidly accelerate, colliding with other particles, which converts their kinetic energy into thermal energy, manifesting as heat.

Under no external electric field, these charge carriers remain static and do not interact significantly (King et al., 1981). However, when an electric field is applied, the dynamics change drastically. The moving charges gain kinetic energy and, upon colliding with other particles, release this energy as heat, leading to energy dissipation within the material.

The process of conductivity at low frequencies, pertinent to GPR, is generally considered instantaneous. In such cases, conductivity can be quantified using a real, static value, denoted as σ_s in Siemens per meter (S/m), which is commonly reported in the literature. This static conductivity is significant as it directly influences the attenuation of EM waves propagated through the material.

At higher frequencies, the behavior of conductivity becomes more complex due to the phase differences between the applied electric field and the resultant current, introducing an imaginary component of conductivity. This component represents the energy stored in the material's electrical field, which increases with frequency. Despite its importance, in typical GPR frequency ranges, the imaginary component is often neglected, simplifying the conductivity to its real component. This simplification is generally acceptable due to the relatively minor effect of conductivity relaxation

phenomena, particularly in subsurface environments where rapid charge movements are less prevalent.

Nevertheless, different materials exhibit distinct behaviors under varying electric fields due to their unique physical and chemical properties. For instance, in electrolytic solutions, heavy anions and cations respond slowly to changes in the electric field, affecting the overall conductivity. The disparity in conductivity between different materials underlines the necessity of understanding both the real and imaginary components of conductivity for comprehensive subsurface analysis using GPR.

2.3.3. Magnetic Permeability

The magnetic properties of materials, typically categorized as diamagnetic, paramagnetic, or ferromagnetic, generally have minimal impact on GPR operations due to their subtle magnetic effects under normal conditions (Getzlaff, 2007; Jiles, 2015). The permeability, often approximated to the permeability of free space (1.26×10^{-6} H/m), plays a pivotal role only when ferromagnetic materials are involved, significantly affecting GPR wave velocity and signal attenuation. Substances like iron and its oxides are notable for their strong magnetic relaxation phenomena, which are influenced by factors such as electron spin and magnetic domain wall motions. These relaxation processes are predominantly dependent on the size and structure of the magnetic grains and can lead to energy losses similar to those produced by electrical properties under certain conditions.

In practical GPR applications, only substantial amounts of magnetically responsive materials impact the EM response, with materials containing small percentages of ferromagnetic substances (typically less than 2%) generally being considered negligible. However, materials with significant amounts of magnetite or hematite, often found in natural settings like igneous rocks or certain soils, can exhibit relaxation and loss effects on par with permittivity-driven losses. The complexity of magnetic properties in these materials arises from their frequency-dependent nature, with the imaginary component of permeability representing energy loss at varying frequencies.

Figures and empirical data, like those from Mars radar exploration or subsurface magnetic property studies (Gurnett et al., 2008; Ramírez-Nicolás et al., 2016), underline the importance of considering magnetic properties in GPR analyses. These studies reveal that the magnetic characteristics of subsurface materials can influence GPR signal propagation in ways comparable to electrical properties, especially in environments with high concentrations of magnetically active minerals. This makes understanding and incorporating magnetic properties crucial in detailed GPR studies and interpretations, particularly in mineral-rich geological settings. However, in this study, the magnetic properties of the target materials have a minimal impact on the propagation of EM waves from GPR and are therefore neglected.

2.4. GPR Theory

GPR is a sophisticated geophysical method that uses radio waves to probe various low-loss dielectric materials such as soil (Abdelmawla and Kim, 2020; Cui et al., 2021), rock, concrete, and asphalt. Initially developed for natural geologic materials, GPR has expanded its applications significantly, including inspecting man-made structures and various other media. This expansion is partly due to the technology's ability to work across a broad radio frequency spectrum, enabling its application in fields ranging from glaciology to the non-destructive testing of concrete structures. The scale of GPR applications can vary extensively, from exploring vast glacial expanses to assessing the integrity of small-scale concrete infrastructures (Lai et al., 2018).

The operational mechanism of GPR involves emitting radio waves into the ground and measuring the reflections from subsurface features. Typically, a GPR system consists of a transmitter and a receiver that maintain a fixed geometric relationship and are moved over the surface to detect these reflections. In some cases, a method known as transillumination is used, where the focus is on how the transmitted energy is modified by the subsurface materials rather than just the reflections (Foss and Leckenby, 1987). This versatility in measurement approaches allows GPR to be adapted to a wide variety of environments and objectives.

Historically, the use of radio waves for earth examination dates back to the 1950s, with the technology evolving significantly since its inception (Jol, 2008). The foundational physics of GPR is rooted in EM theory, described by Maxwell's equations, which when combined with material constitutive relationships, enable the detailed and quantitative interpretation of GPR data. Over the decades, the applications of GPR have grown exponentially, as has our understanding of its underlying physics and its practical deployment in field settings. Today, GPR is equipped with its own set of terminology and operational procedures, making it a unique and invaluable tool in the field of geophysical surveying.

2.4.1. GPR Antennas

GPR antennas are critical components that create and detect key EM fields necessary for subsurface exploration. The primary function of a transmit antenna is to convert excitation voltage into a predictable spatial and temporal EM field. Conversely, the receive antenna must detect the temporal variations of the EM field and translate it into a recordable signal. The effectiveness of a GPR antenna hinges on several key characteristics (Travassos et al., 2018):

- **Source and Detection Locations**: The source and detection points must be precisely definable to ensure accurate data collection.
- **Transmitter and Receiver Responses**: The antennas must consistently convert electric fields to and from voltages over time and space, requiring invariant responses (transfer functions).
- **Vector Characteristics**: The vector nature of the link between the source voltage and received voltage must be quantifiable, ensuring that the antennas can accurately interpret the direction and magnitude of received signals.

Moreover, the bandwidth of the antennas must align with the system's application needs to ensure efficient signal detection and processing. The design and size of antennas are constrained by the need to match the temporal dynamics of the EM fields they intend

to detect. In practical terms, this means that antenna dimensions should correspond with the rate of change of the exciting field.

Operational Characteristics and Design Limitations:

- **Finite-Size Requirements**: Effective GPR operation necessitates the use of finite-size antennas which, by design, are spatially and temporally distributed. This distribution implies that the exact locations for field creation and detection are somewhat imprecise, which can impact the precision of the data collected.
- **Field Transit Time Variability**: The response of antennas in GPR systems varies depending on the environmental conditions and is not invariant, indicating that adjustments may be necessary based on specific survey conditions.

Efficiency and Directivity:

- Antennas most effective for GPR applications are typically short, resistively loaded electric dipoles. These small dipoles provide a balance between signal reproduction and operational efficiency. The directivity of these antennas changes significantly when placed on the ground, influenced heavily by the ground's permittivity. Figures depicting the antenna patterns on the ground show how the transverse electric (TE) and transverse magnetic (TM) patterns adapt based on the permittivity, demonstrating the complex interaction between the antenna radiation patterns and the ground characteristics (Figure 2-2).

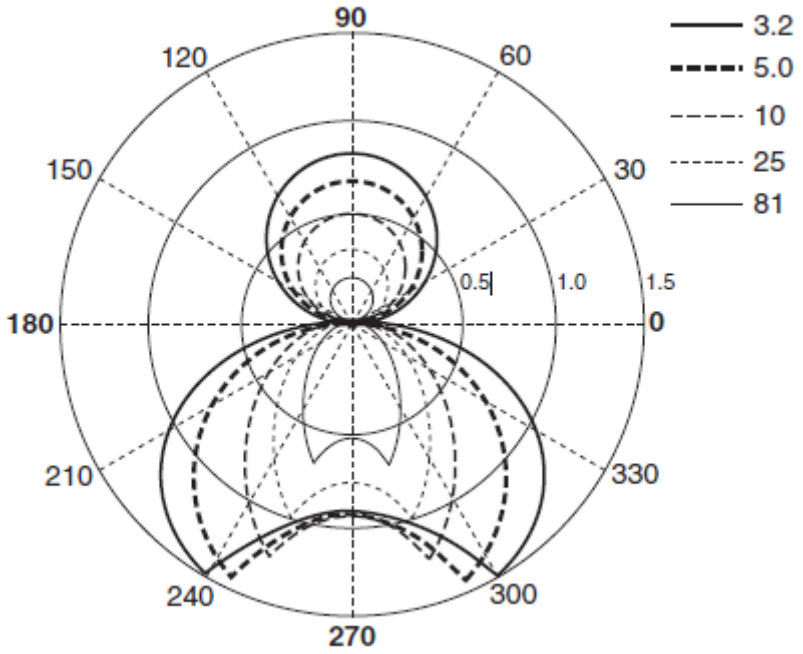

Figure 2-2. When the ground permittivity changes, the patterns change. The TE pattern is shown for permittivities ranging from ice (low) to water (high) (Jol, 2008).

Challenges with Antenna Shielding:

- While shielding can enhance signal focus and reduce noise, it introduces additional complexity. Shielded antennas are common in high-frequency GPR systems where minimizing signal leakage is crucial. However, shields are not perfect and can sometimes interfere with signal clarity, especially in low-frequency applications where antenna size and weight are significant concerns.

In integrating these elements, GPR antennas are designed to maximize the efficacy of subsurface exploration while adapting to the constraints imposed by environmental and operational factors. The design and selection of GPR antennas thus directly impact the quality and reliability of the GPR data collected. In this thesis, only the common offset antenna configuration is used.

2.4.2. Types of GPR Waves

GPR waves interact with their environment in several distinct ways, and these interactions are categorized into different types of waves: air wave, ground wave, refracted wave, and reflected wave, as shown in Figure 2-3.

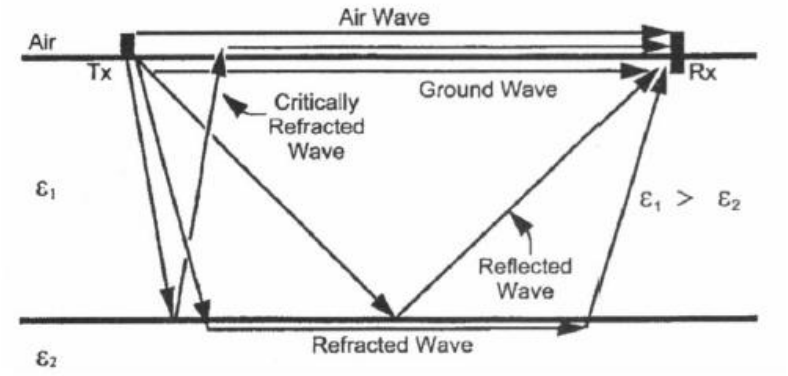

Figure 2-3. Propagation of GPR wave in underground layered materials with dielectric contrast (Giannopoulos, 1998).

Air Wave: The air wave is the initial wave that travels directly from the GPR transmitter to the receiver through the air. It travels at a constant speed of approximately 0.2998 m/ns. Proper shielding of the antenna is essential to mitigate the effects of the air wave, ensuring it does not interfere with the detection of more relevant subsurface signals.

Ground Wave: This wave is generated by the transmission into the ground and is the first wave to penetrate the subsurface materials before reaching the receiver. It's essential for antennas with a small separation between the transmitter and receiver, as their signals may merge at the receiver, appearing as a single direct wave in the radar image.

Refracted Wave: Detected only by specific antenna configurations, such as those set in common mid-point or wide-angle reflection and refraction modes, the refracted wave travels along material boundaries where it encounters changes in material properties.

Reflected Wave: This is the primary wave type utilized in GPR surveys to detect subsurface anomalies. It occurs when the EM wave encounters a boundary between materials with different dielectric properties, causing the wave to bounce back toward

the surface. The strength of the reflected wave is influenced by the relative permittivity of the materials at the interface, calculated using the reflection coefficient formula:

$$Reflection\ Coefficient = \frac{\sqrt{\varepsilon_{r1}} - \sqrt{\varepsilon_{r2}}}{\sqrt{\varepsilon_{r1}} + \sqrt{\varepsilon_{r2}}} \tag{2.11}$$

where ε_{r1} and ε_{r2} represent the relative permittivity of the host and target materials, respectively. This coefficient helps quantify the intensity and phase of the reflected wave relative to the incident wave, with larger differences in permittivity leading to stronger reflections.

These interactions between GPR waves and the materials they encounter are crucial for accurately interpreting subsurface conditions and identifying anomalies within the surveyed area.

2.4.3. GPR Survey

GPR surveys are integral in subsurface exploration, employing various methodologies tailored to specific geophysical needs. Each type of survey has unique configurations and applications, as detailed below:

- Common-Offset Reflection Survey

Common-offset surveys are standard in GPR applications where a single transmitter and receiver are deployed at a fixed separation across each survey location (Berard and Maillol, 2008). This method is known for its simplicity and effectiveness in mapping subsurface reflectivity variations, including changes in material properties and structural boundaries. The data collected with common-offset surveys generally facilitate advanced processing and visualization techniques, enhancing the interpretability of subsurface features. The uniform data spacing, consistent geometry, and straightforward deployment make this technique favored for comprehensive area coverage. This is the survey type adapted in this thesis.

- Multi-offset Common Midpoint (CMP) and Wide-Angle Reflection and Refraction (WARR)

These techniques extend the common-offset method by varying antenna separations to create a detailed velocity profile of subsurface materials. CMP surveys, in particular, stack signals from multiple offsets to improve the signal-to-noise ratio and develop comprehensive cross-sections of subsurface velocity—critical for detailed geophysical investigations (Jacob and Urban, 2016). Meanwhile, WARR surveys offer insights into both the velocity and attenuation properties of the ground materials, similar to seismic refraction techniques (Kaufmann et al., 2020). These methods are more complex and time-consuming but provide valuable data for complex subsurface investigations.

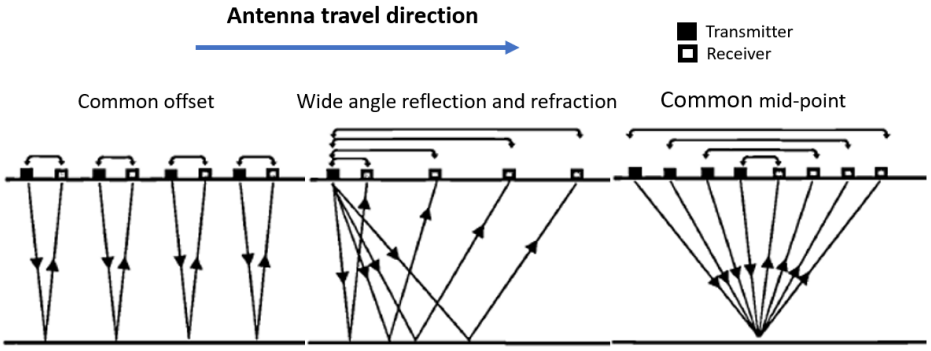

Figure 2-4. GPR wave travel paths of various antenna geometries (Giannopoulos, 1998).

- Transillumination Surveys

Transillumination or borehole GPR measurements are specialized surveys conducted in boreholes or similar confined spaces. These surveys provide detailed cross-sectional images of subsurface conditions and are crucial for studies in complex geological settings where surface GPR surveys might not be effective. The methodology involves transmitting GPR signals across boreholes or between boreholes and the surface, capturing detailed data on subsurface structures and anomalies.

2.4.4. GPR Survey Considerations

Vertical Resolution: Vertical resolution in GPR systems defines the smallest vertical separation at which individual reflectors can be distinguished by the antenna. Typically, this resolution is around a quarter of the wavelength used in the survey, though more accurate systems achieve finer distinctions. The resolution depends on the frequency of

the GPR wave, where higher frequencies provide better resolution due to shorter wavelengths (Reynolds, 2011; Yilmaz, 2001). The equation

$$\lambda = \frac{v}{f\sqrt{\varepsilon_r}} \tag{2.12}$$

where λ is the wavelength, v is the speed of light in vacuum, f is the frequency, and ε_r is the relative permittivity, highlighting how both the operating frequency and the material properties influence vertical resolution.

Horizontal Resolution: The horizontal resolution relates to the system's ability to discern between objects that are side by side and depends on the footprint of the wave emitted by the GPR system, often governed by the First Fresnel Zone. This zone's radius can be estimated with

$$r = \sqrt{\frac{\lambda z}{2} + \frac{(\lambda^2 \varepsilon_r z^2)}{16 f^2}}, \tag{2.13}$$

where z is the depth of penetration (Pérez-Gracia et al., 2008). Like vertical resolution, higher frequencies, and lower permittivity materials enhance the horizontal resolution, allowing closer objects to be distinguished more clearly.

Resolution from System Constraints: GPR data acquisition results in various scan types: A-scan, B-scan, and C-scan, each providing different dimensions of data representation (Figure 2-5). An A-scan provides a single-dimensional depth profile at a point, while a B-scan displays a two-dimensional vertical slice through the subsurface. C-scans offer a top-down view aggregating data from multiple B-scans. The resolution of these scans depends significantly on the digital sampling rate and the methodological setup of the GPR system, which dictates the clarity and precision of the subsurface imaging. The Sampling Theorem is crucial here, suggesting that higher sampling rates can better represent the waveform, improving the accuracy of the data interpretation in the resulting images (Luo et al., 2019).

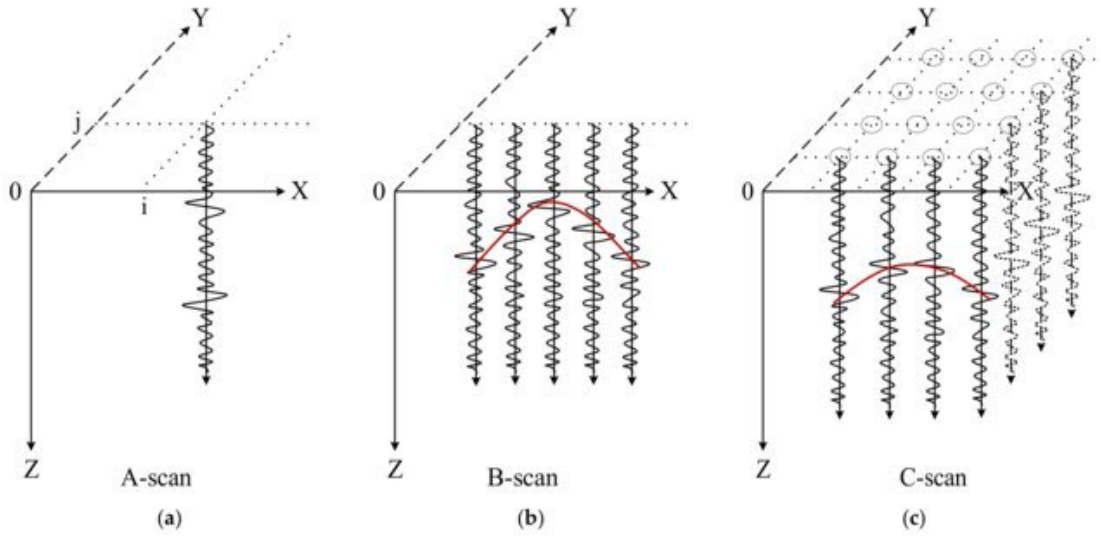

Figure 2-5. Illustration of A-scan, B-scan, and C-scan in GPR survey (Kaniewski and Kraszewski, 2023).

Scattering Attenuation: GPR signals are influenced significantly by the heterogeneous electrical and magnetic properties of the medium they travel through. Small-scale heterogeneities within the medium may not generate strong or detectable signals themselves, but they do affect the transmitted GPR signals by scattering the electromagnetic energy in multiple directions. This scattering, which can be visualized from an energy perspective, results in a decrease in signal intensity as the electromagnetic field scatters off small objects and travels through the medium.

Scattering attenuation, the reduction of signal strength due to these small heterogeneities, is notably dependent on the frequency of the transmitted signal. Higher frequencies often result in greater scattering, which is described by Rayleigh scattering. This type of scattering is crucial to consider because it contributes significantly to the overall attenuation of the GPR signal alongside ohmic or material loss attenuation within heterogeneous lossy dielectric media.

Historically, the significance of scattering effects has been acknowledged early in radar and radio wave applications, particularly in contexts like ice sounding, where volume scattering plays a more pronounced role than ohmic losses in most cases. This understanding underscores the need to account for both ohmic losses and scattering effects when evaluating GPR signal attenuation in varied subsurface environments.

2.4.5. Hyperbolic Reflection of Cylindrical Utilities

The detection of underground utilities with GPR typically involves the use of a common offset antenna configuration. This setup is depicted in Figure 2-4, where the ground-coupled antenna is strategically placed on the surface to transmit EM waves into the subsurface. As these waves traverse through various media—soil, sand, silt, asphalt, concrete—they interact with underground utilities such as pipes and cables.

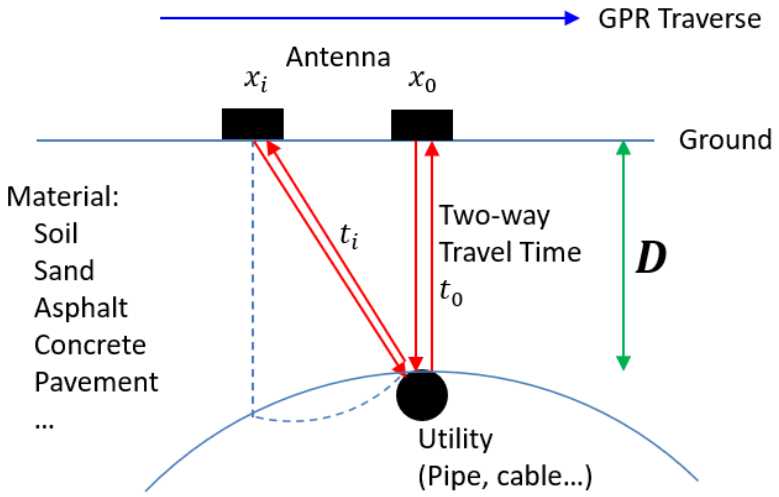

Figure 2-6. The construction of hyperbolic reflection in underground utility survey by GPR (Xie et al., 2021).

When these EM waves encounter cylindrical objects with dielectric properties distinct from the surrounding material, they are reflected back to the surface. The shape of the reflected waveforms often exhibits a hyperbolic pattern on the radargram. This phenomenon occurs because the distance the wave travels increases when the antenna moves away from being directly above the utility, resulting in an increase in the time it takes for the reflection to return to the receiver.

Figure 2-6 illustrates the construction of hyperbolic reflection in underground utility surveys by GPR, showing how the transmitted signals travel through the underground host material and are reflected by utilities. The setup ensures the antenna is at various positions relative to the target utility, providing a comprehensive scan across a predefined GPR traverse.

A typical example of what these hyperbolic reflections look like on a radargram can be seen in Figure 2-7. This radargram was obtained from a 400MHz antenna with reflections captured from metal pipes buried in a sand medium at the IFSTTAR test site in Nantes, France. These reflections are crucial for a range of applications including velocity analysis, depth estimation of underground targets, characterization of underground media, and condition assessment of targets.

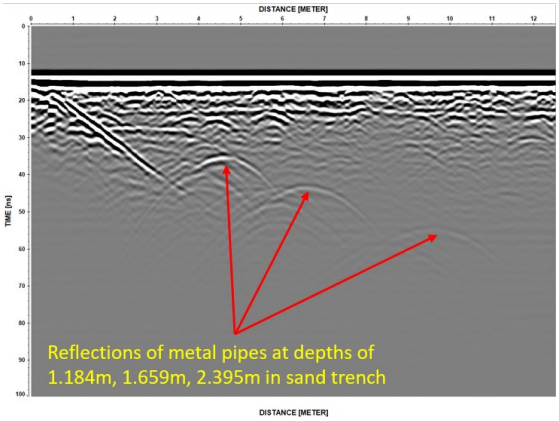

Figure 2-7. Radargram with reflections from metal pipes in the sand trench (Xie et al., 2021).

2.4.6. Basic GPR Signal Processing

Transforming raw GPR data into actionable insights involves several stages of processing, each tailored to enhance specific aspects of the data. This multifaceted approach starts with basic editing to remove errors and extends to advanced processing techniques aimed at refining the data for detailed analysis and visualization.

- **Dewow and Current-shift Removal**

These techniques are employed to remove low-frequency drift (wow) and direct current components in the GPR signal. By stabilizing the baseline of the GPR trace, it enhances the overall readability and reliability of the data. The current shift correction process adjusts the trace to center around a zero mean, effectively balancing variations in signal amplitude caused by environmental or equipment factors.

- **Time-varying Gain**

As GPR signals penetrate deeper, they naturally weaken due to material attenuation. Time-varying gain is applied to increase the amplitude of signals from deeper regions, ensuring that all potential reflections are visible, regardless of depth. This can be managed automatically through algorithms like Automatic Gain Control (AGC) (Pérez et al., 2011), which dynamically adjusts the gain based on the incoming signal strength, or manually, where the operator sets the gain curve to highlight features of interest at various depths.

- **Filtering**

To isolate meaningful data from noise, several filters are used. Bandpass filters focus on frequencies within a specified range, crucial for highlighting relevant geological features while discarding irrelevant noise. High-pass and low-pass filters target spatial inconsistencies, enhancing horizontal or vertical resolution. Median and mean filters smooth out random noise, making the interpretation of GPR data clearer and more accurate.

- **Background Removal**

This process is critical for identifying subtle variations in the GPR data by removing background noise that might obscure key features. It involves calculating the average signal across all traces and subtracting this from each trace, thereby highlighting anomalies and features against a normalized background.

- **Time-zero Correction**

Adjusting the time-zero point on GPR traces corrects for delays introduced by varying surface conditions and initial system settings (Yelf, 2004). This correction ensures that the recorded data accurately reflects the true timing of the reflected signals, which is essential for precise depth calculation and analysis. The possible positions for the time-zero are shown in Figure 2-8. In this thesis, the peak point (point E) is adopted as the position of time-zero.

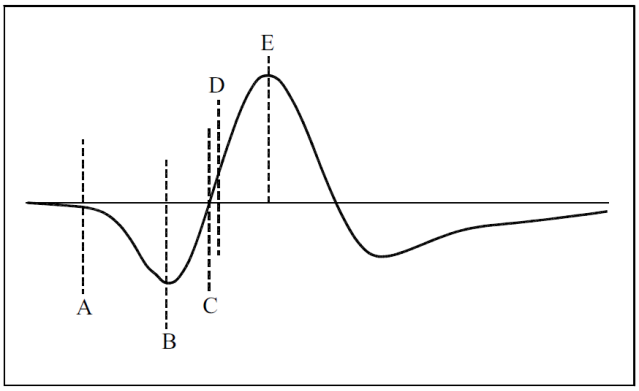

Figure 2-8. Possible positions of time-zero in the direct wave of A-scan waveform (Xie et al., 2021b).

2.5. GPR Ray-path Models in Hyperbolic Fitting

Building on the foundational concepts covered in the preceding section 2.4, which detail the operational principles, equipment, and methodologies integral to GPR technology, we transition into a more focused exploration of hyperbolic reflection models in GPR analysis. This segment, section 2.5, delves into the mathematical and physical modeling of hyperbolic reflections, which are crucial for accurately estimating the depth of burial, EM wave velocity, and permittivity of the medium around cylindrical targets such as pipes and cables. By applying refined hyperbolic fitting techniques to the measured data, this section aims to enhance the precision and reliability of subsurface investigations, providing essential insights into the characteristics and conditions of buried utilities and other cylindrical objects.

In the context of GPR analysis, the curves produced when scanning cylindrical targets such as pipes are often referred to by various terms—hyperbolas, curves, diffractions, or hyperbolic reflections. For clarity and consistency, this thesis will use the term "hyperbolic reflections" to describe these characteristic curves. Additionally, the mathematical models that describe these curves have been given different names in the literature, including GPR ray-path models, GPR reflection models, or simply hyperbolic or hyperbola models. To distinguish these mathematical formulations from the actual measured curves, we will consistently refer to them as GPR ray-path models in this work. Some of these models can be expressed in the form of hyperbolic equations, which we will categorize as hyperbola models, while others that do not fit this form

will be referred to as non-hyperbola models. This distinction sets the stage for the detailed exploration of these models in the following sections. For convenience, the process of fitting hyperbolic reflections using different GPR ray-path models will be collectively referred to as hyperbolic fitting.

Beyond the specific application to underground pipelines, GPR can effectively detect a variety of cylindrical and elliptical structures across diverse environments. This includes scanning rebar within concrete, identifying boulders beneath the earth's surface, mapping tree roots, or exploring geological formations on other planets. These scenarios all generate hyperbolic reflections similar to those observed with pipelines due to their rounded cross-sectional profiles when intersected by GPR waves. The hyperbolic fitting techniques discussed in this thesis, while focused on pipelines, are equally applicable to these varied contexts. The adaptability of these algorithms allows them to be applied directly to any scenario where the target exhibits a circular or elliptical geometry relative to the radar's scanning plane, thus broadening the scope of GPR applications in both terrestrial and extraterrestrial explorations.

The application of deep learning in GPR data analysis has significantly enhanced the detection and interpretation of subsurface features. Techniques such as Faster R-CNN (Lei et al., 2019), CNN-LSTM (Lei et al., 2020), and SSD (Liu et al., 2020) have streamlined the identification and localization of hyperbolas, traditionally a manual and time-consuming process. These methods automate the extraction of key data, improving accuracy and reducing processing time for on-site analysis. Notably, the integration of Generative Adversarial Networks (GANs) (Zhang et al., 2021) and YOLOv4 (Li et al., 2022) showcases the ability to handle complex datasets efficiently, even under challenging conditions like noise and data scarcity. By reducing computational demands and supporting real-time applications, deep learning is proving indispensable in advancing subsurface exploration and utility mapping.

Significant advances in full-waveform inversion (FWI) approaches for GPR also have been documented in the literature. As early as 1996, a FDTD model was developed to

simulate GPR detection of cylindrical targets, showing good correlation with experimental results (Bourgeois and Smith, 1996). This approach was further refined with the introduction of efficient pseudospectral time-domain (PSTD) algorithms in 1999, which significantly reduced the number of unknowns required in FDTD methods (Liu and Fan, 1999). Subsequent improvements in FDTD algorithms have consistently demonstrated robust performance in field and synthetic tests (Fan and Liu, 2000; Gürel and Oğuz, 2000). The integration of FDTD with particle swarm optimization (PSO) has enabled precise localization of subsurface cylindrical objects at varying depths (Matriche et al., 2014). Additionally, the application of frequency-domain FWI, using specialized frequency strategies, has effectively enhanced inversion efficiency, allowing simultaneous inversion of permittivity and conductivity to accurately reconstruct the shape and location of inclusions (Jazayeri et al., 2018). Innovations such as the use of the PEST algorithm (model-independent parameter estimation and uncertainty analysis) have further refined the precision in estimating pipeline diameters and identifying infill materials like air or water. More recently, a novel FWI approach employing a 3D FDTD forward-modeling program coupled with the shuffled complex evolution (SCE) technique has been developed, facilitating reliable parameter extraction and significantly broadening the adaptability of FWI in GPR applications (Liu et al., 2018). The advent of machine learning integrated FWI techniques promises even greater computational efficiency and application scope in scenarios such as rebar positioning within concrete, surpassing traditional electromagnetic solvers in real-time capabilities (Giannakis et al., 2019; Patsia et al., 2023a, b).

2.5.1. GPR Ray-path Model 1 (M1)

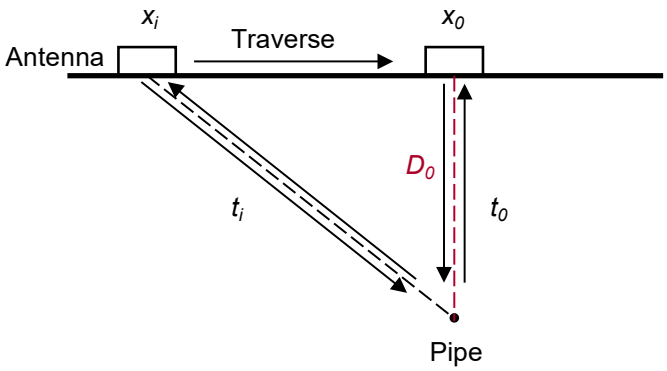

Figure 2-9. Illustration of GPR signal paths for Model 1. Key parameters are color-coded for clarity: the burial depth (D_0) of the target is shown in red. The TTT at positions x_i (any point along the traverse) and x_0 (directly above the target) is denoted by t_i and t_0, respectively. Here, x_i represents the lateral distance between the antenna and x_0.

This model is depicted in Figure 2-9. In this simplistic approach, the separation between the transmitter and receiver antennas is not considered, and the buried cylindrical target is regarded as a point source. The geometry of the scenario allows for the establishment of Equation 1 through basic trigonometry:

$$t_i = \frac{2\sqrt{D_0^2 + x_i^2}}{v}, \tag{2.14}$$

where v is the EM wave velocity in the host material, D_0 is the burial depth of the object, x_i is the distance between the antenna at position i and at the apex of the object, and t_i represents the corresponding two-way travel time at position i.

The equation (2.14) can also be expressed in the form of hyperbolic equations:

$$\left(\frac{vt_i}{2D_0}\right)^2 - \left(\frac{x_i}{D_0}\right)^2 = 1. \tag{2.15}$$

The popularity of this model is largely due to its simplicity and computational efficiency, which has led to its widespread adoption in commercial processing software. Furthermore, it does not require prior knowledge such as antenna separation or target radius, making it applicable in a wide range of scenarios. Common practice involves constructing a mathematical model of the hyperbola using Equation 1 with a given

velocity value and then manually adjusting the model to align with the curved reflection in the data. This alignment process, often referred to as the 'drag-and-overlap' procedure, relies heavily on the operator's experience. As such, it can be subjective and potentially introduce bias, which may undermine the reliability of the survey results.

2.5.2. GPR Ray-path Model 2 (M2)

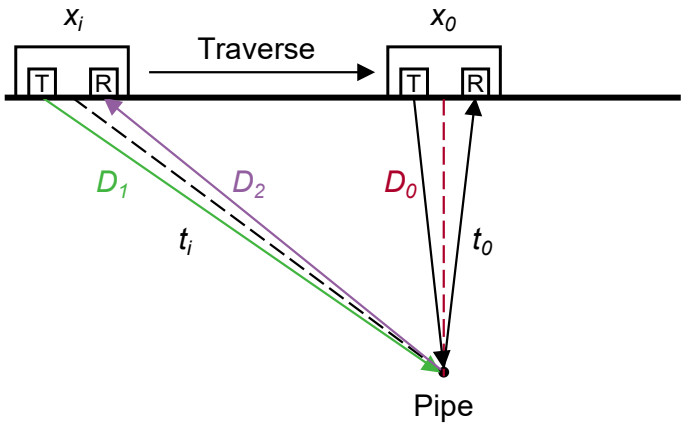

Figure 2-10. Illustration of GPR signal paths for Model 2. The distance (D_1) between the receiving antenna and the target in purple, and the distance (D_2) between the transmitting antenna and the target in green

In contrast to Model 1, Model 2 (as shown in Figure 2-10) accounts for the separation between the transmitter and receiver antennas. This addition helps mitigate uncertainties arising from antenna separation. The TTT in this model can be expressed as:

$$t_i = \frac{D_1 + D_2}{v}. \tag{2.16}$$

These distances can be calculated using Pythagoras theorem

$$D_1 = \sqrt{(x_i + S)^2 + D_0^2}, \tag{2.17}$$

$$D_2 = \sqrt{(x_i - S)^2 + D_0^2}. \tag{2.18}$$

Here, S represents half the separation between the transmitter and receiver antennas.

This model is particularly beneficial when using low-frequency GPR antennas to locate underground utilities. Since the separation between antennas increases with lower frequencies and may approach the depth of the targets, accounting for this separation is critical. However, Model 2 still neglects the radius of the targets, which can result in inaccuracies under conditions where the radius is comparable to the depth.

2.5.3. GPR Ray-path Model 3 (M3)

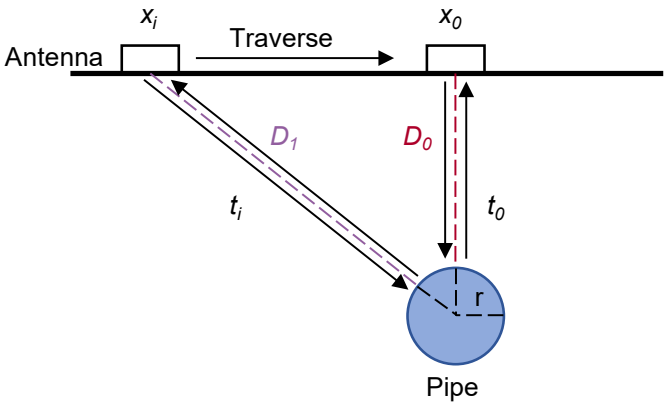

Figure 2-11. Illustration of GPR signal paths for Model 3.

Some researchers have sought to enhance Model 1 by incorporating the radius of cylindrical targets while still treating the GPR antenna as a point source. This adaptation, illustrated in Figure 2-11, has been shown to be particularly beneficial when the target radius is substantially larger compared to its depth (Sham and Lai, 2016b). The modified model can be expressed as follows:

$$t_i = \frac{2D_1}{v}, \tag{2.19}$$

$$D_1 = \sqrt{x_i^2 + (D_0 + r)^2} - r, \tag{2.20}$$

where r signifies the radius of the target.

The equations (2.19) and (2.20) can also be expressed in the form of hyperbolic equations:

$$\left[\frac{t_i v + 2r}{2\left(D_0 + r\right)}\right]^2 - \left(\frac{x_i}{D_0 + r}\right)^2 = 1. \tag{2.21}$$

Despite the improved accuracy in certain scenarios, Model 3 may still exhibit inaccuracies when the antenna separation significantly affects the radar signal's path. Additionally, as this model requires prior knowledge of the target's radius, it may not be suitable when such information is unavailable.

2.5.4. GPR Ray-path Model 4 (M4)

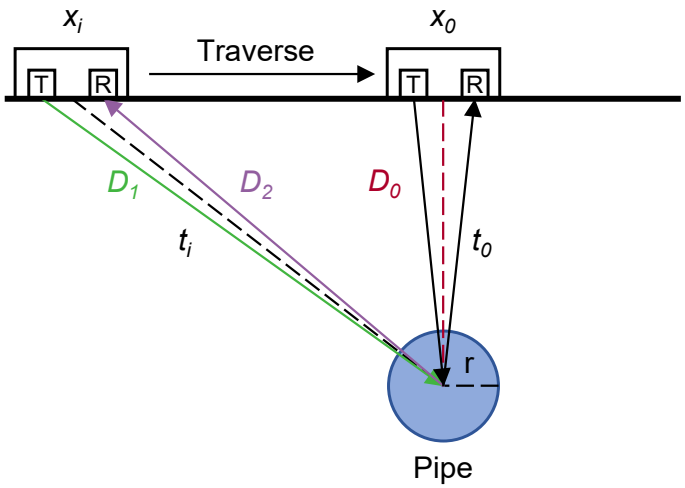

Figure 2-12. Illustration of GPR signal paths for Model 4.

Model 4, depicted in Figure 2-12, is a more comprehensive approach that accounts for both antenna separation and target radius. Furthermore, this model assumes the reflection point to be at the center of the target. The equations representing this model are:

$$t_i = \frac{D_1 + D_2 - 2r}{v}, \tag{2.22}$$

$$D_1 = \sqrt{\left(x_i + S\right)^2 + \left(D_0 + r\right)^2}, \tag{2.23}$$

$$D_2 = \sqrt{\left(x_i - S\right)^2 + \left(D_0 + r\right)^2}. \tag{2.24}$$

While this model is a significant improvement over Model 2, it is computationally more demanding due to the increased complexity. This may pose challenges for real-time applications with limited computational resources.

2.5.5. GPR Ray-path Model 5 (M5)

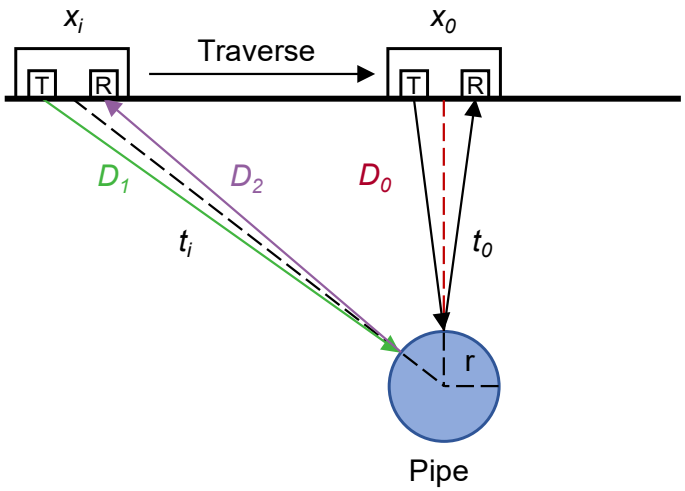

Figure 2-13. Illustration of GPR signal paths for Model 5.

Model 5 is an extension of Model 3 that takes into account antenna separation. Different from Model 4, Model 5 assumes the reflection point to be at the intersection of the antenna midpoint and the target centerline with the target surface (Figure 2-13). The equations for this model are:

$$t_i = \frac{D_1 + D_2}{v}, \tag{2.25}$$

$$D_1 = \sqrt{\left[\left(D_0 + r\right) - \frac{\left(D_0 + r\right)r}{\sqrt{\left(D_0 + r\right)^2 + x_i^2}}\right]^2 + \left[x_i - \frac{x_i * r}{\sqrt{\left(D_0 + r\right)^2 + x_i^2}} - S\right]^2}, \tag{2.26}$$

$$D_2 = \sqrt{\left[\left(D_0 + r\right) - \frac{\left(D_0 + r\right)r}{\sqrt{\left(D_0 + r\right)^2 + x_i^2}}\right]^2 + \left[x_i - \frac{x_i * r}{\sqrt{\left(D_0 + r\right)^2 + x_i^2}} + S\right]^2}. \tag{2.27}$$

This model is even more computationally intensive than Model 4, which may limit its feasibility for real-time applications.

2.5.6. Summary of Five Models

Table 2-2 summarizes the characteristics and parameters considered by each of the five hyperbolic fitting models discussed above. At the outset of the discussion on the five models, it's important to note a key difference between traditional hyperbola fitting and the non-hyperbola fitting methods used in this study. M1 and M3, which do not account for antenna separation, can be translated into standard hyperbola equations. The process of estimating parameters through these equations constitutes traditional hyperbola fitting. On the other hand, M2, M4, and M5, which do consider antenna separation, don't exactly fit the traditional hyperbola but rather describe a curve that approximates the shape of a hyperbola. These models cannot be transformed into standard hyperbola equations and hence represent non-hyperbola models, distinct from the traditional approach.

Table 2-2. Summary of parameters required for five hyperbolic-fitting methods.

Parameters	Hyperbolic Fitting model				
	M1	M2	M3	M4	M5
Antenna separation (S)	N	I	N	I	I
Target radius (r)	N	N	I	I	I
Reflection-point position	-	-	Surface	Centre	Surface

Note: I – Input as priori information; N – Neglected.

Except for Model 1, the other models require information on antenna separation or target radius to enhance the accuracy of parameter estimation. The requirement of this information, however, restricts the applicability of these models. While antenna separation can easily be obtained from equipment specifications, the radius of buried targets might not always be available, which increases the uncertainty of survey results.

2.6. Hyperbolic Fitting Algorithm

Having established a robust framework for modeling hyperbolic reflections in GPR data through various ray-path models, the next crucial step involves the extraction of these reflections and their subsequent analysis using fitting algorithms. Reflection extraction serves as a foundational stage, where we systematically isolate the hyperbolic patterns from raw GPR data, a process pivotal for accurate parameter estimation. This extraction not only ensures the clarity and reliability of the data fed into the fitting algorithms but also enhances the precision of the depth estimation, wave velocity, and medium permittivity calculations. Subsequently, the section on fitting algorithms delves into the methodologies for parameter estimation—ranging from the traditional Nonlinear Least Squares with its Levenberg-Marquardt solution to more robust global optimizers like Particle Swarm Optimization (PSO). These fitting techniques build upon the clean, well-defined inputs generated by the reflection extraction process, providing a comprehensive approach to interpreting GPR data for subsurface evaluations.

2.6.1. Extraction of Hyperbolic Reflection

In the process of analyzing GPR data, the accurate extraction of reflection events from subsurface objects is paramount. This involves isolating specific hyperbolic reflections, which are indicative of cylindrical utilities such as pipes or cables. Initially, the apex of these hyperbolic reflections, which corresponds to the point of shortest TTT, is identified within the radargram. This apex represents the direct overhead position of the buried object relative to the GPR antenna. The critical time, t_0, is then determined by calculating the difference between the established time-zero—marking the start of the GPR signal's journey—and this shortest TTT, thus pinpointing the precise moment the signal reflects off the target.

This selection process is crucial as it focuses on the most pronounced part of the reflection, providing a clear starting point for further analyses. The accurate identification of this point facilitates the subsequent stages of signal processing and

parameter estimation. An example of this selection is depicted in Figure 2-14, illustrating a systematic approach to identifying and isolating hyperbolic patterns within the radargram.

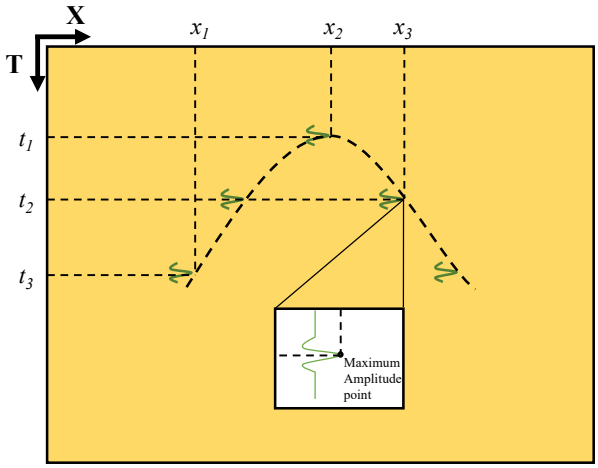

Figure 2-14. The selection of the hyperbolic pattern.

2.6.2. Establishment of the Cost Function and Levenberg-Marquardt Nonlinear Least-Squares Solution

For a given set of parameters [D_0, v], synthetic TTT, denoted by t_i, is computed through various hyperbolic fitting models. These models translate the fitting challenge into an optimization problem, aiming to identify the parameter set [D_0, v] that reduces the sum of squared discrepancies between the observed TTTs, T_i, and the predicted TTTs, t_i. Formally, this optimization task seeks to minimize:

$$\arg\min \sum_{i=1}^{n} \left(T_i - t_i\right)^2, \tag{2.28}$$

where n represents the number of equations formulated for the parameters (D_0, v), utilizing known pairs (x_i, t_i). The least squares method can be applied to solve this set of equations, refining the parameter estimates towards optimal values.

- General Least Squares Approach

The fundamental concept in least squares estimation is to minimize the overall error between the predicted and observed values. In the context of hyperbolic fitting for GPR,

this involves adjusting the parameters of the hyperbolic reflections to best fit the data points collected from subsurface reflections. Mathematically, the objective function or cost function for a least squares problem is defined as:

$$x = \underset{x}{\operatorname{argmin}}\{F(x)\}, \tag{2.29}$$

$$where\ F(x) = \frac{1}{2}\sum_{i=1}^{n}\left(f_i(x)\right)^2, \tag{2.30}$$

where $f_i(x)$ are the residual functions for each observation, representing the difference between the observed values and those predicted by the model. The goal is to find the parameter set x that minimizes $F(x)$, effectively minimizing the sum of the squares of the residuals.

- Levenberg-Marquardt Solution

To refine this approach, the Levenberg-Marquardt method augments the traditional least squares by introducing modifications that enhance robustness and convergence speed, particularly for non-linear models encountered in hyperbolic fitting. It starts by approximating the cost function using a first-order Taylor expansion around the current estimate:

$$f(x+h) \approx f(x) + J(x)h, \tag{2.31}$$

where $J(x)$ is the Jacobian matrix of partial derivatives of the residual functions, and h is the step vector in parameter space. This formulation leads to an approximate model for the cost function:

$$F(x+h) \approx \frac{1}{2}(f(x) + J(x)h)^T(f(x) + J(x)h). \tag{2.32}$$

The quadratic approximation of the cost function allows for solving the parameter updates efficiently using the following update rule derived from setting the gradient of $F(x+h)$ with respect to h to zero:

$$(J^T J + uI)h = -J^T f. \tag{2.33}$$

Here, u is the damping factor that controls the influence of the gradient descent and Gauss-Newton method components, providing a means to navigate the balance between convergence speed and stability.

Additionally, Xie et al. have extended the traditional LM solution method by introducing constraints, leading to the development of the CLS (Constrained Least Squares) solution (Xie et al., 2021a). This enhancement further improves the precision of parameter estimation using least squares fitting for hyperbolic reflections.

2.6.3. Global Optimization for Hyperbolic Fitting

In the realm of hyperbolic fitting for GPR data analysis, traditional methods such as the LM algorithm have been widely utilized due to their efficiency in handling well-behaved mathematical models. However, these least squares methods often struggle with convergence issues when the model assumptions do not hold perfectly or when the parameter landscape is complex and fraught with local minima.

To address these challenges, alternative approaches involving global optimization techniques have been explored. These methods do not rely on the gradient descent principle alone but employ a broader search strategy to navigate the entire solution space. This is particularly useful in scenarios where the objective function, such as the sum of squared differences between observed and predicted travel times outlined in Equation (2.28), is non-convex or has multiple feasible solutions.

By deploying global optimizers, or a combination thereof, one can directly search for optimal values of burial depth (D) and wave velocity (v), thus potentially achieving more robust and reliable fitting results even in complex subsurface conditions. The following discussion delves into various global optimization strategies such as gradient descent (GD), particle swarm optimization (PSO), and genetic algorithms (GA), which offer distinct advantages in terms of exploration capabilities and resilience against getting trapped in local optima.

- Gradient descent (GD)

Gradient descent (GD) is an iterative optimization algorithm used to minimize a cost function, typically employed in situations where the solution space is multidimensional and complex. It is especially useful in applications like fitting GPR hyperbola and non-hyperbola reflections.

In the context of hyperbolic fitting, the objective function to be minimized can be expressed as:

$$J(D,v)=\sum_{i=1}^{n}(T_i-t_i)^2, \tag{2.34}$$

where T_i represents the actual travel times measured by GPR, and t_i are the predicted travel times based on the hyperbolic model with current estimates of D and v.

The gradient descent updates the parameters iteratively according to the formula:

$$D_{new}=D_{old}-\alpha\frac{\partial J}{\partial D}, \tag{2.35}$$

$$v_{new}=v_{old}-\alpha\frac{\partial J}{\partial v}, \tag{2.36}$$

where α is the learning rate—a crucial parameter that determines the step size of each update. This rate must be chosen carefully; too large a rate can lead to overshooting the minimum, while too small a rate may result in a slow convergence.

The partial derivatives $\partial J/\partial D$ and $\partial J/\partial v$ represent the gradients of the cost function with respect to the depth and velocity, respectively. Calculating these gradients involves evaluating how the small changes in D and v influence the prediction error across all data points.

- Particle Swarm Optimization (PSO)

Particle Swarm Optimization (PSO) is a robust, population-based optimization algorithm inspired by the social behavior of birds flocking or fish schooling (Kennedy

and Eberhart, 1995). It's particularly effective for optimizing complex nonlinear functions like those involved in hyperbolic fitting in GPR data analysis.

In PSO, each "particle" in the swarm represents a potential solution to the optimization problem, characterized by parameters such as D and velocity v in the context of GPR. Each particle adjusts its position in the search space by combining some aspect of its personal best position with the best position found by the swarm as a whole.

The position update rules for each particle can be expressed as follows:

Velocity Update:

$$v_i^{(t+1)} = \omega v_i^{(t)} + c_1 r_1 (p_i - x_i^{(t)}) + c_2 r_2 (g - x_i^{(t)}). \tag{2.37}$$

Position Update:

$$x_i^{(t+1)} = x_i^{(t)} + v_i^{(t+1)}. \tag{2.38}$$

Here:

$v_i^{(t)}$ and $x_i^{(t)}$ are the velocity and position of the i^{th} particle at iteration t.

p_i is the personal best position of the i_{th} particle.

g is the global best position found by any particle in the swarm.

ω is the inertia weight that controls the impact of the previous velocity on the current one, helping to balance global and local exploration.

c_1 and c_2 are acceleration coefficients influencing the cognitive and social components respectively, with r_1 and r_2 being random numbers between 0 and 1.

This approach effectively explores the solution space by encouraging individual particles to explore new areas while also converging towards promising regions identified by the swarm. This dual mechanism makes PSO particularly effective at avoiding local minima and finding a global minimum in complex, multimodal landscapes.

To better explain how optimization problems can be used to solve the hyperbolic fitting problem, we have included Figure 2-15. This figure comprises two sub-figures aimed at visually demonstrating the estimation of hyperbolic parameters by locating the minimum value of the cost function. Figure 2-15(a) displays three hyperbolic reflections, each corresponding to a distinct set of parameter combinations. Among them, the hyperbolic reflections that best overlaps with the measured data is the one associated with the set of parameters that minimizes the cost function value. The other two hyperbolic reflections, which exhibit larger fitting errors, are illustrated using dotted lines. In Figure 2-15(b), a plot of cost function values is shown, where the horizontal axis represents different parameter combinations, and the vertical axis represents the corresponding cost function values. Points corresponding to the three-parameter combinations used in Figure 2-15(a) are also marked here, with the point of minimum value distinctly highlighted. This visual representation underscores the proposed method of employing optimization strategies for hyperbolic fitting, reminding that the smallest cost function value at the global minimum equates to the optimal overlap between calculated and measured hyperbolic reflections, hence yielding the most accurate parameter estimation.

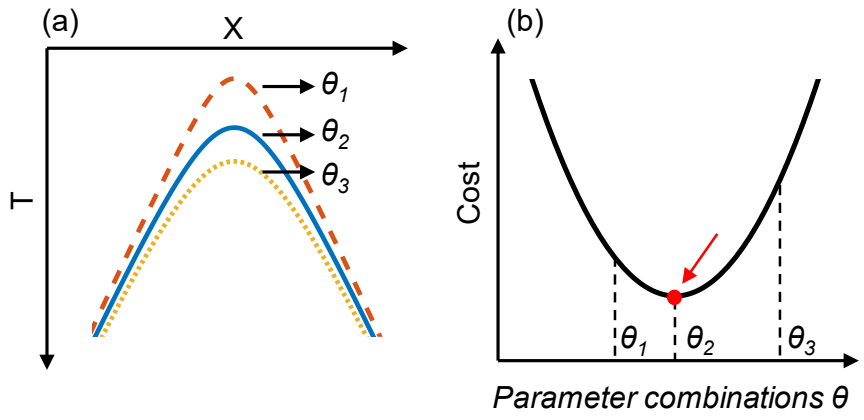

Figure 2-15. (a) Hyperbolic reflections calculated from different parameter combinations and (b) the cost curve of the model. The red dot and arrow indicate the parameter combination of the smallest cost function.

Combining different global optimization algorithms can enhance the robustness and efficiency of solving complex optimization problems, such as fitting hyperbolic curves from GPR data. For instance, initiating the optimization process with PSO utilizes its

capability to broadly explore the solution space, identifying promising regions quickly without getting prematurely trapped in local minima. Subsequently, these solutions can be improved using GD, which can efficiently refine to a minimum value using the initial estimates provided by the PSO. This layered approach not only capitalizes on the strengths of each method—broad exploration and precise exploitation—but also mitigates their weaknesses, providing a more reliable and effective solution for estimating the parameters associated with hyperbolic reflections in GPR data. It is worth noting that the selection of PSO and GD for this study is not prescriptive; similar results could likely be achieved using any compatible combination of global and convex optimization algorithms. This combination of global optimizers underpins the advanced hyperbolic fitting methodology that is central to the research approach in this thesis.

Hyperbolic fitting inherently presents a non-unique solution problem, where multiple sets of parameters, including depth and wave velocity, can accurately describe a single hyperbolic signature. However, by imposing practical constraints on the range of possible values—effectively narrowing the solution space with appropriate prior assumptions—we can significantly reduce the uncertainties associated with parameter estimates. This approach leverages prior knowledge about the subsurface conditions or target characteristics to provide more reliable and constrained fitting results, as discussed in Chapter 6 and supported by references (Xie, et al. 2021).

2.7. Finite Difference Time Domain (FDTD) Modelling of GPR

The Finite Difference Time Domain (FDTD) method is recognized for its robust and versatile capabilities in addressing the full-wave solution of Maxwell's equations, making it highly suitable for modeling electromagnetic wave propagation in GPR applications. The technique employs finite differences as approximations for the spatial and temporal derivatives in Maxwell's equations, allowing for the direct modeling of electric (E) and magnetic (H) fields. This direct approach is effective in simulating GPR wave interactions with various subsurface materials.

FDTD is advantageous because it allows users to specify material properties at every point within the simulation domain, enhancing the accuracy and relevance of subsurface modeling. However, this method also demands substantial computational resources as the model's resolution increases to manage finer details, which can enlarge the computational domain. While FDTD provides detailed insights into electromagnetic wave behavior in heterogeneous media, it does not inherently solve for unique permittivity and permeability values at material interfaces, which could be a limitation in scenarios requiring precise material differentiation. Nonetheless, this issue is generally mitigated by the method's capacity to accommodate large-scale simulations without needing extensive computational overhead typical of finer mesh resolutions used in other methods like Finite Element Method (FEM).

The inclusion of the Courant-Friedrichs-Lewy (CFL) stability condition equation significantly aids in estimating computational costs for FDTD modeling. By delineating the relationship between the spatial discretization (Δx, Δy, Δz) and the temporal resolution (Δt), this equation ensures stability in the numerical simulation:

$$\Delta t \leq \frac{1}{c\sqrt{\frac{1}{\Delta x^2}+\frac{1}{\Delta y^2}+\frac{1}{\Delta z^2}}}, \tag{2.39}$$

where c is the speed of light in vacuum.

For defining the boundaries of the simulation domain in FDTD, artificial boundaries are often necessary. Although this can introduce some complexity, the development of absorbing boundary conditions has matured significantly, providing effective solutions to minimize reflections and artifacts at the domain edges (Giannopoulos, 2005).

Therefore, FDTD method is a powerful approach for simulating the responses of GPR, useful in complex urban subsurface environments. Based on the electromagnetic wave theory, Maxwell’s equations describe the propagation of EM waves, which can be expressed in simplified form, capturing the dynamics of the electric field E and magnetic field H as they relate through time and space:

$$\mu \frac{\partial H_y}{\partial t} = \frac{\partial E_z}{\partial x}, \tag{2.40}$$

$$\varepsilon \frac{\partial E_z}{\partial t} = -\frac{\partial H_y}{\partial x}. \tag{2.41}$$

By employing the Taylor series expansion, functions *f(x)* about a point x_0 with a time step δ, are approximated, facilitating the use of central differences to simulate derivatives in Maxwell's equations. This approach allows for a precise discrete approximation:

$$\frac{df(x)}{dx} \approx \frac{f(x_0 + \frac{\delta}{2}) - f(x_0 - \frac{\delta}{2})}{\delta}. \tag{2.42}$$

Kane Yee first introduced the FDTD method in 1966 (Yee, 1966), utilizing second-order central differences to replace the continuous derivatives in Maxwell's equations with discrete analogs. This discretization of both space and time permits the electric and magnetic fields to be calculated at staggered intervals in a computational grid. By solving these discretized equations, known as "update equations," the future states of the field variables are predicted based on their known past values, ensuring a dynamic and accurate simulation of GPR wave interactions with the subsurface environment (Warren et al., 2016).

3. Chapter 3: Unified Optimization-Based Analysis of Hyperbolic Fitting Models

3.1. Chapter Overview

After introducing the basic principles of GPR and several hyperbolic fitting methods, this chapter delves into the utilization of GPR as a critical instrument for subsurface exploration, specifically highlighting its capability in detecting cylindrical objects like pipelines and rebars, which often manifest as hyperbolic patterns in GPR data. The focus of this investigation centers on the technique of hyperbolic fitting, a prevalent method for interpreting such data, examining the influence of several variables including antenna separation, target radius, burial depth, and the relative permittivity of the surrounding medium. This study conducts a thorough comparative analysis of two hyperbolic and three non-hyperbolic ray-path models, all framed within a unified optimization-based analytical framework. A novel evaluation metric, the C-value, is introduced to quantitatively assess each model's performance. The analysis reveals how these parameters distinctly affect each model's effectiveness, leading to tailored recommendations for model selection based on the availability of prior information and the models' fidelity to actual data. This comprehensive approach augments the accuracy and reliability of both hyperbolic and non-hyperbolic fittings in GPR studies and enhances practical understanding, thereby offering substantial advancements in GPR application methodologies.

3.2. Historical Development of Hyperbolic Fitting Models in GPR

The evolution of hyperbolic fitting models reflects a significant transition from basic echo radar techniques, widely used in various geological applications, to sophisticated methods that are tailored for detailed subsurface analysis. This transition has incorporated a wide range of signal-processing methodologies, some of which can find its origins in fields such as seismology.

The genesis of what we now understand as hyperbolic fitting can be traced back to pioneering efforts by researchers such as Osumi and Ueno in 1985, who laid foundational concepts in radar signal ray models (Figure 2-9), setting the stage for later developments (Osumi and Ueno, 1985). Although these early models did not employ fitting methods for precise parameter estimation, they introduced the community to the potential of utilizing radar data for subsurface characterization.

Significant advancements in GPR signal processing occurred in the late 20th and early 21st centuries. In 2000, Al-Nuaimy et al. introduced innovative approaches to hyperbolic reflection extraction using pattern recognition and neural networks, marking a significant leap towards automated and refined fitting methods (Al-Nuaimy et al., 2000). The work by Shihab and Al-Nuaimy in 2005 further pushed these boundaries by integrating considerations such as the target's radius into hyperbolic fitting models (Figure 2-10), bringing them closer to the contemporary understanding of these techniques (Shihab and Al-Nuaimy, 2005).

The development of models considering antenna separation came later, proposed by researchers like Illawathure et al. in 2020 and Shen et al. in 2019 (Illawathure et al., 2020; Shen et al., 2019). These models, while still simplifying the target as a point source, acknowledged the complex dynamics of signal propagation and interaction within different subsurface conditions (Figure 2-11).

More recent innovations have seen even more complex models that account for both the antenna separation and the target radius. In 2016, Zhang et al. and Sham and Lai introduced sophisticated models that either assume the reflection point at the center of the target (Figure 2-13) or at the intersection of the line connecting the antenna center with the target’s outer contour (Figure 2-12), respectively (Giannakis et al., 2021; Lau et al., 2021; Sham and Lai, 2016a; Zhang et al., 2016). These models represent the highest order of fitting complexity used in contemporary GPR studies and have been applied in a variety of contexts, ranging from underground media analysis on other planets to the detection of urban infrastructure leakages.

This chapter synthesizes these historical developments and conducts a comparative analysis of five widely used models. This comparative approach underscores the versatility and adaptability of GPR technology and highlights the ongoing need to refine these models to enhance their applicability in practical geological and engineering scenarios.

3.3. Evaluation Metric: The Cost Function Value (C-Value)

In assessing the performance of hyperbolic fitting models within this chapter, a critical metric used is the cost function value, referred to as the C-value. This value is computed following Equation (2.28), which articulates the optimization challenge in the research methodology. Specifically, the C-value is calculated as the sum of squared differences between the measured TTT, T_i, obtained from GPR, and the synthetic TTT, t_i , predicted by the hyperbolic models after determining the parameters for burial depth (D) and wave velocity (v). It shall be noted that the GPR survey line is assumed to be perpendicular to the target in this chapter. The influence of the target orientation will be explored in the next chapter.

The C-value serves as a quantitative indicator of how well a hyperbola or non-hyperbola model conforms to the actual GPR data. Essentially, a lower C-value denotes a higher degree of alignment between the model predictions and the actual data, indicating a more accurate representation of the subsurface features. This metric enables an objective comparison across different hyperbola or non-hyperbola fitting models, providing a standardized measure of model effectiveness. In practical terms, when the parameters of burial depth and wave velocity are known or can be precisely estimated, the C-value offers a robust criterion for evaluating the suitability and precision of various fitting techniques. Through this tool, this chapter aims to delineate the model that best matches the detected hyperbolic signatures under varying subsurface conditions, thereby enhancing the reliability and applicability of GPR analysis in geophysical explorations.

3.4. Numerical Simulations

To validate the global optimization algorithms for the five hyperbolic fitting models and quantitatively study the performance of these methods in different scenarios using the C-value analysis, a series of numerical simulations were conducted using gprMax (Antonios 2005; Warren et al., 2016), an open-source Finite-Difference Time-Domain method (FDTD) simulation software that allows users to simulate the GPR response to the subsurface world. This software enabled us to understand how various parameters impact the performance of hyperbolic fitting models. Simulations are important in this study as they allow for precise control of variables, facilitating a clear understanding of their impact on hyperbolic fitting model performance. In this way, we can systematically test and fine-tune the models, highlighting potential challenges, and informing model selection for various real-world scenarios.

Specifically, four sets of simulation models were created by varying the following parameters: radius of the metal targets, antenna separation, buried depth, and relative permittivity of the host material. For all simulations, the TE mode was selected, and a Ricker wavelet with a center frequency of 900 MHz was used for excitation. The time window was set to be 15 ns with a step interval of 0.01 m. The specific parameters of the simulation models are detailed in Table 3-1, Table 3-2, Table 3-3, and Table 3-4.

In this research, the 'TE mode' refers specifically to the orientation of the electric field relative to the pipe or target, rather than to any solver mode within the gprMax software. TE (Transverse Electric) mode in Ground Penetrating Radar (GPR) applications involves the electric field oscillating perpendicular to the direction of wave propagation, illustrated in Figure 3-1. This orientation is crucial when using dipole antennas like bowties for pipeline detection, as the electric field alignment parallel to the pipe's axis (typically in the Z-direction) enhances the reflectivity and clarity of the signals from buried structures. Our simulation setup in gprMax accordingly simulates this scenario by analyzing the Ez component of the electric field, which reflects the vertical alignment of the electric field, mimicking the real-world behavior of TE-mode polarized GPR antennas.

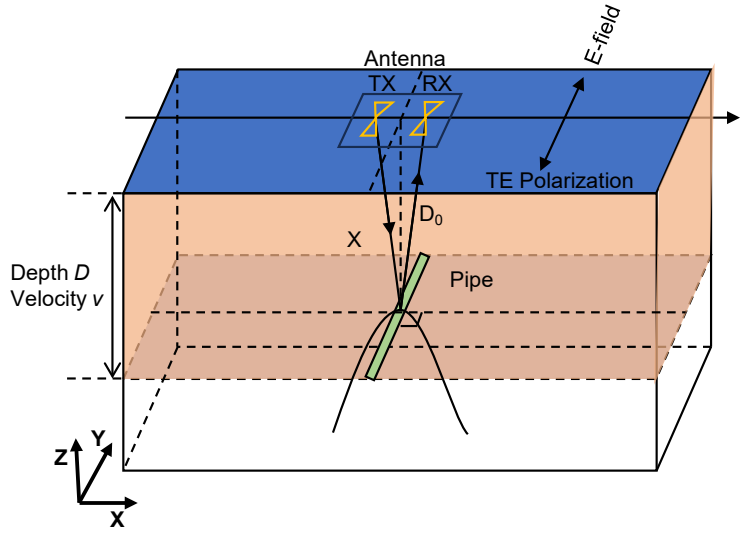

Figure 3-1. Illustration of the numerical-simulation model.

Table 3-1. Simulation models with the varying radius of the target.

Parameters	Simulation models				
	1	2	3	4	5
Radius of target **r** (m)	0.02	0.05	0.1	0.2	0.3
Antenna separation **S** (m)			0.05		
Buried depth **D** (m)			1		
Relative Permittivity **P**			5		

Table 3-2. Simulation models with varying antenna separation.

Parameters	Simulation models				
	1	2	3	4	5
Radius of target **r** (m)			0.1		
Antenna separation **S** (m)	0.02	0.05	0.1	0.2	0.3
Buried depth **D** (m)			1		
Relative Permittivity **P**			5		

Table 3-3. Simulation models with varying buried depths.

Parameters	Simulation models				
	1	2	3	4	5
Radius of target **r** (m)			0.1		
Antenna separation **S** (m)			0.05		
Buried depth **D** (m)	0.3	0.6	0.9	1.2	1.5
Relative Permittivity **P**			5		

Table 3-4. Simulation models with varying relative permittivity.

Parameters	Simulation models		
	1	2	3
Radius of target **r** (m)		0.1	
Antenna separation **S** (m)		0.05	
Buried depth **D** (m)		1	
Relative Permittivity **P**	3	5	10

Post-processing steps involved setting the time-zero position and picking the hyperbolic points, as shown in Figure 3-1, which presents the example results for models with varying target radius (black dots). To study the impact of noise on hyperbolic fitting methods, Gaussian white noise was introduced to the raw data, rendering the signal-to-noise ratio (SNR) of the noisy data at 5 dB (red dots). Additionally, experiments were conducted using Gaussian white noise to achieve signal-to-noise ratios (SNRs) of 10dB, 20dB, and 40dB. The conclusions drawn were consistent across all these noise levels. Therefore, to maintain conciseness, these additional experiments were not chosen to report in detail.

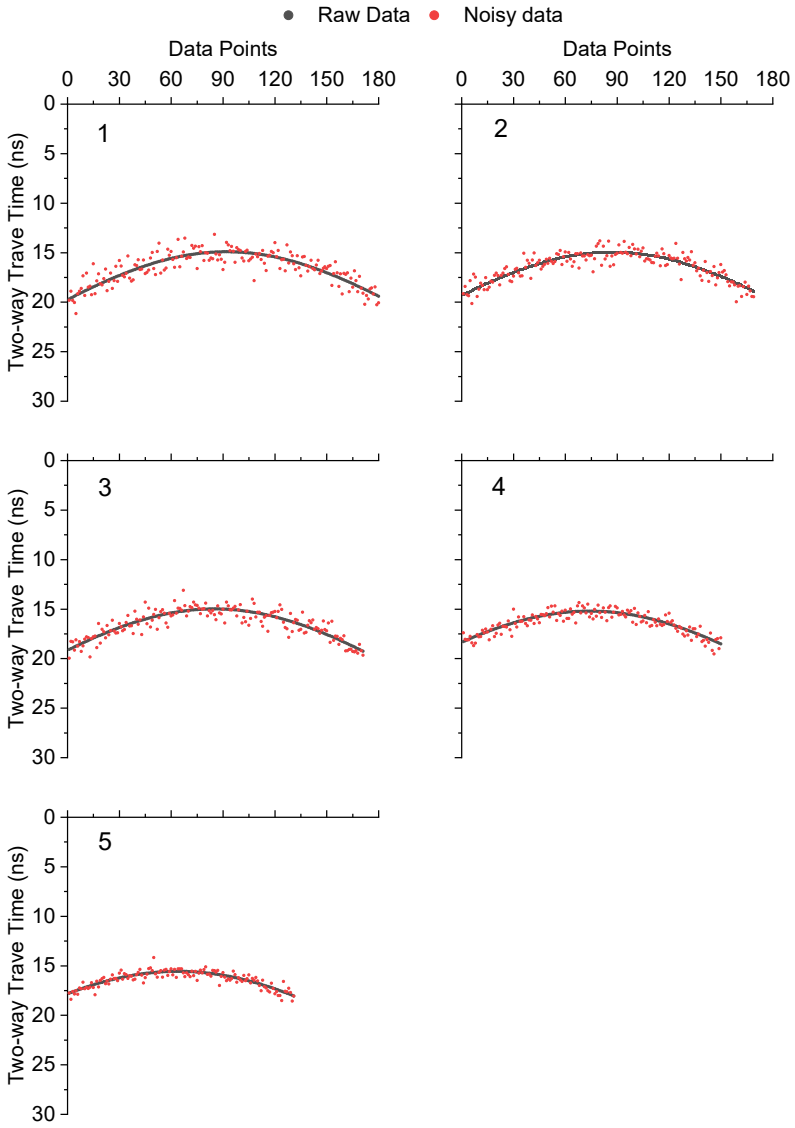

Figure 3-2. Hyperbolic reflection picking results and noisy data of the simulation model with varying radius of targets.

Using the known model parameters, the C-value of different hyperbola and non-hyperbola fitting methods can be obtained and is depicted in Figure 3-2. The C-value serves as a tool to evaluate the performance of each method, with a lower C-value indicating better performance.

Figure 3-2(a) illustrates the effect of changing the radius of targets on the C-value. Initially, for smaller radii, all five models perform comparably. However, as the radius increases, the performance of Model 1 and Model 2 markedly declines. The other models - Model 3, Model 4, and Model 5 - remain stable in performance. This suggests

that incorporating the radius of targets into the hyperbolic fitting models significantly improves accuracy, particularly when the target radius is substantial compared to the depth and antenna separation in terms of size.

Figure 3-2(b) focuses on the effects of antenna separation on the C-value. The results indicate that accounting for antenna separation in hyperbolic fitting significantly enhances the models' performance. It's noteworthy that up to a certain limit, the antenna separation does not drastically affect the models. However, when antenna separation exceeds a critical threshold (such as 0.4 m or 0.6 m), neglecting it from the models can lead to significant errors. This finding emphasizes the importance of considering antenna separation, especially in scenarios with larger separations.

Figure 3-2(c) explores the influence of buried depth on the models' performance. With increasing depth, there is a general decline in the C-value across all models, with Model 1 and Model 2 experiencing the most significant drops. Interestingly, when targets are buried at shallow depths where their diameters are comparable to the depths, Model 1 and Model 2 perform poorly, as evidenced by their high C-values. This indicates that they are ill-suited for hyperbolic fitting under such conditions. However, as the depth increases relative to the radius, the performance of all models begins to converge.

Lastly, Figure 3-2(d) examines how the relative permittivity impacts the C-value. All models exhibit an increasing trend in C-value with growing relative permittivity. However, Model 1 and Model 2 underperform compared to the others. This observation suggests that Model 1 and Model 2 might not be the ideal choices when dealing with the high relative permittivity of the host material.

In summary, Model 4 and Model 5 consistently exhibit small C-values across all experimental scenarios and are closely matched in results. Model 3 performs well in general, with the exception of cases involving large antenna separations. Conversely, Model 1 and Model 2 have limitations in handling varying radius, depth, and relative permittivity effectively. The findings demonstrate the importance of considering key

parameters such as target radius, antenna separation, buried depth, and relative permittivity in hyperbolic fitting models for GPR data to achieve optimal accuracy.

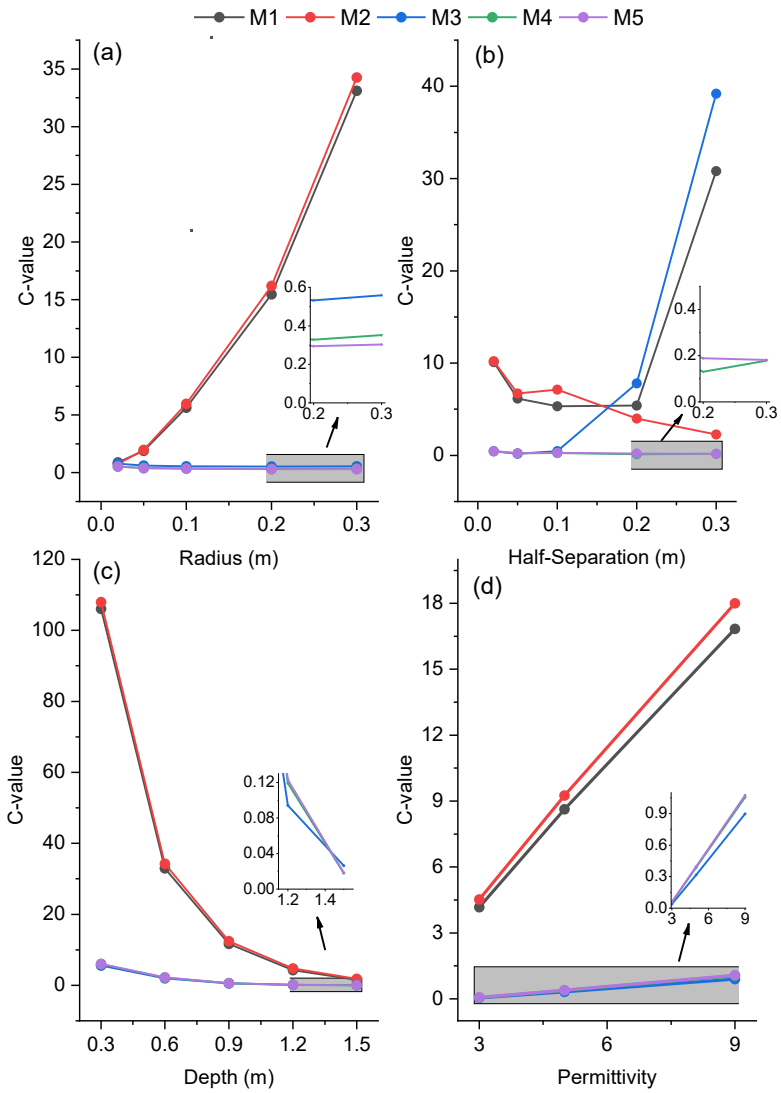

Figure 3-3. The C-value of different hyperbolic fitting models of simulation models with varying (a) radius of target, (b) antenna separation, (c) buried depth, and (d) relative permittivity.

Utilizing the combination optimization algorithm proposed earlier, we can estimate the optimized depth and wave velocity. The results of simulation with varying target radius are presented in Figure 3-3. It is evident that as the radius increases, Model 1 and 2 yield deteriorating results, while Models 3, 4, and 5 maintain a stable and high level of accuracy. The resilience of Models 3, 4, and 5 due to the changing radius signifies their robustness. Additionally, the noise levels, quantified by signal-to-noise ratio (SNR), play a notable role. As SNR decreases (noise increases), the errors for all models

increase. Interestingly, as the radius increases, the influence of noise appears to diminish. This may be because the increased radius has a greater effect on the model than the noise.

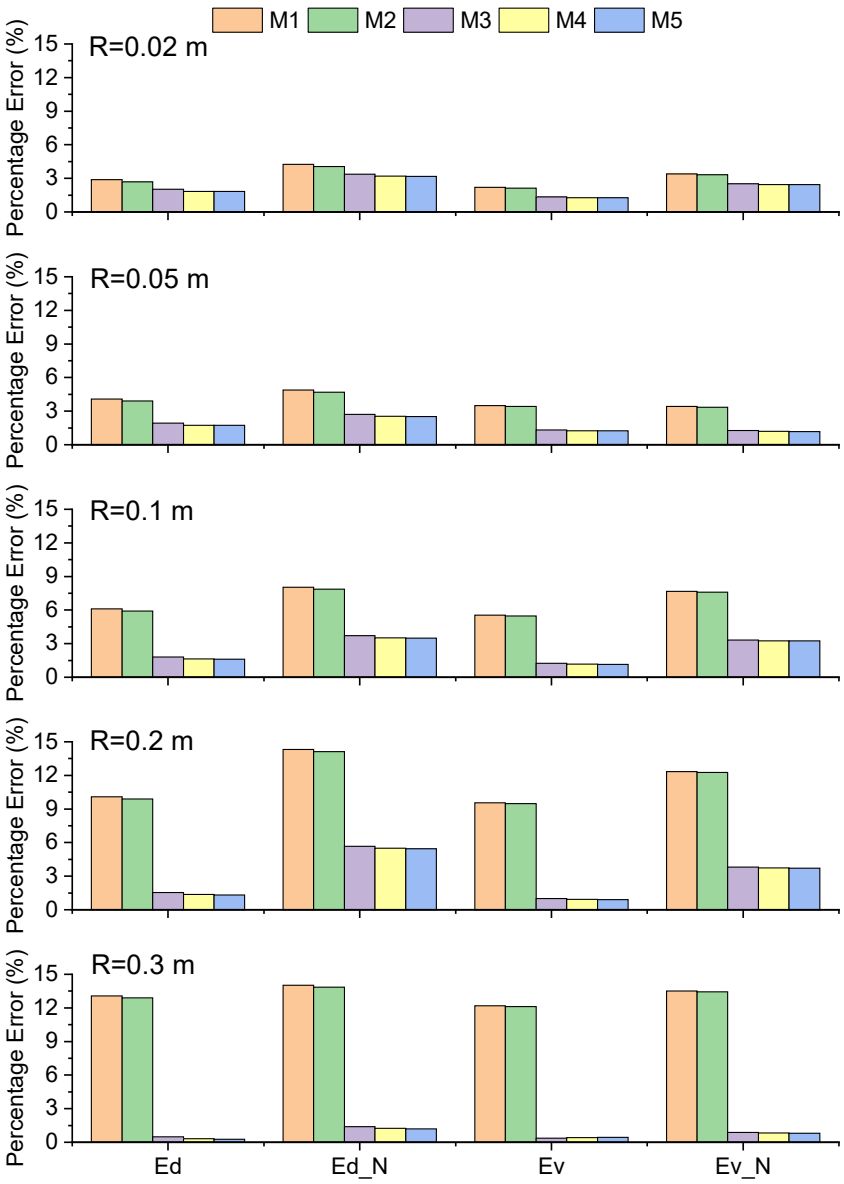

Figure 3-4. Errors in parameter estimation for simulation models with varying radii. Ed – Errors in the estimated depth from raw data; Ed_N – Errors in the estimated depth from data with added noise; Ev – Errors in the estimated wave velocity from raw data; Ev_N – Errors in the estimated wave velocity from data with added noise. The 'noisy data' refers to the original hyperbolic data mixed with additional noise components.

Figure 3-4 shows the impact of antenna separation on parameter estimation. For smaller separations, Models 3, 4, and 5 excel compared to Models 1 and 2. However, as the separation expands, Model 3's accuracy declines, while Models 4 and 5 continue to

perform satisfactorily. Interestingly, for smaller separations, noise deteriorates the parameter estimation for all models, but for larger separations (as seen in experiments 4 and 5, where B=0.2 and 0.3 m, respectively), noise seems to improve the accuracy.

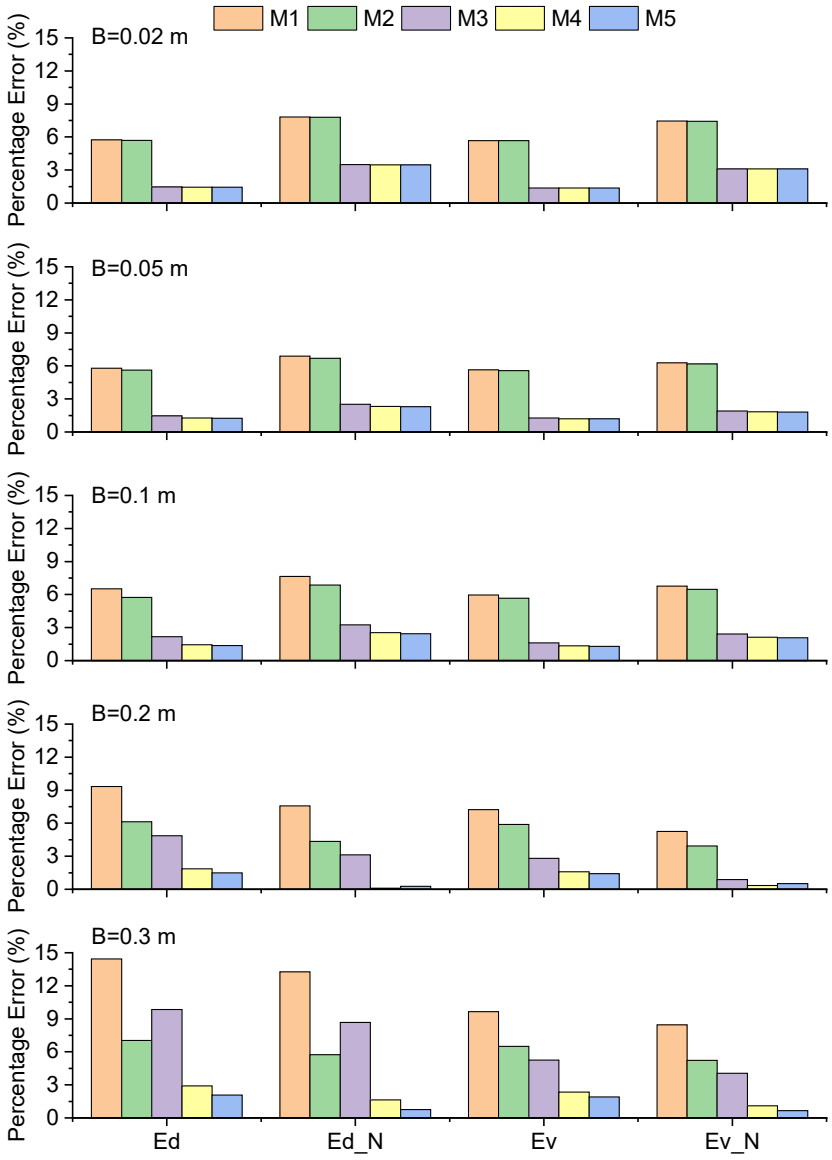

Figure 3-5. Errors in parameter estimation for simulation models with varying antenna separation.

Figure 3-5 portrays how varying the buried depth impacts parameter estimation. Generally, as the depth increases, the estimation accuracy for all models rises. Models 3, 4, and 5 particularly outperform Models 1 and 2 in most scenarios because of the small percentage errors. An interesting observation is that when the target is buried at

shallow depths, noise tends to enhance estimation accuracy, but it negatively affects accuracy for deeper burials.

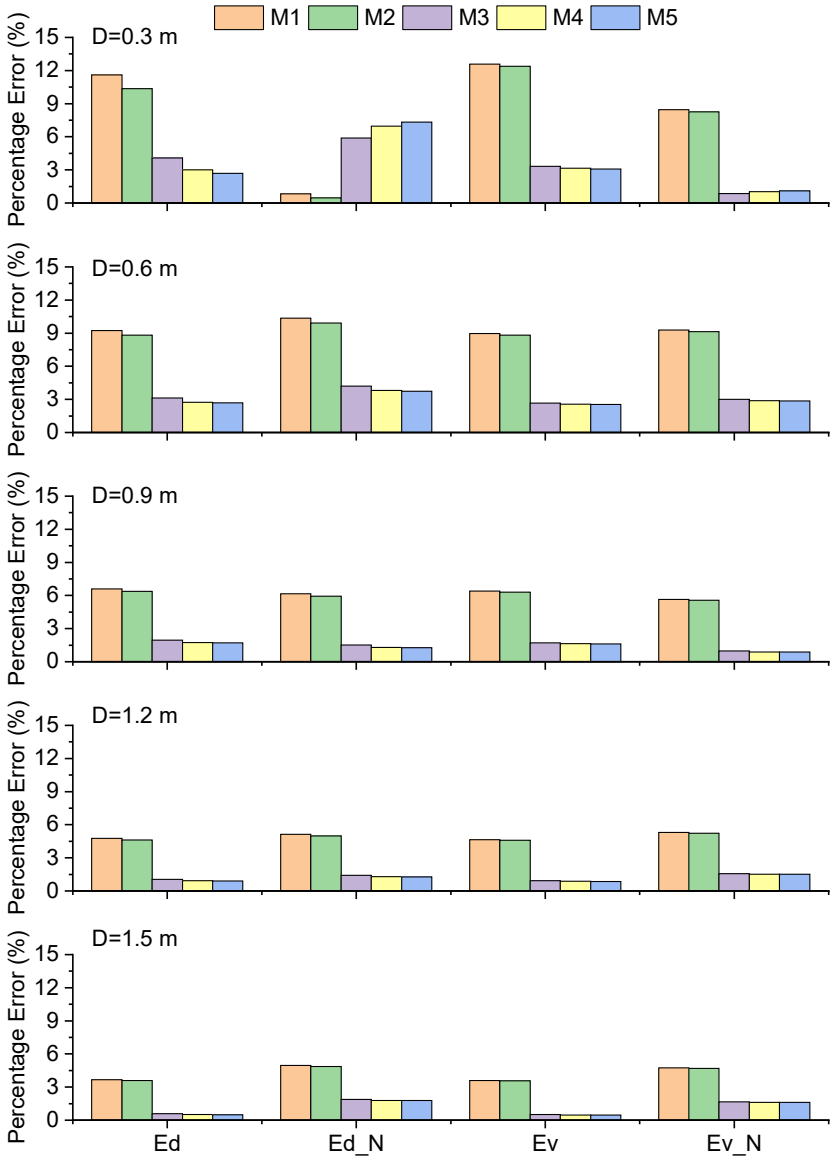

Figure 3-6. Errors in parameter estimation for simulation models with varying buried depth.

The effect of the relative permittivity of the host material on the estimation of depth and wave velocity is noteworthy. Figure 3-6 shows a trend where increasing relative permittivity leads to decreasing accuracy in parameter estimation. Models 3, 4, and 5 again outperform Models 1 and 2 with raw data. However, when noise is introduced (in simulations 1 and 3), Models 1 and 2 surprisingly exhibit a significant boost in parameter estimation accuracy, whereas Models 3, 4, and 5 suffer. This may be because

all models are not true representations and inherently contain errors, which manifest through variations in the material's dielectric properties. In simulation 2, where P=5, noise seems to have a negligible impact on all models.

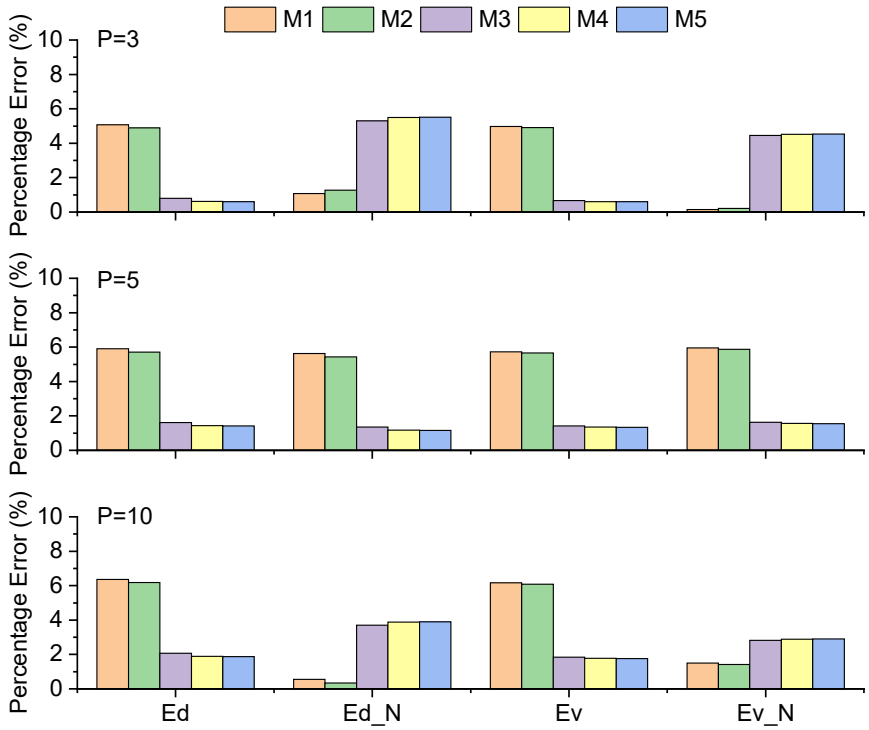

Figure 3-7. Errors in parameter estimation for simulation models with varying relative permittivity.

In assessing computational efficiency, we analyzed the time required to run each model on our computing platform. The benchmarking was carried out on a Windows laptop with an AMD Ryzen 7 quad-core 2.9 GHz CPU and 16 GB of memory, using Matlab 2022 for computations. As depicted in Figure 3-7, Models 1 through 3 demonstrated a considerable advantage in terms of computational speed. The inclusion of antenna separation and target radius in Models 4 and 5 increased their computational demands, with Model 5 exhibiting the longest computation times. Notably, the introduction of noise to the data did not significantly affect the computational times, suggesting that noise level does not impact the efficiency of the computations.

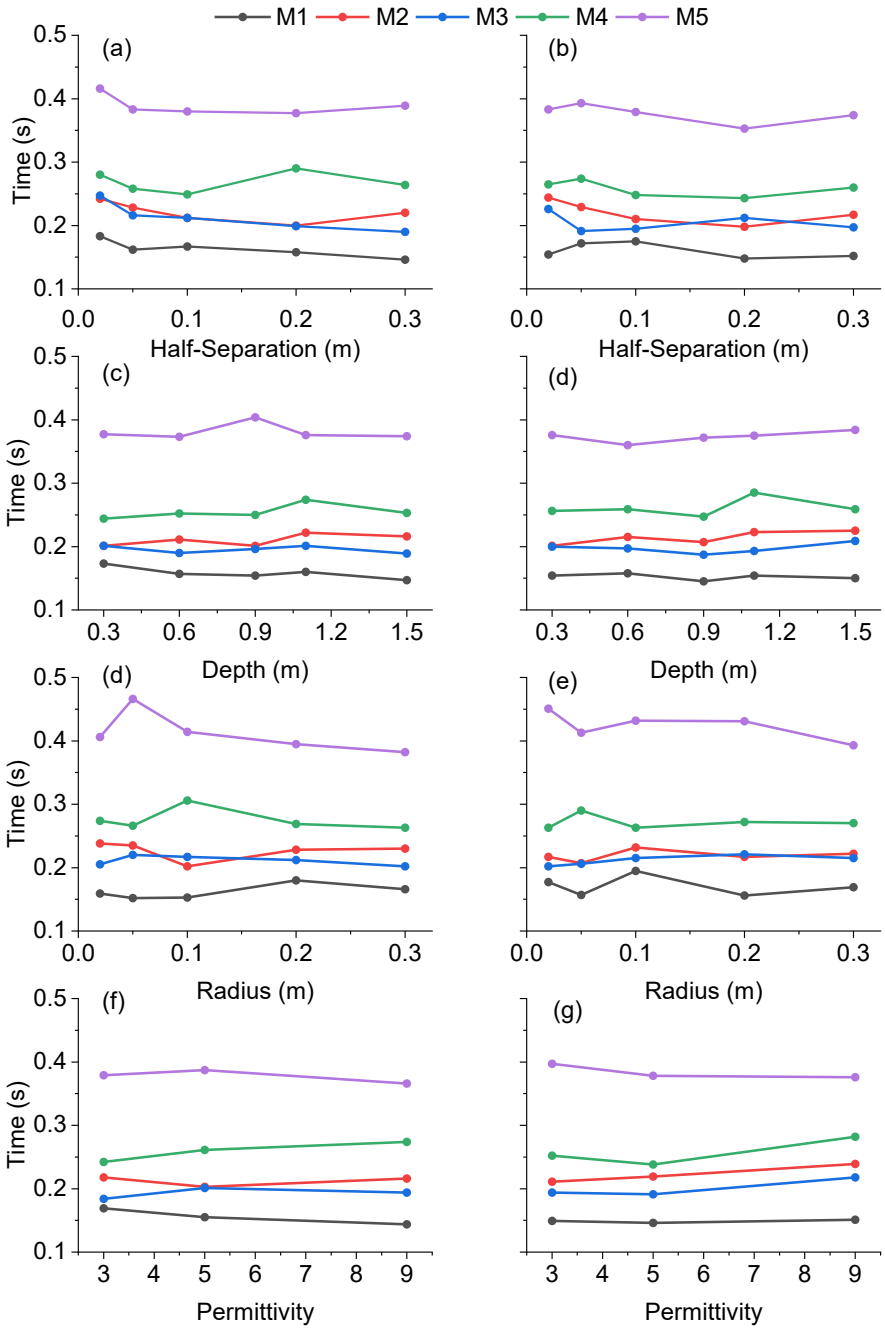

Figure 3-8. Computational time (seconds) of the models for all simulation data. Panels: (a) Raw data and (b) noise-added data of separation simulation; (c) Raw data and (d) noise-added data of depth simulation; (e) Raw data and (f) noise-added data of radius simulation; (g) Raw data and (h) noise-added data of permittivity simulation.

The numerical simulations have offered invaluable insights into the behavior of the models under controlled settings, and how they respond to various parameters such as radius, antenna separation, buried depth, and relative permittivity. Models that account for radius (M3, M4, and M5) consistently perform better with increasing radius, as opposed to those that do not. The assumption of point sources is increasingly not valid

when the radius and antenna separation increases, such that M1 and M2 yield larger errors. On the contrary, models that take antenna separation into account excel in these conditions. All models seem to improve with increasing depth since, with deeper targets, the relative effects of radius and antenna separation reduce, thus diminishing the errors they introduce. This is evident as all models demonstrated similar C-values at a burial depth of 1.5 m (Figure 3-2).

There is a general trend of deteriorating performance with increasing relative permittivity across all models. However, Models 1 and 2 experience a more drastic decline in performance. Based on the simulation results, Models 4 and 5 stand out in terms of performance under various parameters, with Model 3 also exhibiting commendable results except in large antenna separation scenarios. Considering computational costs, Model 4 is recommended for hyperbolic fitting with known information, whereas Model 1 is suitable when radius and antenna separation are relatively small compared to the depth and prior information is lacking. The addition of Gaussian white noise generally leads to reduced estimation accuracy of parameters. Interestingly, under certain conditions such as very large antenna separation or very low relative permittivity, noise appears to improve parameter estimation accuracy. This counter-intuitive result may be attributed to unintentional corrections of data imbalances by the noise. However, it should be noted that this might not be a general characteristic and is contingent on the specific conditions. It's important to highlight that attenuation was not considered in the simulations. This is a significant difference from the field experiments and can influence the behavior of the models.

3.5. Laboratory and Field Experiments

To further evaluate the five models in the real-world environment, both laboratory and field experiments were conducted. These experiments are crucial for understanding how various parameters influence hyperbolic signatures in practice.

3.5.1. Laboratory Experiments

Laboratory experiments were conducted in air, a decision motivated by the known relative permittivity of the air medium, which facilitated a controlled environment for error analysis (Figure 3-8). The experiments employed two GPR antennas from Geophysical Survey Systems, Inc. (GSSI). The antennas operated at central frequencies of 900 MHz and 2 GHz, with respective antenna separations of 0.156 m and 0.04 m. The experiments comprised three target depths (0.5 m, 1 m, and 1.5 m) and three target radii (0.01 m, 0.03 m, and 0.163 m). Table 3-5 outlines the parameters of each laboratory experiment.

Figure 3-9 and Figure 3-10 showcase the B-scan radargrams for each laboratory experiment. These radargrams underwent normalization for analysis. It is evident from the figures that hyperbolic signatures captured by the 2 GHz GPR are subdued, possibly due to strong signal attenuation and scattering. Such attenuation poses difficulties in hyperbolic extraction. Furthermore, it is essential to note that while higher GPR frequencies enhance resolution, they also increase susceptibility to noise. This factor necessitates careful consideration in the selection of GPR frequencies, especially as decreasing the frequency may correspondingly increase the antenna separation.

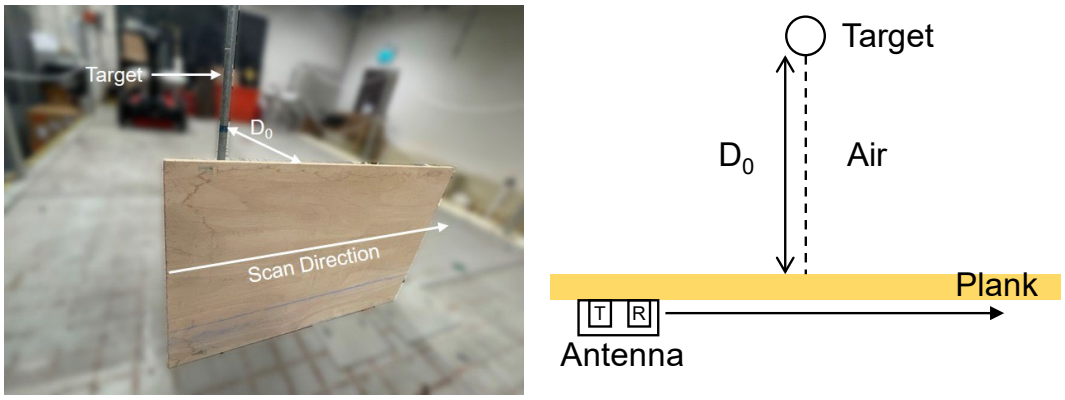

Figure 3-9. Laboratory experiments setup.

Table 3-5. The parameters of laboratory experiments.

Experiment No.	Parameters		
	Antenna separation 2**B** (m)	Radius of target **r** (m)	Buried depth **D** (m)
1	0.04	0.01	0.5
2	0.04	0.01	1
3	0.04	0.01	1.5
4	0.04	0.03	0.5
5	0.04	0.03	1
6	0.04	0.03	1.5
7	0.04	0.163	0.5
8	0.04	0.163	1
9	0.04	0.163	1.5
10	0.156	0.01	0.5
11	0.156	0.01	1
12	0.156	0.01	1.5
13	0.156	0.03	0.5
14	0.156	0.03	1
15	0.156	0.03	1.5
16	0.156	0.163	0.5
17	0.156	0.163	1
18	0.156	0.163	1.5

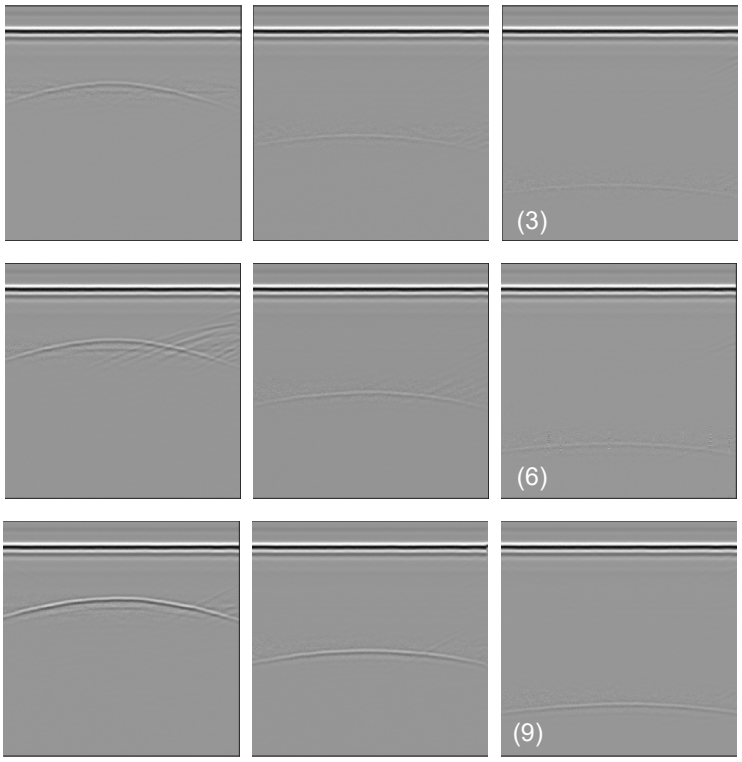

Figure 3-10. Radargrams using a 2 GHz GPR system. Here, the number in the lower left corner of each figure represents the experimental number in Table 3-5.

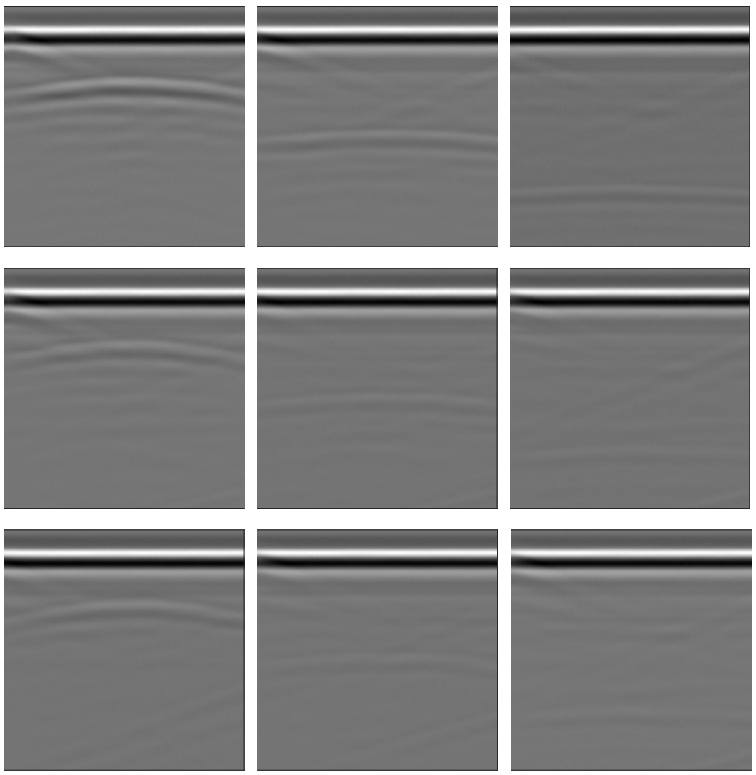

Figure 3-11. Radargrams using 900 MHz GPR system. Here, the number in the lower left corner of each figure represents the experimental number in Table 3-5.

Upon extracting the positions of peak echoes along the pipes, hyperbolic signatures were obtained and are presented in Figure 3-11. To ensure data integrity, Gross Error rejection was applied. An initial observation reveals that escalating antenna separation from 0.04 m to 0.156 m has minimal impact on the shape of the hyperbolic pattern. However, as target depth increases, a flattening effect on the hyperbolic reflection is discernible. A comparable trend of flattening is observed with an increase in target radius.

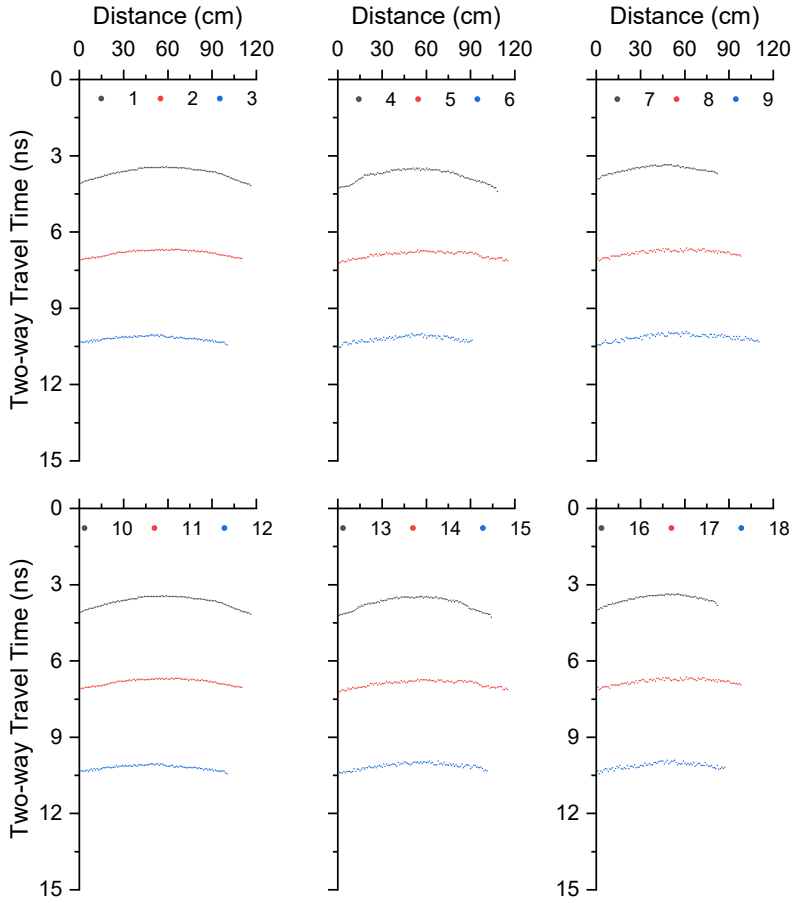

Figure 3-12. The extracted hyperbolic signatures of all experiments. Note: the number of experiments can be related to Table 3-5.

Utilizing the previously mentioned methodology, the C-value for all laboratory experiments was computed. Figure 3-12 provides a graphical representation of this data. One of the significant observations is that an increase in radius from 0.01 m to 0.03 m adversely affects the performance of all models. Interestingly, a further increase in radius to 0.163 m resulted in Models 3, 4, and 5 performing commendably using both

2 GHz and 900 MHz GPR, whereas Models 1 and 2 demonstrated poor performance at 2 GHz but satisfactory performance at 900 MHz. Moreover, concerning the antenna separation, there is a general trend of inferior performance for most models using 2 GHz GPR compared to 900 MHz GPR. This is particularly pronounced in the case of Models 1 and 2 for large radius values. Notably, for smaller depths (D = 0.5 m) and target radii (r = 0.01 m), all models exhibited enhanced performance with 2 GHz GPR. This may be because at shorter distances, high-frequency signals have not yet experienced significant attenuation and scattering, allowing the shorter wavelengths of high-frequency signals to achieve higher detection resolution at this stage. Additionally, concerning depth, barring instances where the target radius is relatively large (r = 0.163 cm), there is a common trend across the five models where an increase in depth initially augments the model's performance, but an excessive depth eventually leads to deterioration. This observation deviates from the simulation results. This is because the simulation experiments did not account for signal attenuation and scattering, which can impact the fitting results.

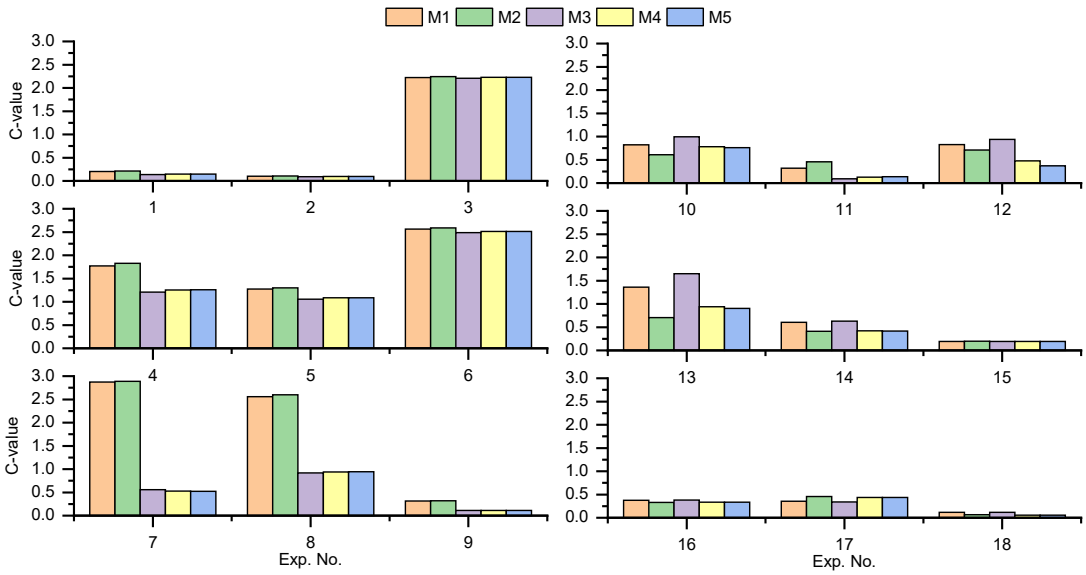

Figure 3-13. The C-value of laboratory experiments. Note: the number of experiments can be related to Table 3-5.

Transitioning to parameter estimation, the combined optimization technique proposed earlier was employed to estimate depth and wave velocity. Figure 3-13 exhibits these results. Consistent with simulation findings, the parameter estimations of depth and

wave velocity across different models are similarly influenced by depth, radius, and antenna separation.

However, a deviation from the C-value analysis is that a larger antenna separation did not enhance the accuracy of parameter estimation but led to a decline. This is exemplified in experiments 16 and 17 where despite a low C-value indicative of a good match with the hyperbolic reflection, the parameter estimation exhibited a high error.

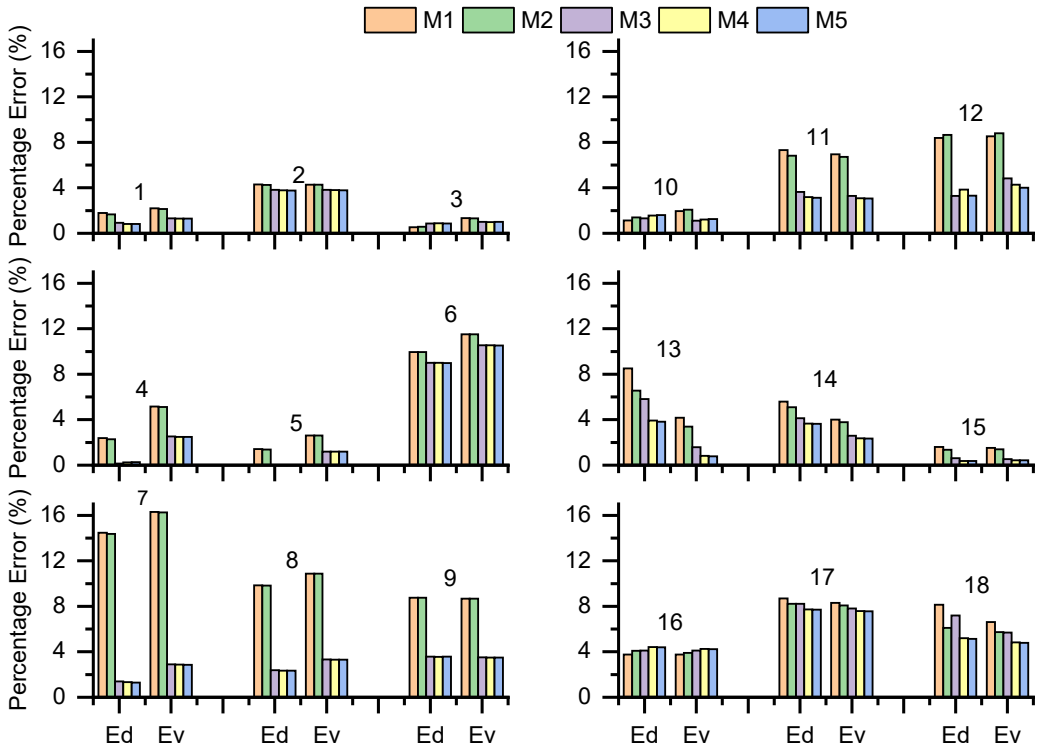

Figure 3-14. Errors of parameter estimation of laboratory experiments.

Upon closely scrutinizing the laboratory experiments, it is evident that the parameters under consideration exhibit similar trends to the simulations. The primary discrepancy between the two lies in the fact that in the laboratory setting, the performance of all models generally declines with increased depth, attributable to severe signal attenuation, an aspect not accounted for in simulations. In practical scenarios, an increase in antenna separation is frequently a consequence of utilizing antennas with reduced working frequencies, which, in turn, are correlated with greater detection depths and diminished signal resolution. This potentially elucidates why all models exhibit better coherence with the hyperbolic reflection obtained through 900 MHz GPR. Furthermore, within a

certain threshold, the increase of the target radius seems to curtail the signal attenuation followed by the increase in depth. This is possibly due to signal resolution; Models 1 and 2 manifest a markedly inferior performance compared to Models 3, 4, and 5 when using 2 GHz GPR, but comparable performances at 900 MHz. The decreased working frequency of the GPR seems to obscure the distinctions amongst the models as a result of variations in radius and depth. In some instances, such as experiments 16, 17, and 18, there is an inconsistency between the C-value analysis and parameter estimations. Despite the low C-value, which suggests a good fit with the hyperbolic reflection, parameter estimation errors are considerably large. This can be attributed to the heuristic nature of PSO, which may occasionally converge to local minima. Consequently, a low-cost function value might not necessarily signify the global optimum, resulting in potential inaccuracies in parameter estimation.

With prior knowledge of the target radius and antenna separation, Model 4 is highly recommended for hyperbolic fitting. It exhibits excellent performance in matching hyperbolic reflections under varying conditions, achieving favorable parameter estimation results via the proposed combination optimization algorithm, and has a reasonable computational cost. On the other hand, in scenarios where prior information is not available, Model 1 is more appropriate. However, care should be taken to consider errors, especially when fitting hyperbolic reflections derived from objects with relatively large radii and shallow depths. Moreover, when utilizing low-frequency GPR for detecting objects buried at greater depths, Model 1 is capable of providing good results of parameter estimation.

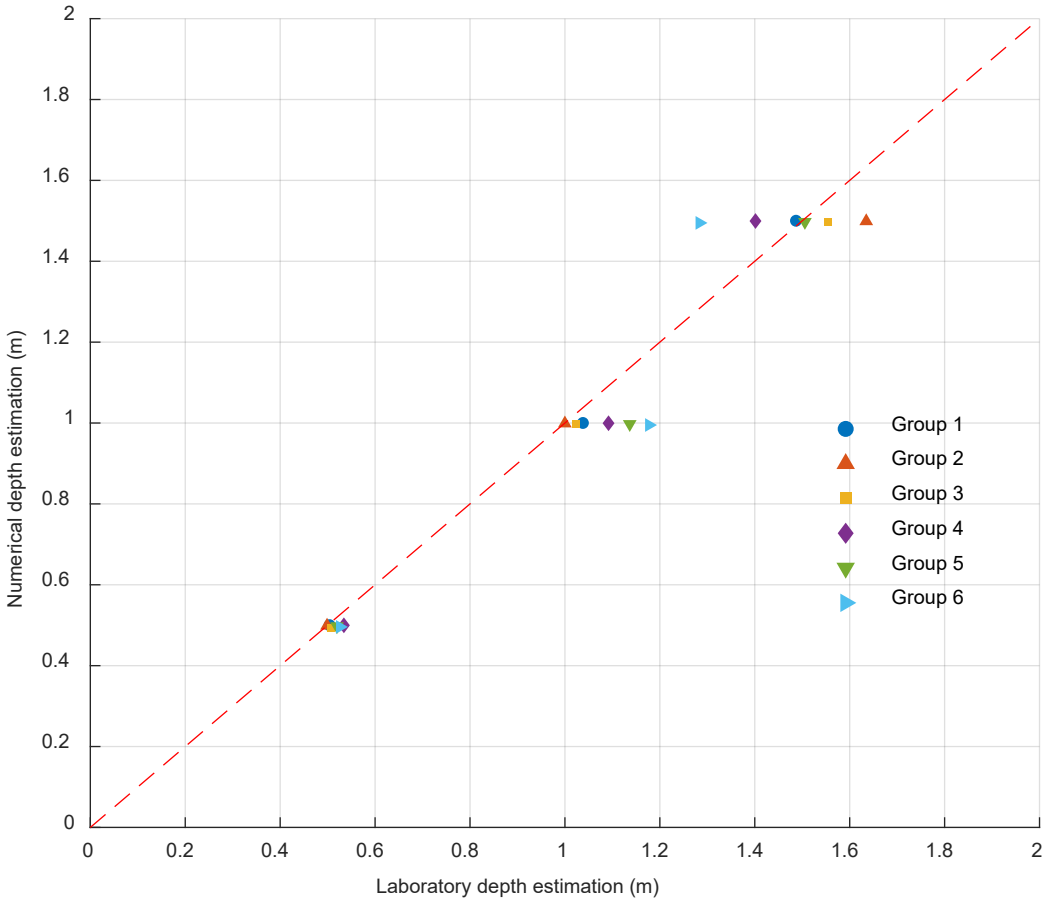

Figure 3-15. The comparison between simulation and laboratory experiments. The numerical experiments were set as same as the 18 laboratory experiments. 18 experiments were divided into 6 groups according to the variation of depth from 0.5m to 1.5m. The detailed parameter setting can be seen in Table 3-5.

To align the methodological framework of the study, additional simulation experiments were conducted that mirrored the parameter settings used in the laboratory experiments, focusing on hyperbolic model 4. Depth estimation results for 18 grouped datasets were extracted, corresponding to variations in depth from 0.5 meters to 1.5 meters, organized into six major groups. These simulation results were then directly compared against laboratory outcomes through a series of scatter plots, which visually map the correlation and discrepancies between the simulated and laboratory data.

The simulation experiments demonstrated a high degree of accuracy, closely aligning with the actual measured values across all experimental groups. Notably, at shallower depths of 0.5 meters, the laboratory results showed a high consistency with the simulation data, clustering near the true values. However, as the depth increased, the laboratory data points began to diverge more significantly from the expected values,

reflecting the growing influence of signal attenuation and scattering that is not present in the simulations. Both scattering and attenuation phenomena result in the weakening of target reflections, increasing the susceptibility of hyperbolic signatures to noise interference, thereby amplifying the discrepancies between modeled and measured data, and escalating the errors in parameter estimation. Additionally, in the initial three groups—characterized by higher frequency and narrower antenna spacing—the dispersion of results was minimal at depths of 0.5 and 1 meter. Beyond these depths, at 1.5 meters, the accuracy of these configurations diminished, underscoring the susceptibility of high-frequency signals to attenuation and scattering effects.

3.5.2. Field Experiments

The field data collection was carried out at the test site in the geophysical environment at IFSTTAR, Nantes, France (Dérobert and Pajewski, 2018). The sand trench was selected as the experimental location. Three metal pipes with a diameter of 0.08 m were buried at different depths, serving as the main reflector for data collection. The actual buried depths of each pipe can be referenced from the as-built report of this geophysical test site. SIR 4000 control unit with GSSI common offset antenna of nominal center frequency at 400MHz was equipped for radargram acquisition.

Figure 3-15 showcases the radargram acquired by a 400 MHz GPR, featuring presented hyperbolic patterns. After extracting the hyperbolic data at the peak-echo points, the optimization method can be applied to estimate the wave velocity and the buried depths of three metal pipes. Given the known burial depths, it is able to compare the accuracy of depth estimation of the five models. The results are presented in Table 3-6.

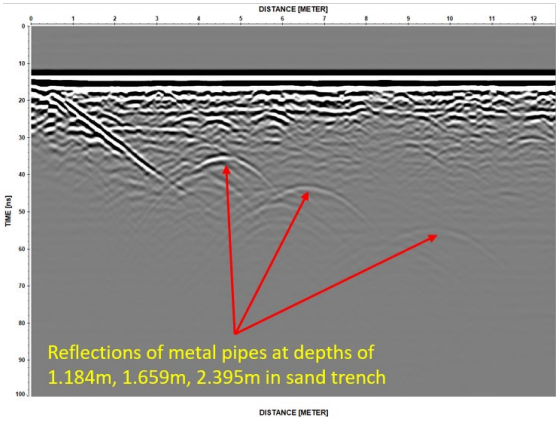

Figure 3-16. Radargram with reflections from metal pipes in the sand trench.

Table 3-6. Estimated depth of the five models.

Model	Pipe1 D = 1.184 m			Pipe2 D = 1.659 m			Pipe3 D = 2.395 m		
	Estimated D (m)	Error (m)	Error (%)	Estimated D (m)	Error (m)	Error (%)	Estimated D (m)	Error	Error (%)
M1	1.258	0.074	**6.25**	1.785	0.126	**7.59**	2.360	0.035	**1.46**
M2	1.254	0.070	**5.91**	1.782	0.123	**7.41**	2.358	0.037	**1.54**
M3	1.241	0.057	**4.81**	1.767	0.108	**6.51**	2.352	0.043	**1.80**
M4	1.237	0.053	**4.48**	1.764	0.105	**6.33**	2.363	0.032	**1.34**
M5	1.237	0.053	**4.48**	1.764	0.105	**6.33**	2.363	0.032	**1.34**

The field experiments echoed the outcomes of the simulations and laboratory experiments. Models M4 and M5 consistently emerged as the most accurate, followed closely by M3, while M1 and M2 were less precise. It's important to note that due to the uncontrolled environment and the lack of actual wave velocity in the field experiments, comprehensive parameter sensitivity analysis based on C-value analysis could not be performed. However, these results offer insights into how the models perform under more realistic conditions and validate their applicability beyond controlled simulations and laboratory settings.

The decreased accuracy of parameter estimation for pipe 2 is attributed to interference from nearby PVC pipes and the inability to extract one side of the curved reflection. In contrast, as with pipe 3, all five models showed similar and improved accuracy as burial

depth increased. This trend aligns with the findings from numerical simulations. Lastly, the improved accuracy observed when using a 400 MHz antenna is likely due to less signal attenuation and noise interference, leading to better data quality. The results from the field experiments highlight the robustness of the proposed methods in real-world applications, substantiating the credibility of the findings from our initial simulations and laboratory experiments. The research underlines the effectiveness of using optimization methods in solving the hyperbolic fitting problem and comparing the performance of different models under various conditions.

3.6. Summary and Contribution

This chapter has examined the efficacy of various hyperbolic fitting models employed in GPR for estimating essential parameters such as burial depth and wave velocity. Through the detailed evaluation of five distinct hyperbolic fitting models, this analysis has illuminated how different model configurations respond under varying conditions—target radius, antenna separation, and material relative permittivity.

Key insights derived from this chapter include:

1. Models that treat targets as point sources displayed varied accuracy, heavily dependent on the relationship between the target's radius and its depth. This finding underscores the importance of considering physical dimensions in model selection and application.

2. Contrary to theoretical expectations, increased depth, while theoretically beneficial for accuracy, often leads to degraded performance due to signal attenuation. This practical challenge suggests a complex interaction between depth and signal quality that must be managed carefully.

3. The research revealed that small variations in antenna separation generally do not impact model performance significantly within a predefined range. However, in practical scenarios, changes in antenna separation are closely tied

to alterations in signal strength and resolution, which can affect the efficacy of the fitting process.

4. The chapter provides generalized recommendations for choosing the most appropriate hyperbolic fitting model, which is model 4, based on available data and operational conditions. These guidelines advocate for a strategic approach to selecting models that balance computational efficiency with accuracy.

It should be noted that in addition to the factors studied in this chapter that affect hyperbolic fitting, the orientation of the target also influences the hyperbolic fitting. This specific research will be introduced in the next chapter. In this chapter, we assume that the GPR survey line is perpendicular to the target, thus the impact of target orientation on hyperbolic fitting can be disregarded.

4. Chapter 4: Angle-Corrected Hyperbolic Fitting Models for Improved Parameter Estimation

4.1. Chapter Overview

Building on the quantitative analysis of hyperbolic models from Chapter 3, this chapter advances the study by focusing on estimating pipe orientation using hyperbolic fitting, a curial factor that is not yet come across in Chapter 3. Traditionally, GPR analysis assumes that traverses are perpendicular to, or the E-field is parallel to, the target alignment—an assumption that often fails in real-world scenarios. To address this, a novel angle-corrected hyperbolic fitting model is introduced in this chapter, which integrates an angle correction index into the conventional fitting approach. This model, formulated as an optimization problem, is solved using a hybrid approach that combines the Multi-Verse Optimizer (MVO) and GD algorithms. Validated through simulation and field experiments, this method enhances the accuracy of estimating parameters like burial depth, object radius, and wave velocity together, especially under varying pipe orientations, offering a more robust framework for GPR data analysis in complex environments.

4.2. Introduction to Angle-Corrected Hyperbolic Fitting

Classical hyperbolic fitting methods have been widely applied in many aspects. Despite these advancements, a significant gap remains in addressing the orientation of subsurface targets relative to the GPR survey line. This oversight is particularly critical as the orientation can profoundly affect the precision of parameter extraction (Jaw and Hashim, 2013; Yuan and Cai, 2020).

While ideal survey conditions assume GPR scans perpendicular to subsurface objects, the reality of urban environments, characterized by a dense and randomly oriented underground utility network, often precludes such perfect alignments (Xie et al., 2018). Various studies have explored the impact of oblique angles between the subsurface object and the GPR line. Techniques like C-scan profile generation, although

straightforward for estimating object orientation, pose challenges in terms of increased data acquisition time and decreased accuracy in complex subsurface environments (Tsung-Hsien and Mendel, 1998). Similarly, the application of full-polarimetric scattering matrices and improved Alford rotation methods offer insights into orientation estimation but are limited by practical field conditions (Liu et al., 2019; Paola and Friedrich, 2003; Seol et al., 2001).

Furthermore, the use of elliptical inversion models and hybrid polarimetric GPR data has shown potential in accurately estimating the orientation and other parameters of elongated subsurface objects, including tree roots, which present additional challenges due to their random orientation (Tanikawa et al., 2013; Wang et al., 2020; Zhou et al., 2022). Despite these methodological developments, traditional hyperbolic fitting techniques cannot still incorporate adjustments for non-perpendicular alignments.

Building upon previous works that introduced an angle correction index to the hyperbolic fitting equation (Lai et al., 2016b; Xie et al., 2018), this chapter presents an advanced approach that incorporates a cost function value (C-value). This C-value is derived from the differences between synthetic and real TTT, offering a novel index for assessing the impact of pipe orientation on fitting accuracy. This approach is enhanced through a hybrid optimization strategy that merges the MVO with GD algorithms, facilitating the simultaneous estimation of pipe orientation, burial depth, and wave velocity. This chapter details the application of this methodology in both simulated and field settings, aiming to refine GPR data analysis for more accurate and reliable underground imaging.

4.3. Methodology

4.3.1. GPR Measurement and Oblique Angle

Commonly in GPR surveys, when the antenna traverses perpendicularly across a buried cylindrical object, the EM field aligns in parallel with the object. This alignment produces an optimal hyperbolic-like pattern for estimating the object depth and wave velocity. However, the presence of an oblique angle between the GPR antenna and the

object changes the dynamics. The oblique angle θ affects the distance from the antenna to the object, reducing it from $\sqrt{x^2 + D^2}$ to $\sqrt{x^2 \sin^2\theta + D^2}$ (Lai et al., 2016b; Xie et al., 2018), where x represents the lateral distance from the antenna to the projection of object on the ground, and D is the depth of the buried object. Here the oblique angle is defined as the included angle between the GPR traverse and a continuous alignment of a buried object. The illustration of such GPR measurement can be seen in Figure 4-1. Considering the orientation of object, traditional hyperbolic fitting models require modification. In this section, two modified hyperbolic fitting methods based on different GPR ray-path models are introduced and subsequently formulated as the optimization problems of scattered points in (x_i, t_i), wherein the cost function is established and computed. Then based on the MVO and GD algorithm, the object orientation, buried depth, and wave velocity will be estimated together.

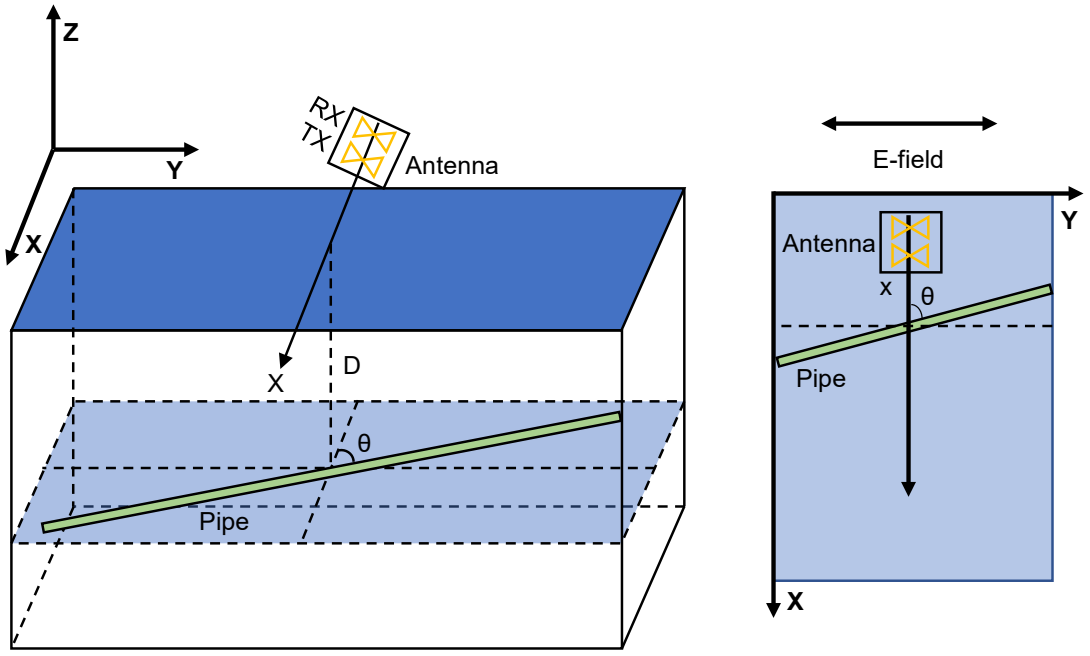

Figure 4-1. Illustration of the GPR measurement with the oblique angle.

4.3.2. Hyperbolic Fitting Model 1 (M1)

This model is graphically represented in Figure 2-9. Within this framework, the separation between the transmitter and receiver antennas is not considered, and the buried cylindrical object is modeled as a point source. The TTT for the GPR system at

position x_i and x_0, where x_0 is the position directly above the target, is denoted by t_i and t_0, respectively. Given the geometry of the scenario and the object orientation, Equation 1 can be derived through fundamental trigonometric principles:

$$t_i = \frac{2\sqrt{D_0^2 + (x_i \sin\theta)^2}}{v}, \tag{4.1}$$

where D_0 is the buried depth of the target, x_i is the distance between the positions of antenna, θ is the oblique angle, and v is the EM wave velocity.

4.3.3. Hyperbolic-like Fitting Model 5 (M5)

As illustrated in Figure 2-13, Model 5 (M5) extends upon Model 1 (M1) by accounting for both the object radius and the separation between the transmitting and receiving antennas (He and Lai, 2024). The governing equations for this model are no longer in the form of the expression of hyperbolic reflection, thereby termed as hyperbolic for convenience, and are expressed as follows:

$$t_i = \frac{D_1 + D_2}{v}, \tag{4.2}$$

$$D_1 = \sqrt{\left[(D_0 + r) - \frac{(D_0 + r)r}{\sqrt{(D_0 + r)^2 + (x_i \sin\theta)^2}}\right]^2 + \left[x_i \sin\theta - \frac{x_i \sin\theta * r}{\sqrt{(D_0 + r)^2 + (x_i \sin\theta)^2}} - S\right]^2}, \tag{4.3}$$

$$D_2 = \sqrt{\left[(D_0 + r) - \frac{(D_0 + r)r}{\sqrt{(D_0 + r)^2 + (x_i \sin\theta)^2}}\right]^2 + \left[x_i \sin\theta - \frac{x_i \sin\theta * r}{\sqrt{(D_0 + r)^2 + (x_i \sin\theta)^2}} + S\right]^2}. \tag{4.4}$$

Here, D_1 is the distance from the transmitter to the object, D_2 is the distance from the object to the receiver, r signifies the object radius, and S denotes half of the antenna separation between transmitter (TX) and receiver (RX).

4.3.4. Establishment of Optimization Problems

Given a set of [D_0, v, $sin(\theta)$], the synthetic TTT, t_i, can be calculated using different hyperbolic fitting equations. The ray-path-based hyperbolic fitting models can then be expressed as optimization problems, where the objective is to find the set of parameters

[D_0, v, $sin(\theta)$] that minimizes the sum of squared differences between the T_i, represents the actual TTT collected by GPR, and synthetic TTT, t_i, calculated by the hyperbolic fitting model. This can be mathematically represented as:

$$argmin\sum_{i=1}^{n}(T_i - t_i)^2 . \tag{4.5}$$

The optimization is framed as a problem of minimizing a cost function (Equation (4.5)), which quantifies the discrepancy between the measured TTT, T_i, and the TTT t_i, predicted by the hyperbolic fitting model.

The MVO (Mirjalili et al., 2016) is a recent optimization algorithm inspired by the multiverse theory in cosmology. The algorithm operates by considering multiple potential solutions as "universes" and employs three main operations, namely, white hole, black hole, and wormhole mechanisms, to navigate the search space and converge toward the optimal solution. To avoid local minima and potential optimization plateaus, this study employs a hybrid optimization approach that combines MVO and convex optimization techniques. Initially, the MVO algorithm, inspired by multiverse theories in cosmology and designed to explore diverse potential solutions as 'universes', is utilized to globally approximate the optimal parameters. These approximations are subsequently refined using the GD method. Importantly, we opted not to include the object radius as an optimization parameter, as previous research has indicated that hyperbolic fitting algorithms have difficulty estimating object radius with the level of accuracy required for practical applications in utility detection (Giannakis et al., 2022).

Once the buried depth, wave velocity, and object orientation are known, the synthetic TTT, t_i, can be computed, and consequently the value of Equation (4.5) (cost function or C-value) can be calculated. This value serves as an index to evaluate the performance of hyperbolic fitting models. A smaller C-value indicates a better match to the detected hyperbolic reflection, allowing for quantitative comparison of these models across various scenarios. Moreover, the C-value offers a mechanism for investigating the

discrepancies between the hyperbolic fitting models and the actual data, without requiring consideration of pipe orientation.

4.4. Numerical Simulation

In continuation of the simulation efforts from Chapter 3, this section focuses on validating the angle-corrected hyperbolic fitting models using gprMax (Warren et al., 2016), a FDTD simulation software. These simulations specifically assess the impact of angle discrepancies on hyperbolic fitting accuracy, exploring how pipe orientation influences the model's effectiveness. By precisely manipulating the angles between the GPR traverse and subsurface targets, we evaluate the performance of the angle correction index introduced in this chapter. This validation not only tests the models under controlled conditions but also helps refine their application in real-world scenarios, ensuring the reliability and applicability of the proposed methods.

The simulation models were constructed with varying parameters to represent conditions encountered in GPR applications. Two sets of models varied by the radius of targets and buried depth, employing the TE mode and a Ricker wavelet with a center frequency of 1000 MHz for excitation. This frequency aligns with the effective bandwidth of 500-1500MHz typical for GPR, chosen based on findings that antenna frequency has minimal impact on hyperbolic fitting accuracy (He and Lai, 2024; Xie et al., 2021a, 2022). However, it is important to note that varying antenna frequencies can significantly affect the signal's interaction with the environment, particularly through mechanisms such as attenuation and scattering, which in turn can influence the visibility and shape of hyperbolic reflections. These environmental effects are critical for understanding the practical implications of frequency selection in field applications.

The time window for simulations was set at 30 ns, with a spatial step interval of 0.01 m. Antenna separation was determined to be 0.1 m, a measure within the limits identified in previous studies for maintaining accuracy in hyperbolic fitting models without exceeding the practical size of GPR antennas (He and Lai, 2024). This setup

facilitates investigations into the effect of antenna separation on parameter estimation accuracy.

The relative permittivity of the host material was set at 5, a value of common ground conditions, and selected for its consistent impact on fitting model accuracy across varying conditions. This standardization allows for a focused analysis of the model's sensitivity to target geometry and positioning. The specific parameters of the simulation models are detailed in Table 4-1 and Table 4-2.

Table 4-1. Simulation models varying in target radius.

Parameters	Simulation models				
	1	2	3	4	5
Radius of target **r** (m)	0.02	0.05	0.1	0.2	0.3
Buried depth **D** (m)			0.9		

Table 4-2. Simulation models varying in buried depth.

Parameters	Simulation models				
	1	2	3	4	5
Buried depth **D** (m)	0.3	0.6	0.9	1.2	1.5
Radius of target **r** (m)			0.1		

During the simulation, the GPR antenna was fixed to move along the designed lines. The scanning lines all passed through the projection of the middle point of the root on the ground surface, crossing the root at a specific angle ranging from 0° to 90° at intervals of 15°, as can be seen in Figure 4-2.

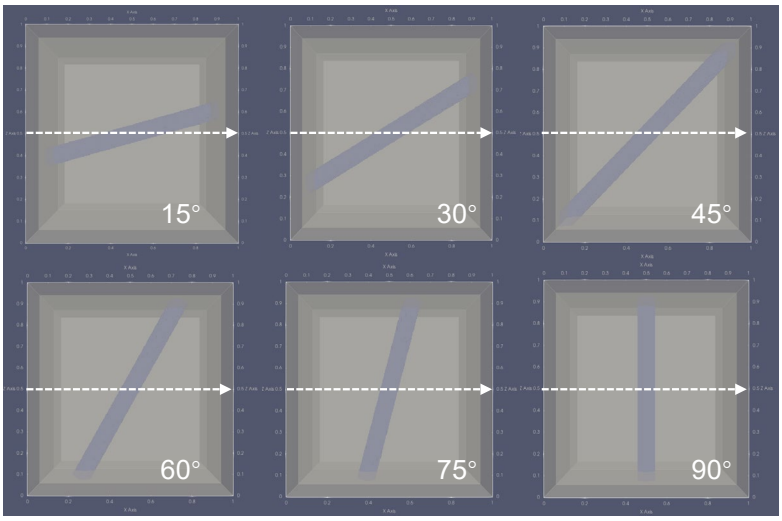

Figure 4-2. Top view of the simulation models and the scanning line.

Post-processing steps involved setting the time-zero position and picking the hyperbolic reflection points. The example results of the GPR radargrams and the corresponding picking hyperbolic patterns can be seen in Figure 4-3.

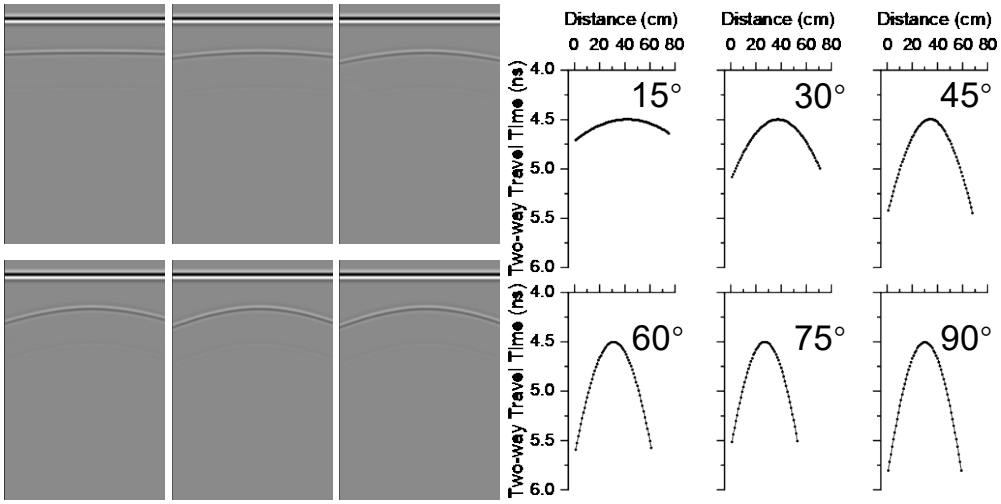

Figure 4-3. Radargrams and corresponding hyperbolic reflection picking results with varying pipe orientations.

Using the known model parameters, the C-value for various hyperbolic fitting methods can be calculated, as shown in Figure 4-4 and Figure 4-5. The C-value serves as a performance metric; a lower C-value suggests better matching between the model and real-world observations. We also calculated the C-value without correcting the oblique angle to assess its impact on the fitting models.

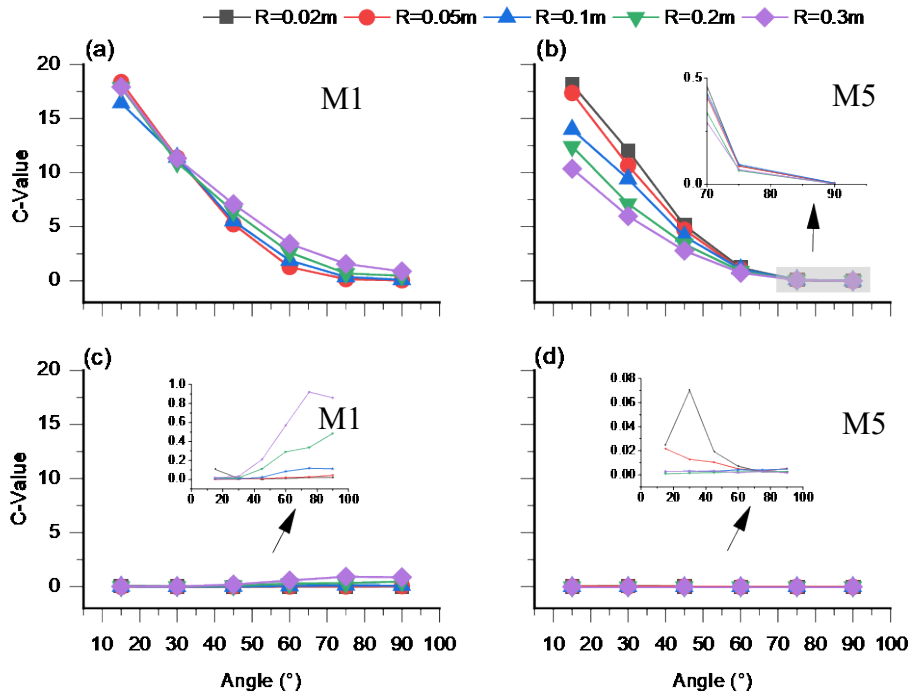

Figure 4-4. C-value analysis for simulation models with varying pipe radius. For M1: (a) C-value considering pipe orientation; (c) C-value without considering pipe orientation. For M5: (b) C-value considering pipe orientation; (d) C-value with varying target radius, without considering pipe orientation.

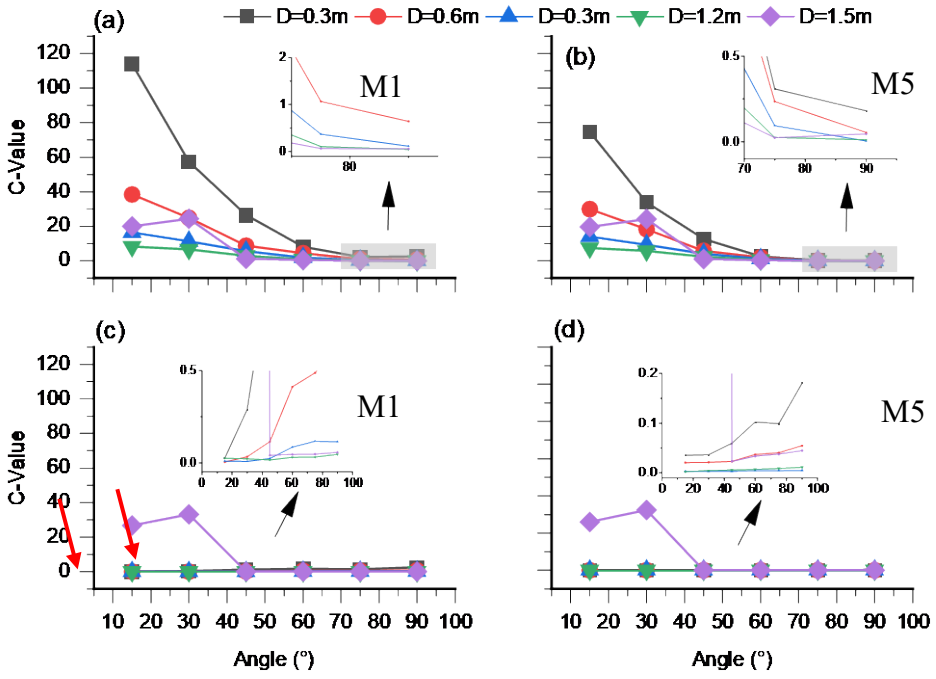

Figure 4-5. C-value analysis for simulation models with varying buried depth. For M1: (a) C-value considering pipe orientation; (c) C-value without considering pipe orientation. For M5: (b) C-value considering pipe orientation; (d) C-value with varying target radius, without considering pipe orientation.

As illustrated in Figure 4-4(a, b), when the horizontal pipe orientation is disregarded, the C-values for both models (across varying target radii) are exceptionally high, implying a poor fit to the actual hyperbolic reflections. As the oblique angle increases, for example, to 75°, i.e. the pipe alignment is getting close to being parallel to the GPR E-filed, the C-value decreases and becomes comparable to those obtained when considering the pipe orientation. Regarding the effect of target radius on the models, different trends were observed. For M1, the C-value increases as the target radius enlarges (Figure 4-4(a, c)), which is attributed to the negligence of this parameter in the model. For M5, without considering the pipe orientation, the C-value tends to become lower with the increasing radius when the oblique angle is relatively small (Figure 4-4(b)). When the oblique angle is relatively big, the C-value of different radii becomes similar. After angle correction, all C-values notably decrease, suggesting that incorporating target radius into the fitting models enhances accuracy. This improvement varies depending on the prior information on pipe orientation.

Similarly, for varying buried depths, the C-values of both models are generally high, particularly at smaller oblique angles, such as 15°, 30° and 45°. The varying buried depth shows a similar influence to these models. The C-value becomes larger with the decreasing depth. This is because the effect of target size and antenna separation on the fitting increases as depth decreases, so models that do not take these factors into account have increasing C-value. Two outliers (indicated by red arrows) appear when the oblique angles are 15° and 30° at a 1.5 m buried depth (Figure 4-5). These outliers are attributed to the combined effect of increasing oblique angles and buried depths which flatten the hyperbolic patterns. This flattening occurs in a layer where the signal sampling rate is inadequate to accurately capture the hyperbolic reflection, resulting in elevated C-values. After considering the oblique angle, the C-values for both models decrease substantially. When compared to the target radius, buried depth has a more significant effect on the C-value, especially when both the oblique angle and depth are relatively small. Aside from the sampling rate-induced anomalies, an increase in buried depth appears to reduce errors resulting from neglecting pipe orientation. However, in

practical applications, greater buried depth might lead to signal attenuation, thereby introducing more errors.

Finally, an analysis based on C-values—without angle corrections—reveals that the impact of oblique angle on hyperbolic reflections is not linear. For equal angle changes, the effect is much more prominent at smaller angles compared to larger ones, which could impact parameter estimation using the methods presented in this chapter.

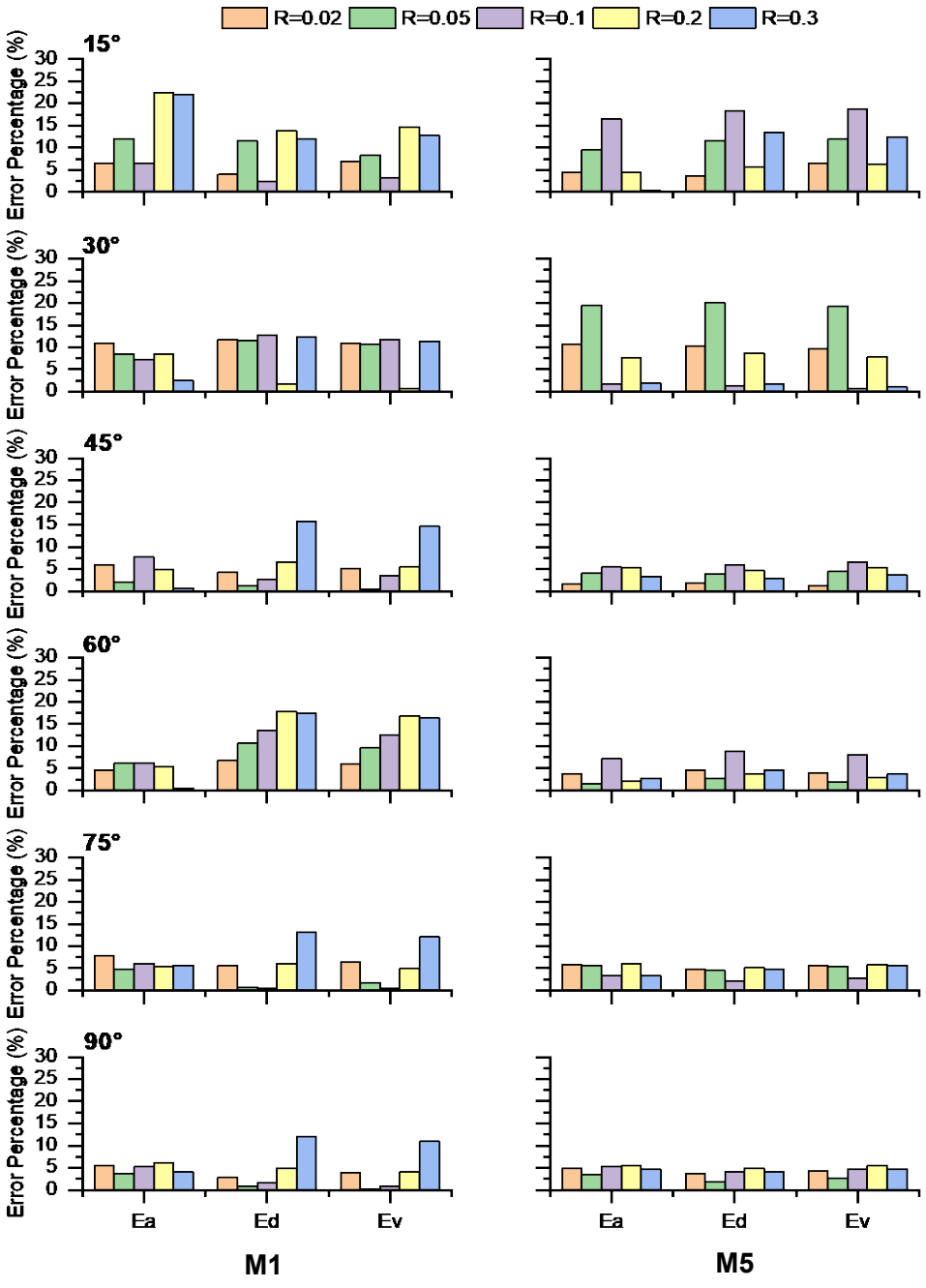

Figure 4-6. Errors in parameter estimation for simulation models with varying radius and pipe orientation. Ea – Errors in estimated pipe orientation; Ed – Errors in estimated depth; Ev – Errors in estimated wave velocity.

In Figure 4-6, the efficacy of the combined optimization algorithm—previously explained—is assessed for both M1 and M5 under varying target radii and oblique angles. The results indicate a direct correlation between smaller oblique angles and elevated estimation errors for both angle and depth parameters. For M5, it is noteworthy that estimation errors across all evaluated parameters—namely, orientation angle, buried depth, and wave velocity—converge within an acceptable 10% error margin when the oblique angle is greater than 45°. Contrary to M1, M5 manifests a diminished sensitivity to target radius variation, validated by a consistent performance in error rates. In M1, however, there is a discernible escalation in the error as the target radius increases. Interestingly, at target radii below 0.1 meters, like concrete rebars, both models provide comparable estimation accuracies, rendering either model viable for applications necessitating precise parameter estimations at such dimensions. The empirical data for M5 exhibit a marked uniformity in the optimization errors for both depth and velocity parameters, across varied target radii and oblique angles. This strongly implies an inherent robustness in the ability of M5 to estimate these parameters accurately.

In summation, the results depicted in Figure 4-5 provide clear evidence M5 is preferentially advantageous for achieving accurate and less radius-dependent parameter estimations, particularly when the oblique angle surpasses 45°. As can be observed, when the angle is less than 45°, the C-values for both hyperbolic models are quite high. As the angle exceeds 45 degrees, the C-value for M5 becomes significantly lower than that for M1, and it continues to stabilize as the angle increases further. The observations collectively corroborate the utility of the combined optimization algorithm in facilitating precise parameter estimations across a diversified set of conditions.

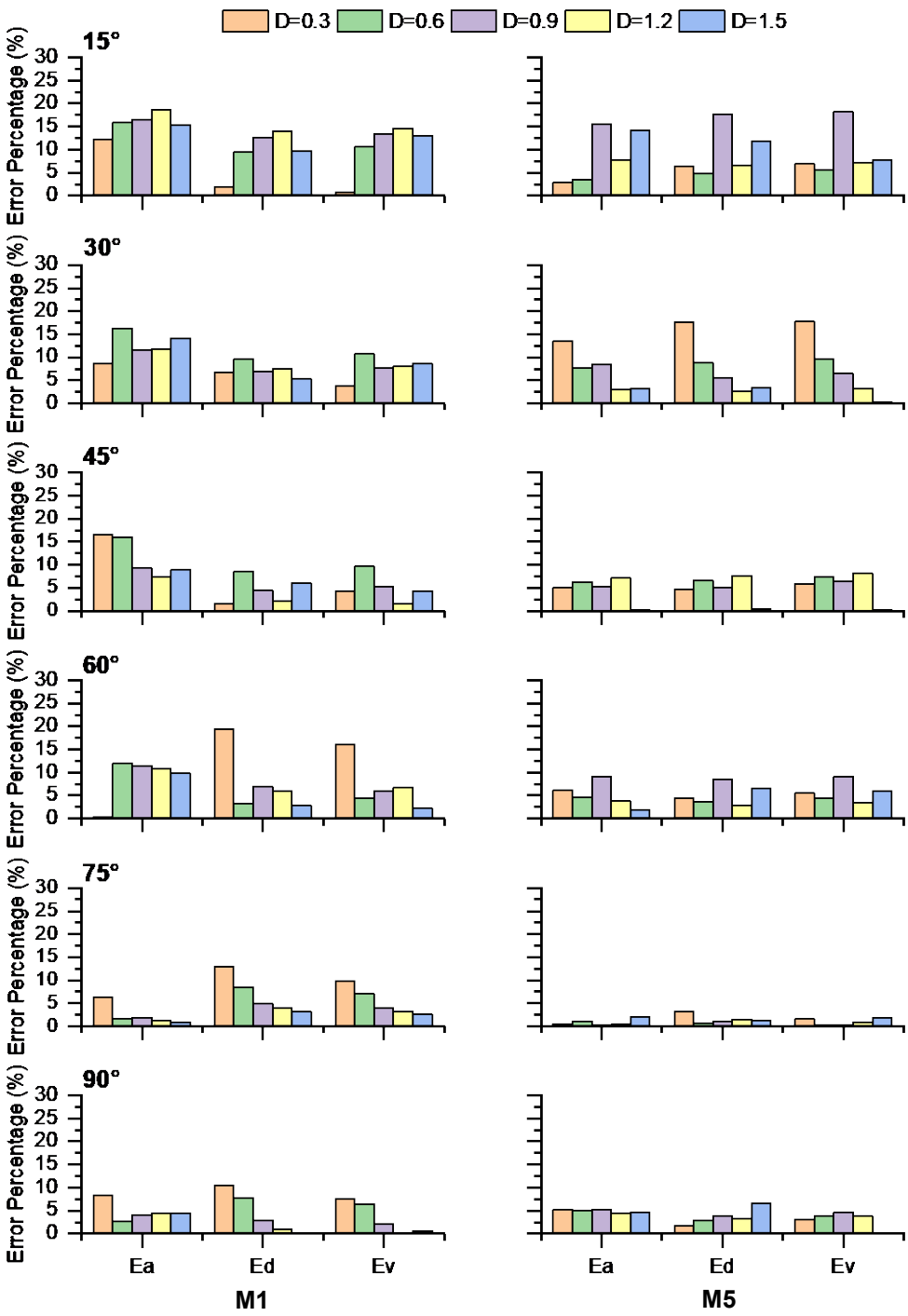

Figure 4-7. Errors in parameter estimation for simulation models with varying depth and pipe orientation. Ea – Errors in estimated pipe orientation; Ed – Errors in estimated depth; Ev – Errors in estimated wave velocity.

Figure 4-7 shows the impact of varying burial depths on the precision of parameter estimation, specifically in terms of pipe orientation, depth, and wave velocity, for both M1 and M5. Consistent with previous observations, estimation accuracy is inversely proportional to the size of the oblique angles for both M1 and M5. Remarkably, M1

manifests a pronounced sensitivity to changes in burial depth. The results indicate a degeneration in the estimation accuracy for all parameters as the burial depth diminishes. This degradation can be postulated to arise due to the relative increase in the target radius at shallower depths, a parameter not explicitly accounted for in M1. M5, in contrast, exhibits robust performance at oblique angles greater than 30°, irrespective of the burial depth. Both models tend to exhibit enhanced performance at greater burial depths. Specifically, when targets located at depths at a comparatively larger depth, i.e. 1.5 meters, the optimization error for both models tends to diminish, even at oblique angles as narrow as 30°. In summary, Figure 4-7 substantiates that the performance of M1 is acutely contingent upon the burial depth, unlike M5, which maintains a more consistent estimation accuracy across different burial depths and oblique angles. This evidential disparity reiterates the relative robustness of M5 in scenarios requiring versatile and depth-invariant parameter estimation. The results further show the utility of larger burial depths in enhancing the estimation precision for both models, a reference for subsurface applications.

The primary objectives of the numerical simulations in this chapter extend beyond a mere quantitative comparison of M1 and M5. The simulations are designed not only to assess the impact of varying parameters—such as target radius and burial depth—on these models but also to validate the effectiveness of the proposed combined optimization method, particularly in the context of pipe orientation estimation. The results confirm that M5, which incorporates target radius into its algorithm, consistently outperforms M1 when dealing with variations in target radius and burial depth. This contrast becomes increasingly evident as M1, which assumes targets to be point sources, accrues greater estimation errors under these conditions. Furthermore, both models display sensitivity to oblique angles; however, M5 is generally more robust, maintaining a satisfactory performance level even under suboptimal conditions. Therefore, based on our simulation data, M5 is recommended for scenarios where hyperbolic parameters can be reliably estimated. On the other hand, M1 still offers acceptable performance when the target radius is relatively small.

It is important to acknowledge the limitation that signal attenuation was not considered in these simulations. This represents a significant deviation from real-world, field-based experiments and could potentially affect the applicability and behavior of both models in practical settings. Finally, the simulation results lend strong support to the effectiveness of the combined optimization method, particularly in estimating pipe orientation alongside burial depth and wave velocity. This validation reinforces the proposed method as a valuable tool for comprehensive parameter estimation, especially in the term of pipeline management. These simulation outcomes set the stage for the subsequent field testing and verification, thereby providing holistic proof upon which to assess the proposed models and optimization methods under real-world conditions.

4.5. Field Experiments

4.5.1. Experimental Setup and Data Acquisition

To evaluate the applicability and precision of the proposed optimization method under real-world conditions, a field experiment was carried out at a test site constructed by IFSTTAR in France (Derobert and Pajewski, 2018; Dérobert and Pajewski, 2018). The experimental setup consisted of three trenches, each filled with varying compositions of silt, sand, and gravel. Within each trench, nine pipes were systematically buried across three distinct depth layers. Each layer housed a set of three pipes: an air-filled PVC pipe, a water-filled PVC pipe, and a metal pipe, all aligned parallel to each other. Figure 4-8 illustrates the spatial arrangement of these pipes both in plan and section views.

The study focused on metal pipes with a radius of 0.04 m, which were buried at 1.184 m, 1.659 m, and 2.395 m deep within the sand-filled trench. These metal pipes were anticipated to yield discernible curved reflections suitable for analysis. Data acquisition was executed using a GSSI 4000 control unit coupled with GSSI antennas operating at nominal center frequencies of 270 MHz and 400 MHz. Consistent with the simulation settings, six GPR traverses were devised to scan each metal pipe. These traverses were incrementally rotated around a fixed pivot from oblique angles of 15° to 90°, in 15°

intervals. Figure 4-9 presents the reflection profiles of a metal pipe buried at different within the sand trench, as captured from various oblique angles. It shall be noted that the gain was only applied for visualization.

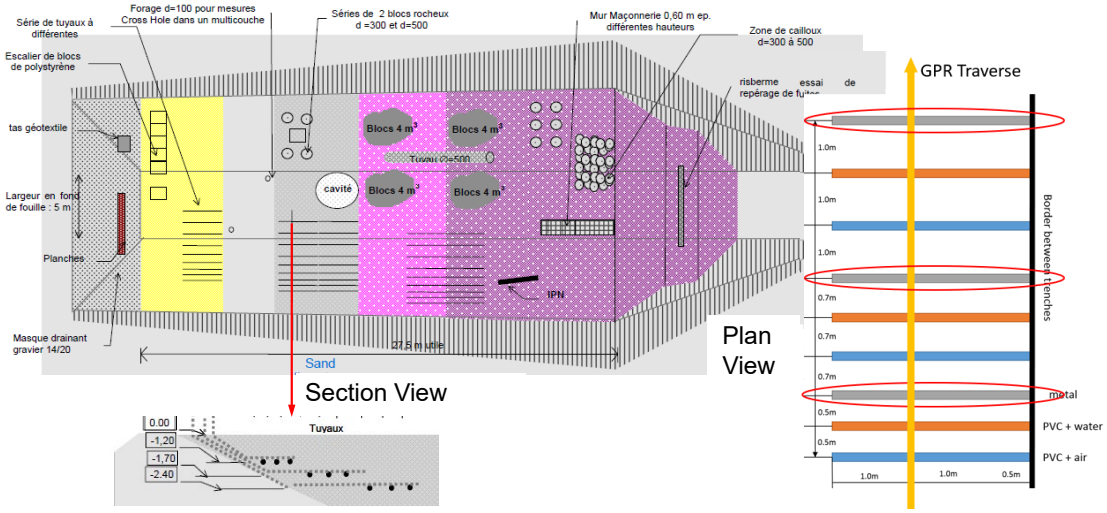

Figure 4-8. Geophysical test site at IFSTTAR, Nantes, France.

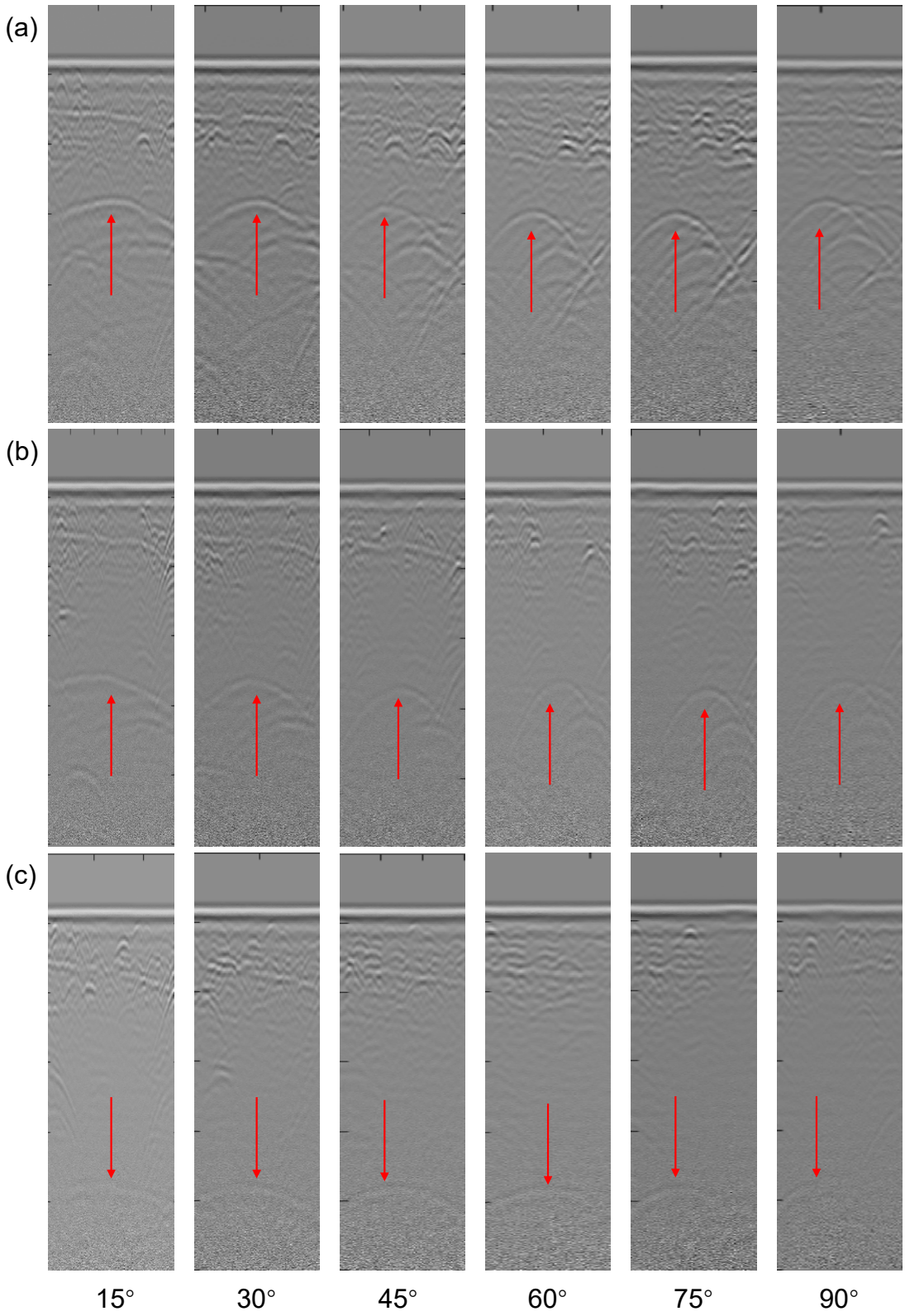

Figure 4-9. Metal pipe reflections in 1.184 m (a), 1.659 m (b), and 2.395 m (c), from 15° to 90° oblique angles in sand trench.

4.5.2. Hyperbolic Reflection Analysis

Utilizing the peak-echo extraction method previously described, hyperbolic reflections were successfully extracted. Figure 4-10 displays the reflections of the metal pipe, buried at a depth of 2.395 m, captured at varying oblique angles using a 270 MHz antenna. A discernible trend emerges: as the oblique angle increases, the curvature of the hyperbolic reflection flattens. This empirical observation is congruent with both the simulation results and extant literature on the subject (Lai et al., 2016b; Liu et al., 2018; Xie et al., 2018).

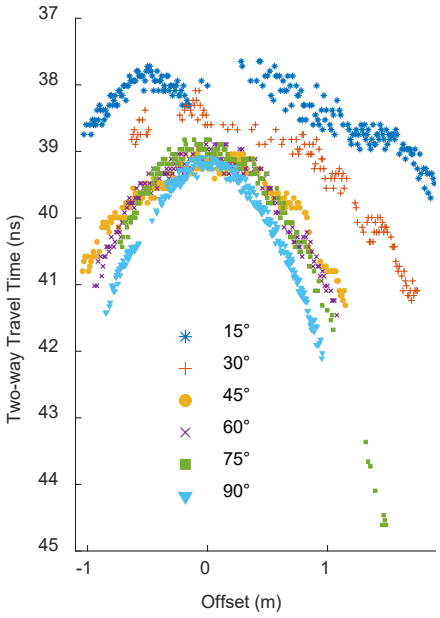

Figure 4-10. Reflections of the metal pipe in 2.395 m at different oblique angles in 270 MHz antenna.

4.5.3. Parameter Estimation and Model Performance

- Parameter Estimation Methodology

Transitioning to parameter estimation, the combined optimization approach proposed earlier was employed to estimate the pipe orientation, depth, and wave velocity. Figure 4-11 and Figure 4-12 exhibit the errors in estimating these parameters when using 270 and 400 MHz antennas, respectively. The detailed information is shown in Table 4-3 and Table 4-4. To evaluate the performance and reliability of hyperbolic fitting models, we employed two widely accepted statistical metrics: Mean Absolute Error (MAE) and Root Mean Square Error (RMSE). MAE measures the average magnitude of the errors

between predicted and observed values, without considering the direction of the error. It provides an easily interpretable, linear score that directly indicates the average error in the units of the parameter being estimated. RMSE, on the other hand, gives a sense of the error distribution's spread and penalizes larger errors more severely due to the squaring of individual error terms. The choice of using both MAE and RMSE stems from their complementary attributes. While MAE offers a straightforward and easily understandable measure of model performance, RMSE provides a more nuanced view by emphasizing larger errors. Together, these metrics provide a comprehensive assessment of model accuracy and robustness, which we present in Table 4-5 (for MAE) and Table 4-6 (for RMSE).

- Estimation Results and Analysis

As evident from the results, when the oblique angle exceeds 30°, the proposed method demonstrates commendable accuracy in estimating both pipe orientation and depth. In such scenarios, the estimation accuracy is subject to a variety of factors including depth, GPR center frequency, and the chosen hyperbolic fitting model. Importantly, the influence of depth on parameter estimation diverges between field experiments and simulations. In field conditions, contrary to what was found in simulation results, increasing depth does not improve estimation accuracy but tends to diminish it. This decline in accuracy is likely due to signal attenuation and scattering at greater depths, a phenomenon visible in Figure 4-9 and Figure 4-10. Such noise in the data predictably lowers the accuracy of parameter estimations.

According to Table 4-5 (MAE) and Table 4-6 (RMSE), M5 generally demonstrates lower errors in angle estimation across both 270 MHz and 400 MHz frequencies. However, the results for depth estimation are mixed, confirming the complex interplay between depth and estimation accuracy. This subtle behavior is especially pronounced in field experiments.

- Implications and Parameter Influences

Moreover, as depth increases, both M1 and M5 demonstrate a decline in the accuracy of pipe orientation estimation, while surprisingly showing better results for depth estimation. This suggests a differential impact of burial depth on the accuracy of estimating various parameters, such as orientation and depth. When comparing M1 and M5, the latter shows a slight edge in overall accuracy. This minor improvement may be attributed to the consideration of pipe radius and antenna separation of M5. However, the impact of these factors is less pronounced in field experiments where the radius and separation are relatively small compared to the burial depth (r = 0.04 m, S = 0.1 m). Our observations from Table 4-5 and Table 4-6 also highlight that operating at a higher frequency of 400MHz tends to reduce angle-estimation errors. This could be an essential parameter for consideration in future experimental setups.

For oblique angles that are relatively small, such as 15° and 30°, the error in estimating pipe orientation is considerably higher than for depth estimation. A plausible explanation for this divergence in error rates lies in the small values of the angle correction index $sin(\theta)$, e.g., $sin(15°) = 0.2588$. Here, even a small absolute error leads to a significant relative error. Furthermore, the term $x * sin(\theta)$ in the hyperbolic equations becomes negligible at small angles, minimizing its overall impact on parameter estimation. As a result, unlike angle estimation, parameters like depth and wave velocity are estimated with relatively low errors.

The consistency between MAE and RMSE as shown in Table 4-5 and Table 4-6 indicates that both metrics broadly support the same conclusions about model performance and the influence of various parameters. The RMSE is higher than the MAE in most cases, suggesting the influence of outliers or large errors, which could be influenced by the large error at a small oblique angle.

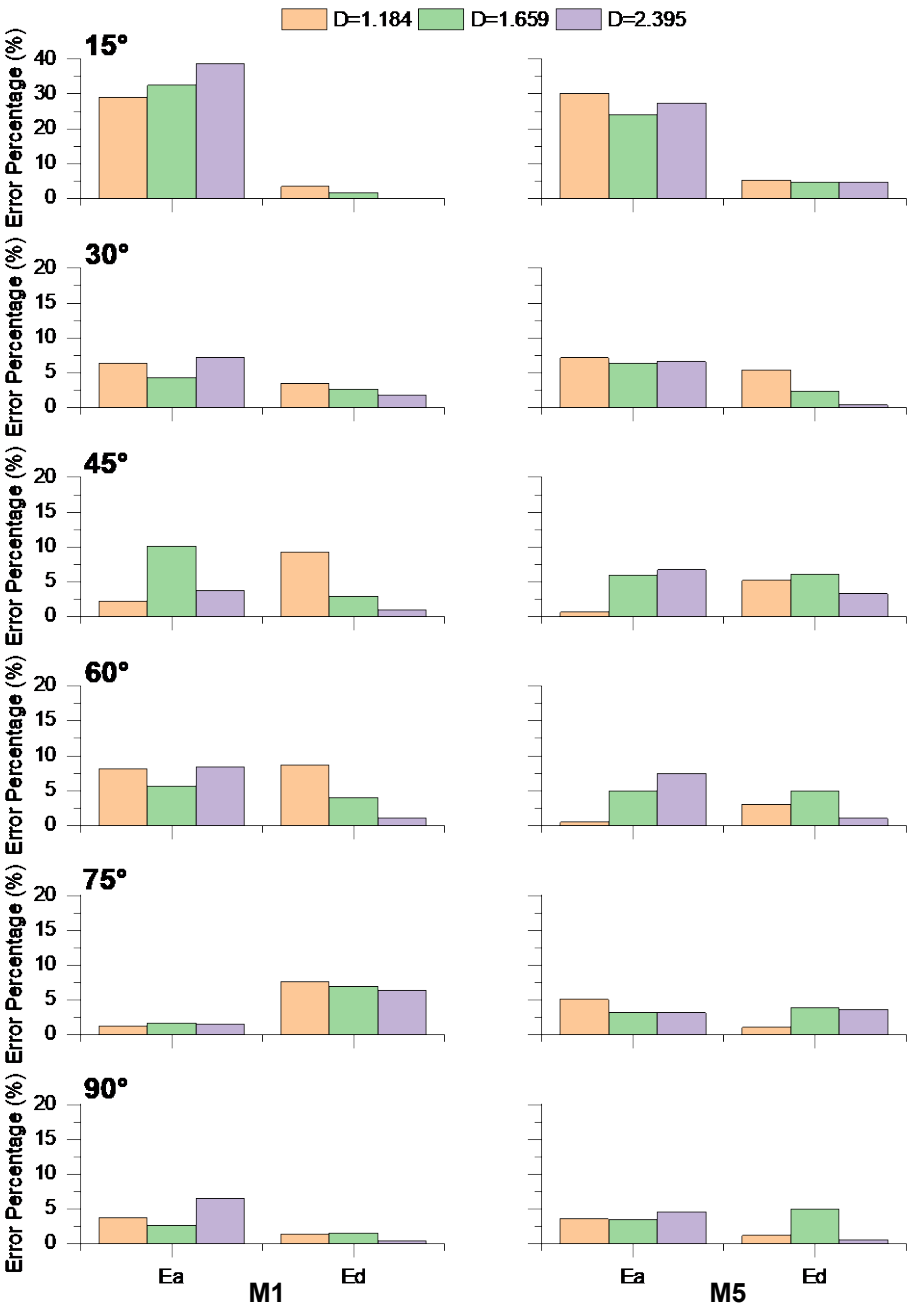

Figure 4-11. Errors of parameter estimation of field experiments using 270 MHz antenna. Ea – Errors in estimated pipe orientation; Ed – Errors in estimated depth; Ev – Errors in estimated wave velocity.

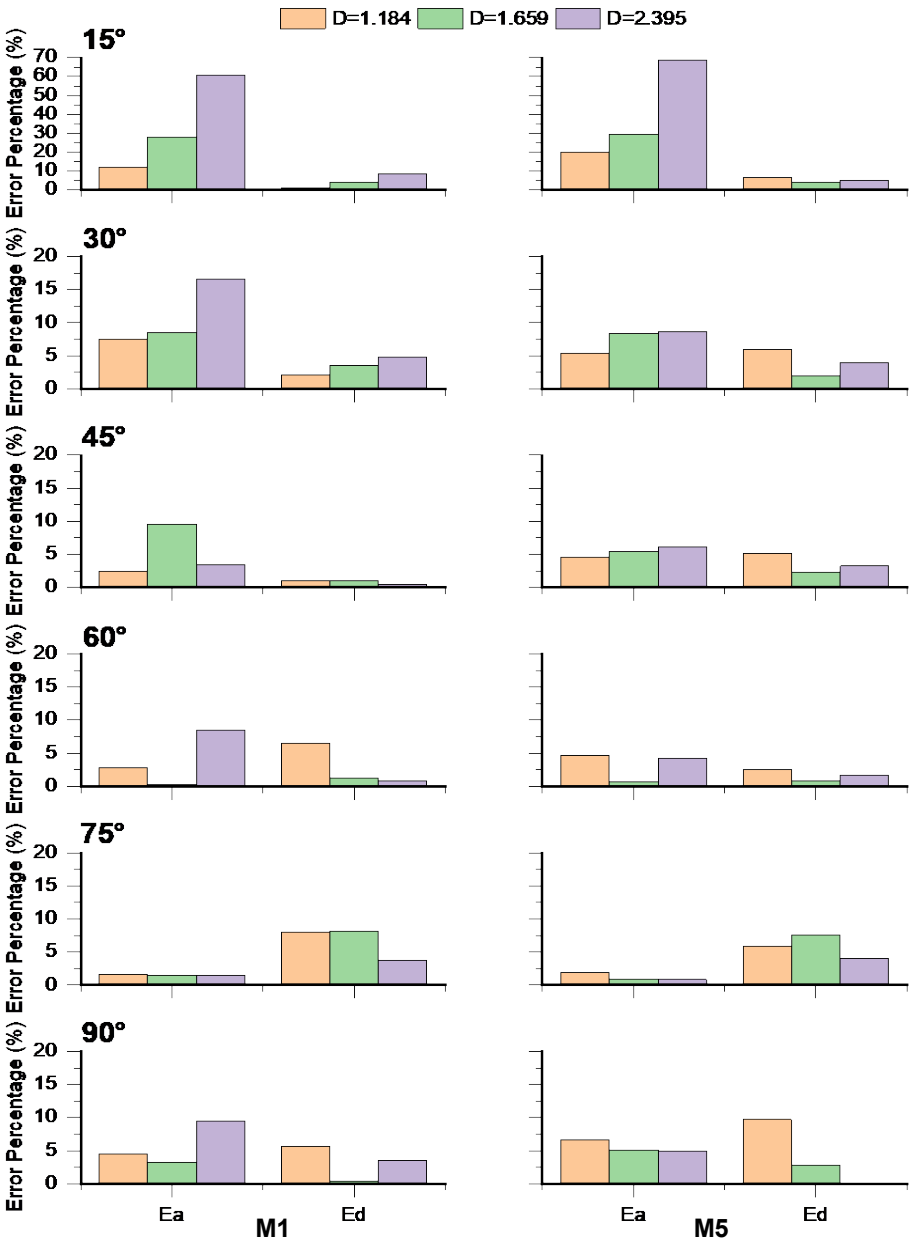

Figure 4-12. Errors of parameter estimation of field experiments using 400 MHz antenna. Ea – Errors in estimated pipe orientation; Ed – Errors in estimated depth; Ev – Errors in estimated wave velocity.

Table 4-3. Parameter estimation results using 270 MHz GPR. Est. O, Est. D, and Est. V are the estimated pipe orientation Sin(θ), buried depth D, and wave velocity V, respectively. Abs. Err. O and Err. O (%) are the absolute error of the estimation of the pipe orientation Sin(θ), and the corresponding percentage error, respectively.

Angle	Sin(θ)	Depth	M1							M5						
(°)		(m)	Est. O	Est. D	Est. V	Abs. Err.	Err. O (%)	Abs. Err. D	Err. D (%)	Est. O	Est. D	Est. V	Abs. Err.	Err. O (%)	Abs. Err. D	Err. D (%)
15	0.259	1.184	0.334	1.143	0.126	0.075	29.094	0.041	3.439	0.337	1.122	0.125	0.078	30.182	0.062	5.204
		1.659	0.343	1.633	0.126	0.084	32.526	0.026	1.547	0.321	1.739	0.134	0.062	23.953	0.080	4.814
		2.395	0.359	2.397	0.126	0.100	38.764	0.002	0.080	0.330	2.511	0.133	0.071	27.500	0.116	4.856
30	0.500	1.184	0.532	1.143	0.124	0.032	6.416	0.041	3.500	0.536	1.120	0.123	0.036	7.150	0.064	5.412
		1.659	0.522	1.616	0.122	0.022	4.332	0.043	2.601	0.532	1.620	0.123	0.032	6.360	0.039	2.381
		2.395	0.536	2.440	0.127	0.036	7.130	0.045	1.872	0.533	2.404	0.125	0.033	6.647	0.009	0.362
45	0.707	1.184	0.723	1.294	0.131	0.015	2.179	0.110	9.332	0.711	1.246	0.126	0.004	0.613	0.062	5.203
		1.659	0.635	1.706	0.122	0.072	10.166	0.047	2.860	0.665	1.760	0.126	0.042	5.932	0.101	6.080
		2.395	0.681	2.417	0.124	0.026	3.702	0.022	0.937	0.660	2.316	0.118	0.048	6.726	0.079	3.298
60	0.866	1.184	0.796	1.286	0.126	0.070	8.086	0.102	8.608	0.870	1.148	0.113	0.004	0.447	0.036	3.041
		1.659	0.818	1.593	0.117	0.048	5.575	0.066	4.003	0.823	1.577	0.117	0.043	4.958	0.082	4.940
		2.395	0.793	2.419	0.124	0.073	8.375	0.024	1.021	0.802	2.419	0.124	0.064	7.445	0.024	1.000
75	0.966	1.184	0.954	1.274	0.122	0.012	1.216	0.090	7.616	0.916	1.197	0.115	0.050	5.132	0.013	1.093
		1.659	0.949	1.775	0.126	0.017	1.752	0.116	6.986	0.934	1.723	0.122	0.032	3.270	0.064	3.862
		2.395	0.951	2.547	0.131	0.014	1.497	0.152	6.364	0.936	2.481	0.128	0.030	3.133	0.086	3.596
90	1.000	1.184	0.962	1.167	0.124	0.038	3.826	0.017	1.418	0.964	1.170	0.115	0.036	3.614	0.014	1.210
		1.659	0.974	1.686	0.124	0.026	2.608	0.027	1.627	0.966	1.743	0.114	0.034	3.439	0.084	5.049
		2.395	0.934	2.385	0.116	0.066	6.573	0.010	0.419	0.954	2.410	0.117	0.046	4.619	0.015	0.630

Table 4-4. Parameter estimation results using 400 MHz GPR.

Angle	Sin(θ)	Depth	M1							M5						
(°)		(m)	Est. O	Est. D	Est. V	Abs. Err. O	Err. O (%)	Abs. Err. D	Err. D (%)	Est. O	Est. D	Est. V	Abs. Err. O	Err. O (%)	Abs. Err. D	Err. D (%)
15	0.259	1.184	0.290	1.197	0.128	0.031	29.094	0.013	1.092	0.310	1.261	0.135	0.051	30.182	0.077	6.465
		1.659	0.331	1.731	0.131	0.073	32.526	0.072	4.313	0.336	1.730	0.131	0.077	23.953	0.071	4.259
		2.395	0.417	2.190	0.117	0.158	38.764	0.205	8.571	0.437	2.271	0.121	0.178	27.500	0.124	5.182
30	0.500	1.184	0.537	1.160	0.122	0.037	6.416	0.024	2.060	0.527	1.114	0.118	0.027	7.150	0.070	5.924
		1.659	0.543	1.717	0.127	0.043	4.332	0.058	3.506	0.542	1.693	0.125	0.042	6.360	0.034	2.046
		2.395	0.583	2.279	0.117	0.083	7.130	0.116	4.849	0.543	2.491	0.128	0.043	6.647	0.096	4.013
45	0.707	1.184	0.690	1.172	0.117	0.017	2.179	0.012	1.043	0.675	1.123	0.113	0.032	0.613	0.061	5.188
		1.659	0.639	1.643	0.117	0.068	10.166	0.016	0.967	0.669	1.698	0.121	0.038	5.932	0.039	2.353
		2.395	0.683	2.406	0.123	0.024	3.702	0.011	0.444	0.663	2.316	0.119	0.044	6.726	0.079	3.284
60	0.866	1.184	0.842	1.262	0.121	0.024	8.086	0.078	6.577	0.826	1.214	0.117	0.040	0.447	0.030	2.565
		1.659	0.868	1.680	0.123	0.002	5.575	0.021	1.286	0.860	1.644	0.121	0.006	4.958	0.015	0.887
		2.395	0.792	2.376	0.122	0.074	8.375	0.019	0.800	0.829	2.354	0.121	0.037	7.445	0.041	1.695
75	0.966	1.184	0.951	1.279	0.120	0.015	1.216	0.095	8.059	0.948	1.253	0.118	0.018	5.132	0.069	5.866
		1.659	0.951	1.795	0.126	0.015	1.752	0.136	8.221	0.957	1.785	0.125	0.009	3.270	0.126	7.618
		2.395	0.952	2.305	0.118	0.014	1.497	0.090	3.756	0.958	2.298	0.118	0.008	3.133	0.097	4.054
90	1.000	1.184	0.955	1.116	0.119	0.045	3.826	0.068	5.730	0.934	1.069	0.114	0.066	3.614	0.115	9.682
		1.659	0.968	1.666	0.122	0.032	2.608	0.007	0.416	0.949	1.612	0.118	0.051	3.439	0.047	2.858
		2.395	0.906	2.311	0.112	0.094	6.573	0.084	3.496	0.950	2.399	0.117	0.050	4.619	0.004	0.176

Table 4-5. Mean Absolute Error (MAE) of the optimized results.

Frequency (MHz)	Depth (m)	M1			M5		
		Err. O	Err. D	Err. D (%)	Err. O	Err. D	Err. D (%)
270	1.184	0.040	0.067	5.652	0.035	0.042	0.739
	1.659	0.045	0.054	3.271	0.041	0.075	2.293
	2.395	0.052	0.043	1.782	0.049	0.055	3.078
400	1.184	0.028	0.048	4.094	0.039	0.070	1.720
	1.659	0.039	0.052	3.118	0.037	0.055	1.775
	2.395	0.075	0.087	3.653	0.060	0.073	2.011

Table 4-6. Root Mean Square Error (RMSE) of the optimized results.

Frequency (MHz)	Depth (m)	M1		M5	
		RMSE O	RMSE D	RMSE O	RMSE D
270	1.184	0.047	0.076	0.043	0.047
	1.659	0.052	0.062	0.042	0.077
	2.395	0.060	0.066	0.051	0.068
400	1.184	0.030	0.059	0.042	0.075
	1.659	0.046	0.068	0.044	0.066
	2.395	0.088	0.109	0.081	0.084

4.6. Summary and Contribution

This chapter has shown the significance of hyperbolic fitting as an essential technique for estimating various parameters from the hyperbolic reflections of cylindrical objects, emphasizing the critical role of target orientation in enhancing the precision of these estimations. The contributions of this research are substantial, offering novel methodologies and insights into the complexities of parameter estimation using GPR:

1. The value of cost function (C-value) is used to quantitatively evaluate the impact of pipeline orientation on hyperbolic curves and fitting models. This analysis not only provides a deeper understanding of how orientation affects fitting precision but also introduces a robust metric for the evaluation and optimization of hyperbolic fitting methods.

2. Based on the established cost function, this study introduces a hybrid optimization approach that simultaneously estimates pipeline orientation, depth, and wave velocity, enhancing the applicability and accuracy of GPR data analysis. This method is operationalized through two distinct models: Model 1, which functions independently of prior information, and Model 5, which requires knowledge of target radius and antenna separation for enhanced accuracy. The effectiveness of these methods has been corroborated through comprehensive simulation and field experiments.

3. The research extends to a quantitative examination of how different pipeline radii and burial depths at various oblique angles influence the generation of hyperbolic curves. This investigation enriches the understanding of the factors that impact parameter estimation accuracy, thereby augmenting the robustness and reliability of the proposed fitting techniques. In the next chapter, another important factor of concern—wave velocity estimation in multi-layer media—is addressed, extending our investigation into increasing accuracy of parameter estimation under heterogenous subsurface conditions.

5. Chapter 5: Depth-Weighted Velocity Correction: Approach to Hyperbolic Fitting in Multi-Layered GPR Surveys

5.1. Chapter Overview

Following the developments of models discussed in previous chapters on hyperbolic fitting techniques and the integration of angle correction for improved parameter estimation, this chapter introduces a novel depth-weighted velocity correction algorithm that enhances the accuracy of velocity estimations within such complex layered media using hyperbolic fitting. Commonly, GPR hyperbolic fitting techniques operate under the assumption that the subsurface environment is homogeneous, an assumption that is frequently invalidated by the complexity encountered in actual field conditions. The utility of proposed algorithm spans not only improving the localization of subsurface utilities but also refining the characterization of material properties, including dielectric attributes and moisture content assessments. Designed to be adaptable across various hyperbolic models, the algorithm leverages available data on target radius and antenna separation, ensuring broad applicability. Through comprehensive numerical simulations and targeted laboratory experiments, which include a sensitivity analysis of the algorithm's parameters, the method's effectiveness is validated.

5.2. Introduction

Hyperbolic fitting techniques in GPR typically assume homogeneity in the surveyed area, a presumption that often does not hold in complex field conditions. This assumption introduces significant errors in velocity estimations when encountering heterogeneous layers such as multi-layered road surfaces or tunnel linings (Zhao and Al-Qadi, 2016; Zhu et al., 2024). Traditional methods do not effectively address the variations in dielectric properties across different layers, leading to inaccurate subsurface characterizations.

In fields like extraterrestrial exploration where GPR is employed, the use of air-coupled antennas introduces air as an intermediary medium, further complicating hyperbolic fitting results for sub-surface wave velocity estimations. Although specialized algorithms have been developed to correct these distortions, they remain rarely in engineering contexts and are often too complex and computationally intensive for practical engineering applications (Liu et al., 2023; Persico et al., 2015; Rappaport, 2007).

To mitigate these challenges, this chapter presents a novel depth-weighted velocity correction algorithm designed to refine wave velocity estimations within heterogeneous media. This simple yet effective algorithm adjusts velocity estimations to better reflect the layered media conditions found in typical GPR surveys, enhancing the accuracy of hyperbolic fitting methods. Validated through extensive numerical simulations and laboratory experiments, this algorithm addresses the inaccuracies in traditional hyperbolic fitting methods (M1 and M5) in previous chapters and extends its application to more complex and practical engineering scenarios, promoting its adoption for terrestrial and extraterrestrial subsurface explorations.

5.3. Methodology

The workflow of the proposed method is illustrated in Figure 5-1**.** The process begins with data pre-processing to correct the raw GPR signals, which includes time-zero correction, Dewow, and DC-shift removal. Subsequently, it is essential to determine the thickness and relative permittivity of the overlaying layers. These parameters can be obtained through various methods depending on the experimental setup: the extended common midpoint method (XCMP) is primarily used in simulation experiments, while direct measurements and the reflected-amplitude method are utilized in field experiments. Alternatively, these parameters can also be sourced from reference tables or construction documents. This flexibility in method selection helps accommodate the different practical constraints and data availability in each scenario. Following parameter determination, hyperbolic reflections are identified and optimized,

facilitating the estimation of the total burial depth and the bulk velocity influenced by all layers. Finally, the depth-weighted velocity correction is applied, adjusting the EM wave velocity and the corresponding relative permittivity for the layer containing the target object.

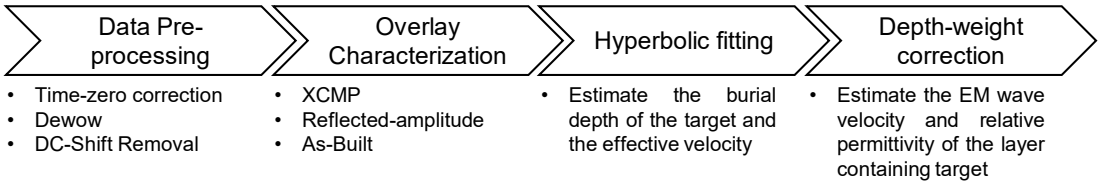

Figure 5-1. Procedure of the proposed method.

5.3.1. Extended Common Midpoint Method (XCMP)

The CMP method is one of the multi-offset profile data processing techniques originally developed in the seismic field (Schneider, 1984; Annan, 2004). Leng and Al-Qadi (Leng and Al-Qadi, 2014), and Zhao and Al-Qadi (Zhao and Al-Qadi, 2016) developed this method and introduced it to GPR detection. The basic setup of the XCMP method and the corresponding geometry using two bistatic systems can be seen in Figure 5-2. T_1/R_1 and T_2/R_2 are the transmitter/receiver pairs for Channel 1 (CH1) and Channel 2 (CH2), respectively. The antenna separations for CH1 and CH2 are S_1 and S_2, respectively. Both antenna pairs share the same midpoints, P_1 and P_2. ε_0, ε_1, and ε_2 are the relative permittivity of air, layer 1 and layer 2, respectively, and v_0, v_1, and v_2 are the corresponding EM wave velocity. H_1 and H_2 are the thickness of layer 1 and layer 2, respectively. t_1 and t_2 are the time EM wave travels in the layer 2 for CH1 and CH2, respectively.

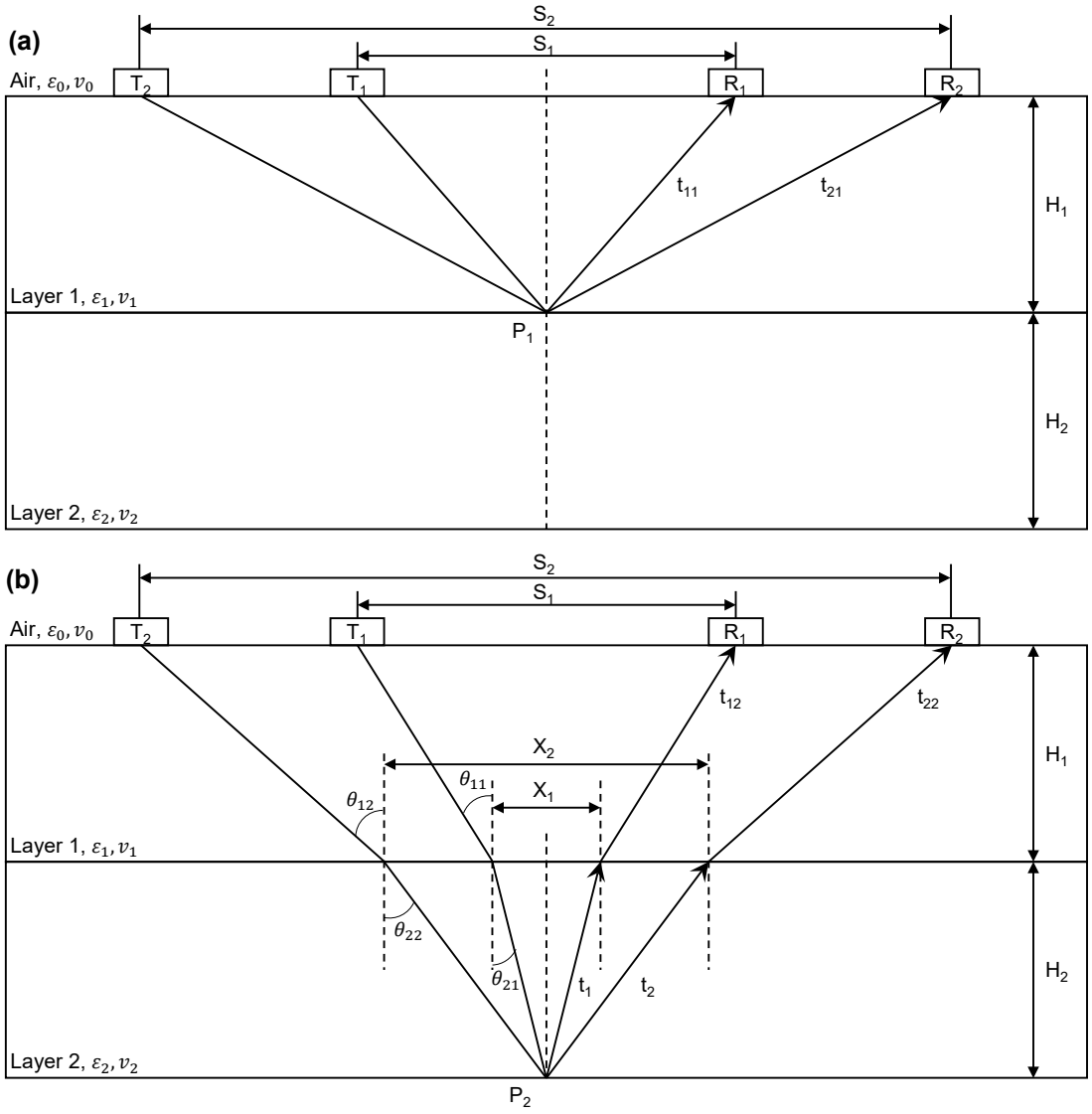

Figure 5-2. XCMP setup and geometry using two bistatic GPR systems: (a) reflection in a single layer; and (b) reflection and refraction in double layers.

The XCMP problem has four unknowns: the thickness (H_1 and H_2) and relative permittivity (ε_1 and ε_2) of two layers. Obtaining bottom reflection times at layer 1 and layer 2 from two channels can fully determine the four unknowns. Based on Snell's Law of reflection and refraction, thickness and relative permittivity can be expressed as:

$$t_{11} = \frac{2\sqrt{H_1^2 + \frac{S_1^2}{4}}}{v_1}, \tag{5.1}$$

$$t_{21} = \frac{2\sqrt{H_1^2 + \frac{S_2^2}{4}}}{v_1}, \tag{5.2}$$

$$v_i = \frac{c_0}{\sqrt{\varepsilon_i}}, \tag{5.3}$$

where t_{11} and t_{21} are the EM wave travel times in from T_1 and T_2 to R_1 and R_2 in layer 1, respectively (Figure 5-2 (a)), c_0 = 3×10^8 m/s is the EM waves velocity in vacuum. It shall be noted that the above equations do not work when total reflection occurs or antenna separation is too large.

The solution of the thickness and relative permittivity of layer 2 is derived as:

$$\left(\frac{S_1 - x_1}{2H_1}\right)^2 = \frac{\varepsilon_1 t_1^2 (x_1^2 - x_2^2)^2}{\varepsilon_1 t_1^2 (x_1^2 - x_2^2)^2 - c_0^2 x_1^2 (t_1^2 - t_2^2)^2} - 1, \tag{5.4}$$

$$\left(\frac{S_2 - x_2}{2H_1}\right)^2 = \frac{\varepsilon_1 t_2^2 (x_1^2 - x_2^2)^2}{\varepsilon_1 t_2^2 (x_1^2 - x_2^2)^2 - c_0^2 x_2^2 (t_1^2 - t_2^2)^2} - 1, \tag{5.5}$$

$$t_1 = \Delta t_1 + \frac{2\sqrt{H_1^2 + \frac{S_1^2}{4}}}{v_1} - \frac{2\sqrt{H_1^2 + \frac{(S_1 - x_1)^2}{4}}}{v_1}, \tag{5.6}$$

$$t_2 = \Delta t_2 + \frac{2\sqrt{H_1^2 + \frac{S_2^2}{4}}}{v_1} - \frac{2\sqrt{H_1^2 + \frac{(S_2 - x_2)^2}{4}}}{v_1}, \tag{5.7}$$

where Δt_1 and Δt_2 are the time difference of the EM wave between the reflections at bottoms of layer 1 and layer 2 for CH1 and CH2, respectively, as shown in Figure 5-2 (b). x_1 and x_2 are the distances between the incidence point and reflection point of CH1 and CH2, respectively. The detailed equation of the derivation process can refer to the literature (Leng and Al-Qadi, 2014). It shall be noted that if the layer is relatively smaller than the wavelength, Δt_1 and Δt_2 may not be resolved due to pulse overlapping (Zhao and Al-Qadi, 2016).

From Equation (5.4) to Equation (5.7), four unknown x_1, x_2, t_1 and t_2 may be resolved numerically. The thickness and relative permittivity of layer 2 then can be determined by:

$$\varepsilon_2 = \frac{c_0^2(t_1^2 - t_2^2)}{x_1^2 - x_2^2}, \tag{5.8}$$

$$H_2 = \frac{\left[\sqrt{(c_0 t_1 / 2\sqrt{\varepsilon_2})^2 - \left(\frac{x_1}{2}\right)^2} + \sqrt{(c_0 t_2 / 2\sqrt{\varepsilon_2})^2 - \left(\frac{x_2}{2}\right)^2}\right]}{2}. \tag{5.9}$$

5.3.2. Depth-weighted Velocity Correction

Utilizing hyperbolic reflection models 1 (M1) and 5 (M5) developed in Section 2.5, this section applies a global optimization algorithm based on the MVO to estimate electromagnetic (EM) wave velocity and burial depth for cylindrical targets. Equation (3.8) facilitates the calculation of media's relative permittivity, which aids in predicting the water content within various layers. However, these models inherently assume medium homogeneity within each layer—an assumption often contradicted in complex scenarios like pipelines beneath layered structures such as asphalt or tunnel linings. In such cases, traditional estimates reflect a bulk velocity, influenced by the composite effects of all encountered layers. To address these discrepancies and enhance the precision of subsurface utility detections, this section introduces a depth-weighted velocity correction method. This method adjusts the bulk wave velocity from hyperbolic fitting to better represent the actual EM wave velocity or relative permittivity of the layer surrounding the targets, ensuring that GPR survey results align more closely with real-world conditions.

The proposed method, termed the depth-weighted velocity correction algorithm, advances the interpretation of bulk wave velocity by considering the distinct contributions of each layer. The algorithm assumes that the bulk wave velocity is a depth-weighted average of the velocities corresponding to each layer, a concept

formulated on the premise that the proportional distance traveled by EM waves through each layer aligns with the layer's relative thickness. This relationship is mathematically captured by the equation:

$$v_e = \frac{H_1}{H}v_1 + \frac{H_2}{H}v_2 + \cdots + \frac{H_n}{H}v_n = \sum_{i=1}^{n}\frac{H_i}{H}v_i, \tag{5.10}$$

where v_e is the bulk velocity estimated by the hyperbolic fitting through M1 and M5, H is the burial depth of the round-shaped target, H_i and v_i are the thickness and the EM wave velocity of the i^{th} layer, respectively.

Therefore, utilizing the bulk velocity v_e and burial depth H estimated by hyperbolic fitting, with the thickness and wave velocity of the overlying layers predicted by the XCMP method, the wave velocity in the layer where the target is located, v_n, can be determined using the following equations:

$$H_n = H - \sum_{i=1}^{n-1} H_i, \tag{5.11}$$

$$v_n = (v_e - \sum_{i=1}^{n-1}\frac{H_i}{H}v_i) \times \frac{H}{H_n}, \tag{5.12}$$

where H_n represents the thickness of the layer containing the target.

Incorporating this depth-weighted correction into GPR data analysis largely reduces the inaccuracies introduced by inhomogeneous media and boosts the reliability of geophysical assessments across various environmental settings. The efficacy of this approach is supported by validation through both controlled simulations and laboratory experiments.

5.4. Numerical Simulation

Similar to Chapters 3 and 4, the numerical simulation was also conducted using gprMax. The simulations were organized into two groups based on the number of overlying layers—single and double layers, respectively. To investigate the influence of layer

thickness and dielectric properties on the algorithm, two-parameter variation schemes were implemented: one varying the thickness while holding the relative permittivity constant, and another varying the relative permittivity while maintaining consistent thickness across the layers. The specific parameters for these schemes are detailed in Table 5-1 and Table 5-3. For all simulations, the TE mode was chosen, and a Ricker wavelet with a 1.5 GHz center frequency was used for excitation. To minimize dispersion effects and facilitate the selection of layer reflection signals via the XCMP method, the wavelength of the excitation signal was ensured to be less than the thickness of any layer (Zhao and Al-Qadi, 2016). The simulations were conducted over a 30 ns time window with a 0.01 m step interval. The separation distances for T1/R1 and T2/R2 were set to 0.1 m and 0.2 m, respectively.

5.4.1. Single Overlying Layer Cases

Following the two schemes described previously, the thickness and relative permittivity were varied independently to explore their impacts on the proposed methods. The specific simulation parameters are detailed in Table 5-1. In this group, four sets of parameters were established, generating eight distinct cases, as illustrated in Figure 5-3.

Table 5-1. Parameters for single overlying layer simulation cases. Case Num. is the number of the case. P_1 and P_2 are the relative permittivity of layer 1 and the layer enveloping the target, respectively. H_1 and H_2 are the thicknesses of layer 1 and the layer enveloping the target, respectively.

Case Num.	P_1	P_2	H_1 (m)	H_2 (m)
1	2	20	0.3	0.7
2	3	8		
3	4	7		
4	5	6		
5	3	8	0.2	0.8
6			0.3	0.7
7			0.4	0.6
8			0.5	0.5

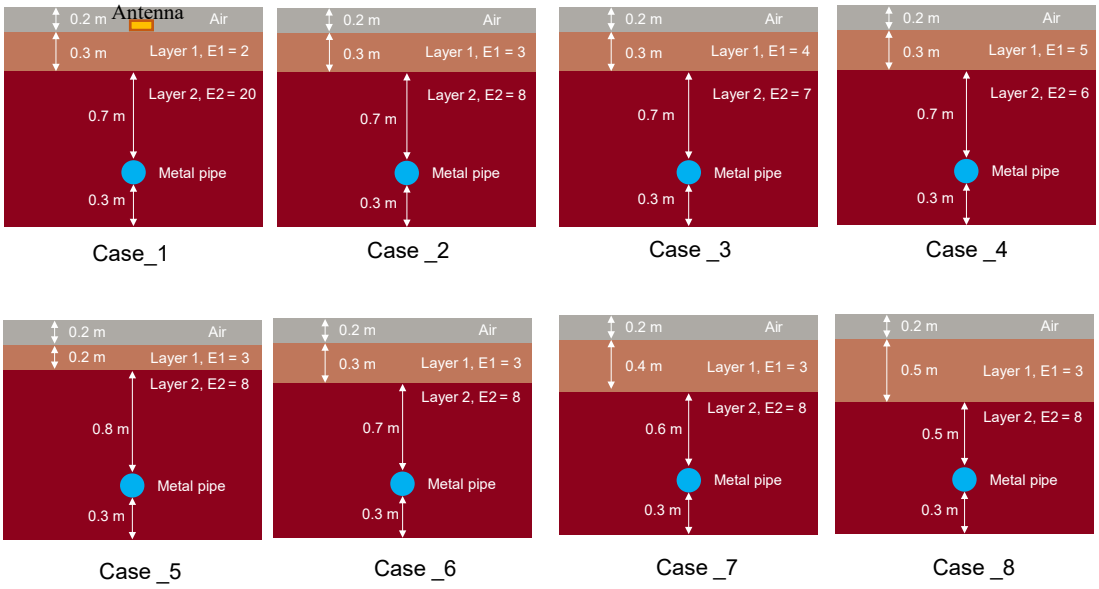

Figure 5-3. The simulations cases with a single overlying layer.

Following the workflow detailed in Section 5.3, the wave velocity of the media containing the target can be obtained. The parameter-estimation results from the cases with varying relative permittivity and layer thickness are shown in Table 5-2.

Table 5-2. Parameter estimation results of two hyperbolic fitting models in the single layer simulations. Model is the number of the hyperbolic model. The case represents the number of simulation cases (Figure 5-3). Vt is the import value of the EM wave velocity in the layer containing the target. Ve is the bulk velocity estimated by the hyperbolic fitting and Err_Ve is the corresponding percentage error. CV is the velocity corrected by the proposed method (Equation (3.17)) and Err_CV is the corresponding percentage error. H is the total depth estimated by hyperbolic fitting and Err_H is the corresponding percentage error.

Model	Case	Vt (m/ns)	Ve (m/ns)	Err_Ve (%)	CV (m/ns)	Err_CV (%)	H (m)	Err_H (%)
1	1	0.0670	0.1099	**63.94**	0.0796	**18.81**	1.3123	31.23
	2	0.1060	0.1318	**24.35**	0.1164	**9.79**	1.1028	10.28
	3	0.1133	0.1309	**15.52**	0.1235	**9.02**	1.0739	7.39
	4	0.1224	0.1331	**8.75**	0.1327	**8.43**	1.0616	6.16
2	1	0.0670	0.1060	**58.12**	0.0731	**8.98**	1.2652	26.52
	2	0.1060	0.1265	**19.34**	0.1080	**1.93**	1.0574	5.74
	3	0.1133	0.1255	**10.75**	0.1155	**1.89**	1.0289	2.89
	4	0.1224	0.1275	**4.17**	0.1247	**1.92**	1.0164	1.64
1	5	0.1060	0.1261	**18.97**	0.1157	**9.13**	1.1017	10.17
	6		0.1318	**24.35**	0.1164	**9.79**	1.1028	10.28
	7		0.1376	**29.82**	0.1173	**10.69**	1.1002	10.02
	8		0.1436	**35.48**	0.1188	**12.11**	1.0952	9.52
2	5		0.1210	**14.16**	0.1088	**2.68**	1.0562	5.62
	6		0.1265	**19.34**	0.1080	**1.93**	1.0574	5.74
	7		0.1320	**24.53**	0.1069	**0.86**	1.0549	5.49
	8		0.1377	**29.91**	0.1055	**0.45**	1.0498	4.98

To analyze the parameter estimation results further, the percentage errors of the bulk and corrected velocities were depicted in Figure 5-4. The results reveal that M1 and M5 display similar trends: the error in bulk velocity significantly decreases as the disparity in dielectric properties between the two media layers reduces. For instance, in simulation case 1, where the dielectric contrast between layers is substantial (relative permittivity of 2 and 20), the errors in bulk wave velocity were as high as 63.94% and 58.12%, respectively. In contrast, in scenarios with minimal dielectric differences (relative permittivity of 5 and 6), the errors dropped to 8.75% and 4.17%, respectively. M5 consistently demonstrated higher accuracy across all simulation cases, a benefit

derived from including variables such as target radius and antenna separation in its calculations (He and Lai, 2024).

The comparison of the corrected results indicates a significant reduction in error for both models under various simulation conditions. Specifically, in simulation case 1, which displayed the highest initial errors, the correction algorithm reduced the error for M1 from 63.94% to 18.81% and for M5 from 58.12% to 8.98%. In simulation cases 3-5, while the corrected error rates exhibited minor fluctuations corresponding to changes in dielectric properties between layers, they remained relatively stable—M1 averaged around 9% and M5 around 2%. This pattern indicates that the impact of dielectric property differences on the algorithm's performance is more substantial when these differences are significant. As these disparities reduce, their influence on the accuracy of the proposed algorithm correspondingly diminishes. The variance in correction efficacy can be explained by the theoretical foundations underlying the proposed velocity correction method. This method assumes that the wave propagates along a straight line in an inhomogeneous medium. According to Snell's law, as depicted in Figure 5-2, when there is a greater disparity between the dielectric properties of the upper and lower layers of the medium, the actual wave propagation route deviates more significantly from the hypothetical straight line. Consequently, the error associated with the correction increases. Conversely, when the disparity between the dielectric properties is smaller, the actual wave propagation path aligns more closely with the assumed straight line, resulting in a smaller correction error.

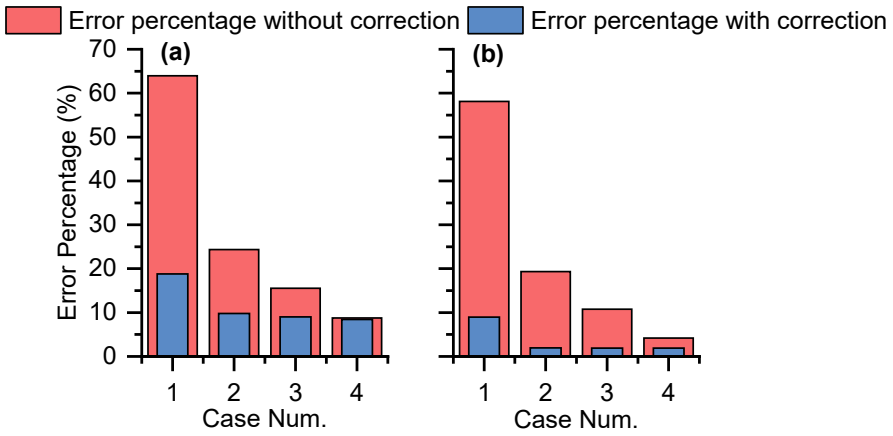

Figure 5-4. Percentage error in velocity estimations with and without correction across models (a) M1 and (b) M5 for single-layer cases with varying relative permittivity.

In the analysis of single overlying layer cases, we examined how variations in layer thickness affect the performance of the proposed algorithm. As shown in Figure 5-5, both M1 and M5 exhibit a nearly linear increase in the error of bulk wave velocity as the thickness of the media layers becomes comparable. This trend highlights the significant influence of media thickness on velocity estimations, underscoring the robustness of the proposed method. Notably, M5 consistently delivered superior accuracy across all simulations.

Figure 5-5 also illustrates notable improvements in the error associated with the corrected wave velocity compared to the uncorrected velocity for both models. However, a divergence in behavior emerges as the layers' thickness equalizes: the corrected velocity error in M1 slightly increases, while it decreases substantially in M5. This variation suggests that the object radius parameter differentially affects the accuracy of hyperbolic fitting models based on the relative thickness of the surrounding media. Further exploration of how the object radius interacts with media properties could yield essential insights, potentially enhancing the efficacy of the velocity correction method.

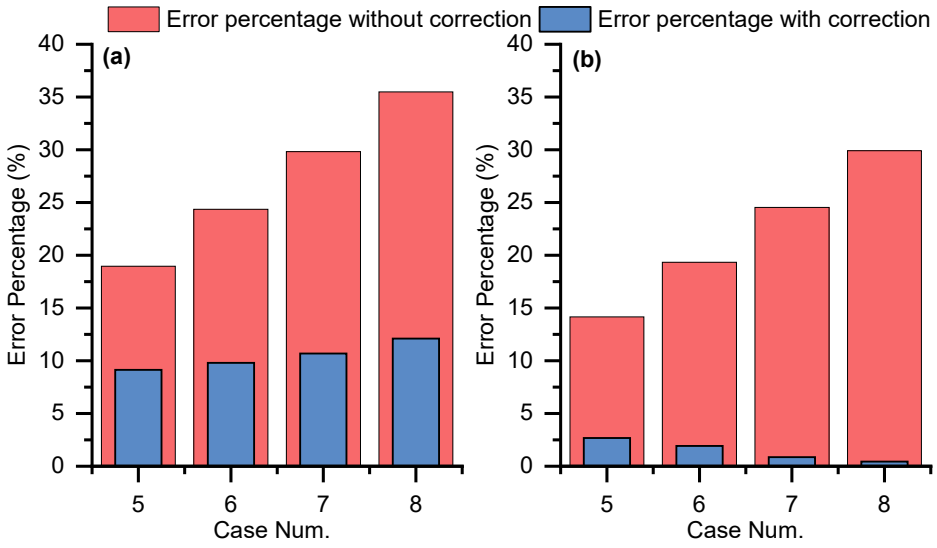

Figure 5-5. Percentage error in velocity estimations with and without correction across models (a) M1 and (b) M5 for single-layer cases with varying layer thickness.

The accuracy of depth estimations, as shown in Figure 5-6, reveals differences between M1 and M5. M5 consistently provides more accurate depth results than M1, which, in turn, enhances the precision of the velocity corrections derived from these models. Figure 5-6(a) illustrates the performance of the models with varying relative permittivity, showing that higher permittivity generally results in higher error rates, in line with previous research (He and Lai, 2024). This effect diminishes as the disparity in relative permittivity between the two layers decreases, improving the accuracy of depth estimations. Conversely, Figure 5-6(b) shows that depth estimation errors reduce when the two media layers converge towards equal thickness, especially when the layer with higher relative permittivity is thinner and the one with lower relative permittivity is thicker.

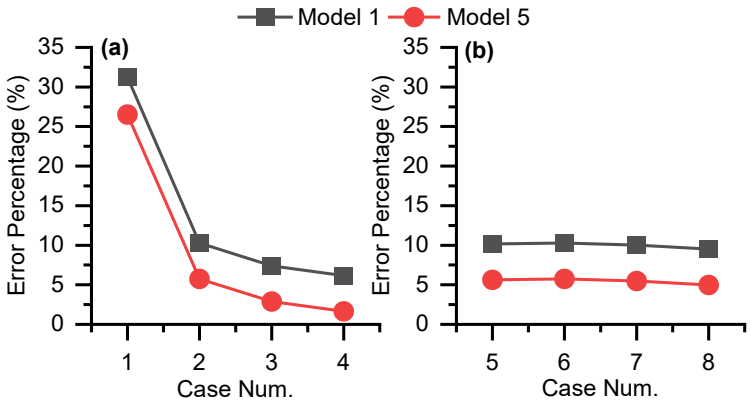

Figure 5-6. Percentage error in depth estimation across models (a) M1 and (b) M5 for single-layer cases.

5.4.2. Double Overlying Layer Cases

In this section, the proposed velocity-correction algorithm was evaluated using double-layer simulation cases. Three sets of parameters were established, generating six distinct cases. The specific parameters for these cases are detailed in Table 5-3, and the cases themselves are depicted in Figure 5-7.

Table 5-3. Parameters for double overlying layer simulation cases. Case Num. is the number of the case. P_1, P_2, and P_3 are the relative permittivity of layer 1, layer 2, and the layer enveloping the target, respectively. H_1, H_2, and H_3 are the thickness of layer 1, layer 2, and the layer enveloping the target, respectively.

Case Num.	P_1	P_2	P_3	H_1 (m)	H_2 (m)	H_3 (m)
9	2	4	18	0.2	0.2	0.6
10			8			
11			5			
12	2	4	8	0.1	0.1	0.8
13				0.2	0.2	0.6
14				0.3	0.3	0.4

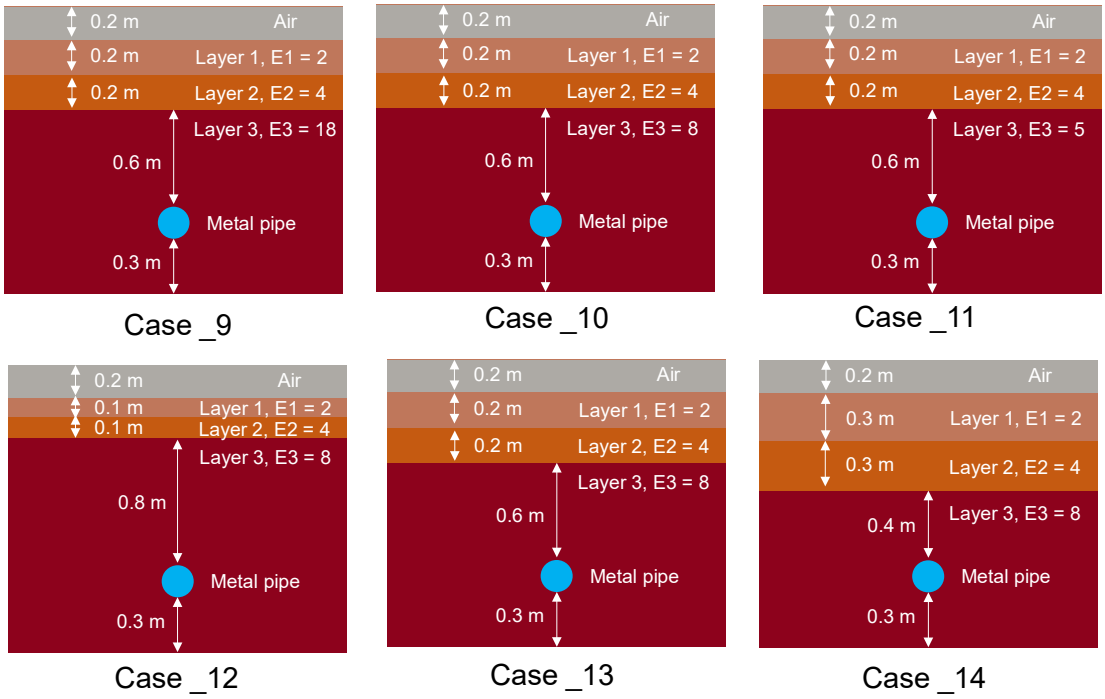

Figure 5-7. The simulations cases with double overlying layers.

As in Section 5.4.1, the estimated results from these simulations are compiled in Table 5-4, highlighting both the uncorrected and corrected velocity errors. This comparative analysis is visualized in Figure 5-8 and Figure 5-9, which illustrate the error percentages for velocity with and without the corrections. Additionally, the depth estimation results are depicted in Figure 5-10.

Table 5-4. Parameter estimation results of two hyperbolic fitting models in the double-layer simulations.

Model	Case	Vt (m/ns)	Ve (m/ns)	Err_Ve (%)	CV (m/ns)	Err_CV (%)	D (m)	Err_D (%)
1	9	0.1341	0.1593	**18.81**	0.1465	**9.30**	1.0785	7.85
	10	0.1060	0.1409	**32.93**	0.1187	**12.03**	1.1229	12.29
	11	0.0707	0.1159	**64.02**	0.0855	**21.04**	1.2568	25.68
2	9	0.1341	0.1528	**13.97**	0.1350	**0.71**	1.0335	3.35
	10	0.1060	0.1353	**27.65**	0.1083	**2.22**	1.0774	7.74
	11	0.0707	0.1117	**58.07**	0.0775	**9.72**	1.2107	21.07
1	12	0.1060	0.1290	**21.70**	0.1178	**11.12**	1.1261	12.61
	13		0.1409	**32.93**	0.1187	**12.03**	1.1229	12.29
	14		0.1543	**45.57**	0.1231	**16.18**	1.1132	11.32
2	12		0.1239	**16.89**	0.1110	**4.68**	1.0811	8.11
	13		0.1353	**27.65**	0.1083	**2.22**	1.0774	7.74
	14		0.1482	**39.82**	0.1063	**0.25**	1.0685	6.85

The simulation results of the double-layer cases closely mirror those observed in the single-layer configurations, showing the robustness and adaptability of the proposed velocity-correction method across varying subsurface conditions. Both models, M1 and M5, exhibited similar trends in error reduction for bulk and corrected velocities, as well as depth estimations, regardless of the number of layers involved. This consistency is significant as it validates the method's efficacy not only in simplified, single-layer scenarios but also in more complex, double-layer environments.

While the specific error percentages and trends align closely with those of the single-layer cases, the double-layer configurations further demonstrate the method's reliability in handling interactions between multiple layers, which are common in real-world subsurface evaluations. The results indicate that the velocity-correction method effectively mitigates errors associated with complex layer interactions, thereby enhancing the accuracy of subsurface material characterization. This is evident in scenarios where disparities in layer properties could potentially complicate data interpretation and analysis.

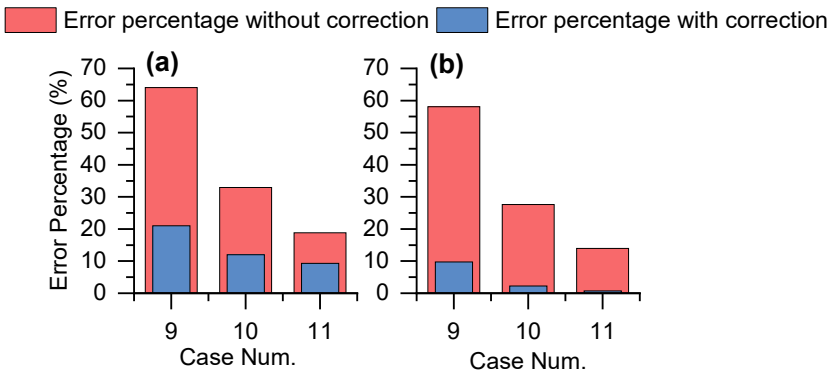

Figure 5-8. Percentage error in velocity estimations with and without correction across models (a) M1 and (b) M5 for double-layer cases with varying relative permittivity.

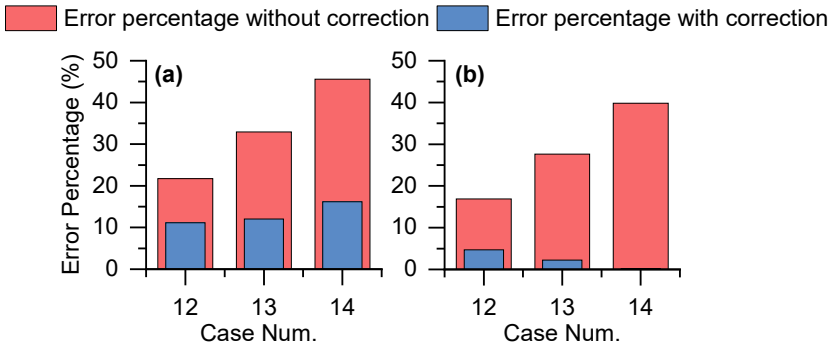

Figure 5-9. Percentage error in velocity estimations with and without correction across models (a) M1 and (b) M5 for double-layer cases with varying layer thickness.

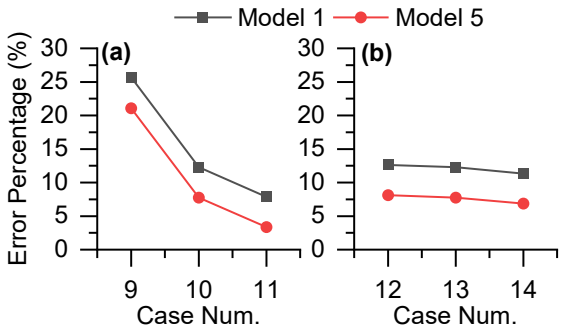

Figure 5-10. Percentage error in depth estimation across models (a) M1 and (b) M5 for double-layer cases.

5.5. Laboratory Experiments

To validate the proposed method under real-world conditions, controlled laboratory experiments were conducted across three different scenarios. The properties of the layers used in these experiments are detailed in Table 5-5. It is important to note that

the thickness of all three layers was measured using a tape measure, the relative permittivity of the sand was determined using a time-domain reflectometer (TDR), and the relative permittivity of the asphalt and polyoxymethylene (POM) was measured using the reflected-amplitude method (Wang et al., 2018), where the relative permittivity of the surface layer (ε_1) is determined from the ratio of the amplitude of the reflection from the surface layer (A_1) to that from a copper plate (A_p), according to Snell's law of reflection, as described by the equation $\varepsilon_1 = [(1 + A_1 / A_P)/(1 - A_1 / A_P)]^2$.

Table 5-5. Parameters of different layers. H and P are the thickness and relative permittivity of the corresponding material, respectively.

Layer material	Thickness H (m)	Relative permittivity P
Sand	0.1	2.3
Asphalt	0.1	4.4
POM	0.08	2.9

Figure 5-11 illustrates the configurations for the three laboratory experiment scenarios. These experiments utilized a GPR system from Geophysical Survey Systems, Inc. (GSSI), which operated at a central frequency of 2 GHz with antenna separations of 0.04 m. In each scenario, a metal pipe with a diameter of 0.03 m was buried at a depth of 0.1 m within dry sand. Scenario 1 (S1) involved the GPR operating directly on the surface of the dry sand, providing a baseline measurement. In Scenario 2 (S2), a 0.1 m thick asphalt layer was overlaid on the dry sand to simulate a single-layer condition, while Scenario 3 (S3) added a 0.08 m thick POM layer on top of the asphalt, simulating a double-layer condition. It is crucial to note that the GPR traverse was perpendicular to the pipe. Discussions regarding the application of hyperbolic fitting in situations where the GPR traverse is not perpendicular to the pipe are detailed in previous research (Lai et al., 2016b).

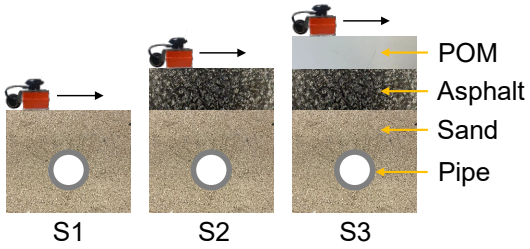

Figure 5-11. Laboratory experiments setup.

Figure 5-12 presents the radargrams of the three experimental scenarios. With the addition of each layer, the hyperbolic reflections become deeper and weaker, while the interfaces between different layers are distinctly marked with lines of varying colors. The radargrams clearly show that as layers are added, the nature of the hyperbolic reflections changes not only in terms of depth but also in their shape.

Utilizing the peak-echo selection method, the hyperbolic reflections extracted are also displayed in Figure 5-12. Upon adding an asphalt layer, the shape of the hyperbolic reflections visibly flattened—a direct result of the increased depth and altered wave velocity due to the new layer composition. Consequently, using hyperbolic fitting to estimate depth and velocity under these conditions naturally results in measurements that reflect both the increased depth and the combined velocity characteristics influenced by the presence of the asphalt.

When a second layer of POM is added on top of the asphalt, the change in the reflections' shape becomes subtler, merely flattening slightly. This is attributed to the POM's thinner profile and its relative permittivity of 2.9, which is slightly higher than that of sand but lower than asphalt, resulting in less pronounced changes. These variations in hyperbolic reflections across different layered structures illustrate that traditional hyperbolic fitting, which assumes homogeneous media, is limited under non-uniform conditions. This necessitates further methods to accurately correct the results.

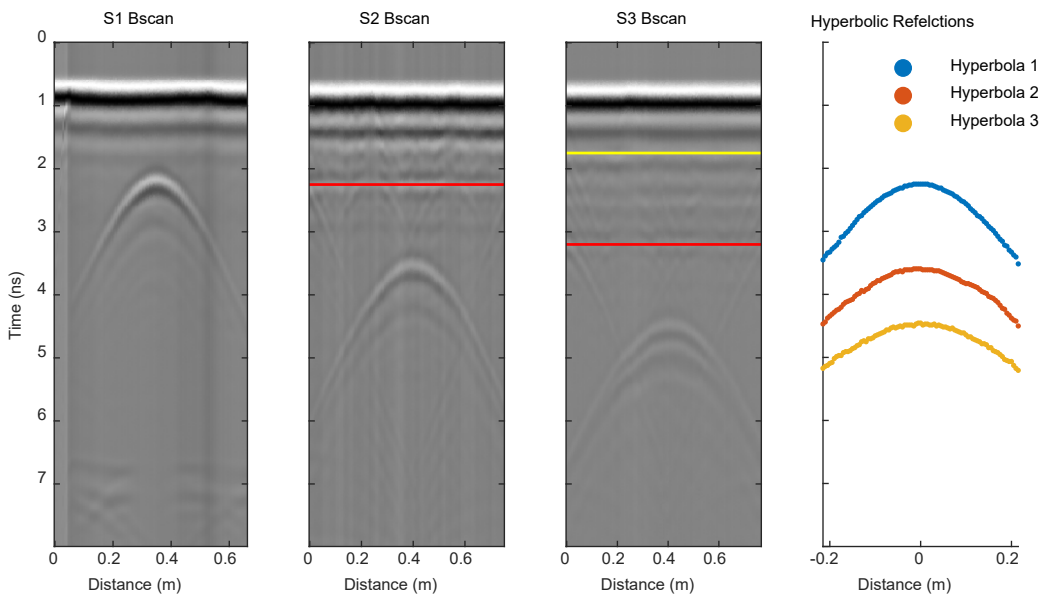

Figure 5-12. Radargrams of the three scenarios and the extracted hyperbolic reflections. Red lines indicate the interface between asphalt and sand. The yellow line donates the interface of POM and asphalt.

After extracting the hyperbolic reflections, the two hyperbolic fitting models were applied to estimate the burial depth and the bulk EM wave velocity. Subsequently, the correction algorithm outlined in Section 5.3.2 was employed to adjust the bulk velocity to reflect the wave velocity of the media where the pipe is buried—dry sand in these experiments.

Table 5-6 presents the results from the laboratory experiments applying the proposed velocity correction algorithm to both single-layer and double-layer cases. An in-depth analysis of these results is crucial. Initially, the velocity estimation results for S1 using M1 and M5 indicate that both models performed commendably: M1 had an error of 5.26%, while M5 had a smaller error of 3.19% in estimating the wave velocity. However, after introducing an asphalt layer, the errors escalated to 9.00% (M1) and 13.76% (M5), respectively. This significant increase underscores the challenges posed by assuming a uniform medium. Following the application of the correction algorithm, the errors were substantially reduced to 4.15% and 2.93%, closely mirroring the results of S1 using M1 and M5 and thus affirming the effectiveness of the proposed method.

When examining the more complex double-layer case results, a slight increase in velocity estimation was observed, attributable to the additional POM layer, which has

a relative permittivity of 2.9 and is sandwiched between the asphalt and dry sand layers. Despite being thinner than both the asphalt and sand layers, the POM layer contributed to a minor increase in velocity estimation. The velocity correction performance of M1 in the double-layer case was suboptimal, with accuracy decreasing from an initial 8.01% error to 8.6% after correction, indicating a deterioration in performance. This underscores the limitations of M1, particularly when handling multiple layers with similar dielectric properties and thicknesses, a challenge also highlighted in simulation experiments. In contrast, M5 demonstrated robust performance, significantly reducing the error rate from 11.33% to 2.17%.

The results consistently indicate that M5 provides more accurate velocity estimates than M1, benefiting from the inclusion of target radius and antenna separation considerations. These parameters significantly influence accuracy when they align closely with the burial depth of the target; their omission leads to more pronounced errors (He and Wai-Lok Lai, 2024). However, in practical measurement scenarios where acquiring precise values for these parameters is challenging, M1 remains a useful alternative, offering straightforward velocity estimation and correction despite higher error margins.

Moreover, the addition of the asphalt layer notably increased the depth estimation error, primarily due to the layer's higher relative permittivity and the presence of non-smooth boundaries. These factors intensify estimation challenges, as further corroborated by references (He and Wai-Lok Lai, 2024). Conversely, the introduction of the POM layer reduces depth estimation errors, benefiting from its lower relative permittivity and larger thickness, which collectively aid in reducing error.

Table 5-6. Parameter estimation results of laboratory experiments. Ht indicates the reference value of the burial depth, measured by tape.

Model	Scenarios	Vt (m/ns)	Ve (m/ns)	Err_Ve (%)	CV (m/ns)	Err_CV (%)	Ht (m)	H (m)	Err_H (%)
1	S1	0.1977	0.2081	5.26	-	-	0.10	0.1144	14.40
	S2		0.1799	**9.00**	0.2059	**4.15**	0.2	0.2421	21.05
	S3		0.1818	**8.04**	0.2147	**8.60**	0.28	0.3124	11.57
2	S1		0.1914	3.19	-	-	0.1	0.1047	4.70
	S2		0.1705	**13.76**	0.1919	**2.93**	0.2	0.2289	14.45
	S3		0.1753	**11.33**	0.2020	**2.17**	0.28	0.2991	6.82

The numerical and laboratory experiments validated the proposed depth-weighted velocity correction algorithm, demonstrating its effectiveness in improving velocity estimation in layered environments. However, the method assumes GPR waves travel linearly through each layer, which simplifies the modeling but doesn't fully account for wave refraction and reflection at interfaces, as governed by Snell's law. This approximation may introduce errors, particularly in environments with large dielectric contrasts where the actual wave propagation path significantly deviates from the assumed straight-line trajectory. Additionally, the acquisition of layer parameters through various methods like XCMP and direct measurement introduces variability in accuracy. While results have been promising in up to two layers, extending this approach to more complex multi-layered scenarios will require precise parameter determination. Future studies should focus on refining these assumptions and expanding the algorithm's applicability to diverse subsurface conditions.

5.6. Summary and Contribution

This chapter has addressed the traditional limitations of hyperbolic fitting, which is commonly used to estimate burial depth and wave velocity from hyperbolic reflections but typically relies on the assumption of homogeneous media. Recognizing the inadequacy of this assumption in practical scenarios, this chapter introduces a novel depth-weighted velocity correction algorithm that adapts hyperbolic fitting for

application to multi-layered subsurface structures. The primary contributions of this chapter are as follows:

1. The research quantitatively assesses the errors in velocity estimation that arise when hyperbolic fitting is directly applied to layered media. It investigates how variations in media parameters affect these errors, offering a better understanding of the challenges posed by non-homogeneous environments.

2. The proposed correction algorithm effectively reduces velocity estimation errors in layered structures and enhances the velocity-estimation accuracy for target-contained layers. It is versatile, and compatible with different hyperbolic fitting models, which can be adapted based on the availability of specific parameters such as target radius and antenna separation.

3. A comparative analysis of two hyperbolic fitting models that incorporate the velocity correction algorithm is provided. The study outlines clear recommendations for selecting appropriate models based on the specific characteristics of the layered scenarios encountered. This comparative insight is instrumental in guiding practitioners in choosing the most suitable ray-path model for accurate subsurface investigations.

6. Chapter 6: Impact of Hyperbolic Integrity on Hyperbolic Fitting in GPR Measurement

6.1. Chapter Overview

This chapter addresses a less explored aspect of GPR hyperbolic fitting: the impact of hyperbolic integrity on fitting accuracy. Utilizing optimization-based models, this study systematically examines the effects of data modification through uniform point deletion (change of horizontal sampling of A-scans) and biased point removal (biased and assymetric hyperbolic reflections). Such modifications simulate potential data integrity issues that can arise in practical GPR applications. The methodology allows for the empirical estimation of key parameters, such as burial depth and wave velocity, and assesses their stability under conditions of up to 40% point deletion. The analysis incorporates statistical tools like mean value, standard deviation, and R-squared to evaluate the robustness of parameter estimations. This chapter further explores the influence of variable factors such as burial depth, dielectric permittivity, and target radius on the estimations. Through detailed numerical simulations and field experiments, the findings enhance understanding of how to maintain the reliability of GPR data analysis even in complex underground conditions. These insights are crucial for advancing the precision of subsurface explorations and refining GPR techniques to adapt to diverse environmental challenges.

6.2. Introduction

While hyperbolic fitting provides a straightforward approach to deducing these parameters, such as burial depth and wave velocity, it often assumes ideal conditions that do not typically exist in field scenarios. This simplification leads to uncertainties in the results, especially in complex environments like layered structures or areas with subsurface heterogeneity. Factors such as equipment stability, operational settings, and the inherent properties of the survey area can introduce errors in data acquisition and

processing. Moreover, subsurface heterogeneity contributes to additional challenges by causing EM wave scattering, thereby complicating the interpretation process.

In practical applications, the integrity of hyperbolic reflections is frequently compromised due to various factors such as sparse data from limited antenna configurations or obscured reflections by adjacent subsurface utilities, or trade-off of horizontal resolution and vehicle speed in multi-channel GPR system. These conditions necessitate a rigorous examination of hyperbolic data's reliability and accuracy in parameter estimation. Recognizing these challenges, this chapter discusses the development of robust methodologies to assess and mitigate the impacts of data alteration on hyperbolic fitting accuracy.

By employing optimization-based models, this study systematically investigates the stability of hyperbolic fitting under conditions of uniform and biased point deletion—common scenarios in sparse data environments and areas with dense subsurface utility layouts. Additionally, the influences of varying burial depths, dielectric permittivity, and target radii on hyperbolic fitting accuracy were analyzed through a comprehensive set of numerical simulations and field experiments.

6.3. Methodology

Further to models introduced in Section 2.5, this section employs hyperbolic reflection models 1 (M1) and 5 (M5), leveraging a global optimization algorithm based on the MVO. By implementing the MVO algorithm repeatedly, we accumulate a substantial dataset of parameter estimations. The empirical distribution of these estimations is subsequently derived, providing a probabilistic characterization of estimated parameter. This distribution serves as the basis for a comprehensive analysis to hyperbolic integrity, enabling us to quantify the reliability of hyperbolic-reflection-based interpretations in GPR data analysis.

The core of our investigation into the impact of hyperbolic integrity involves executing multiple optimizations of the parameter set $[D_0, v]$ against a specific dataset $[x_i, t_i]$. This iterative approach is continued until a stable parameter distribution is observed. The

empirical distribution's density then informs the probability that the estimated parameters [D_0, v] are an accurate reflection of the actual dataset [x_i, t_i]. For this study, we have determined that 5000 repetitions of the optimization process are adequate for the parameter distributions of both simulated and experimental datasets to achieve stability.

6.3.1. Statistical Parameters for Analyzing Hyperbolic Integrity Impact

Prior to the introduction of statistical parameters, it is critical to delineate the primary focus of the present research. The objective herein is not to ascertain the absolute accuracy of parameter estimations yielded by hyperbolic fitting models; rather, it is to explore the complex alterations in hyperbolic integrity upon such estimations. Through the optimization-based hyperbolic fitting, a distribution of parameters is derived, inherently characterized by probabilistic tendencies. These distributions reveal the probabilities associated with the estimated parameters, thereby expressing the impact in the data analysis.

- Mean Value and Standard Deviation in Evaluating Hyperbolic Integrity Impact

In statistical analysis, the mean value and standard deviation are crucial metrics used to describe the distribution of a data set. The mean provides a measure of the central tendency, indicating the average outcome, while the standard deviation reflects the amount of variability or dispersion from the mean. Mathematically, they are defined as:

$$Mean(mu) = \frac{1}{m}\sum_{i=1}^{m} y_i , \tag{6.1}$$

$$StandardDeviation(\sigma) = \sqrt{\frac{1}{m-1}\sum_{i=1}^{m}(y_i - \mu)^2} , \tag{6.2}$$

where y_i represents the estimated depth or velocity at i^{th} optimization, mu is the mean value of the parameter estimation, and m is the number of runs.

By analyzing how the mean value and standard deviation change as points are systematically removed from the hyperbolic reflection—reflecting various degrees of

hyperbolic integrity—we can gauge the impact of data completeness on the accuracy and certainty of parameter estimates.

- R-Squared (R^2) in Evaluating Hyperbolic Integrity Impact

R-squared, also known as the coefficient of determination, is a statistical measure that represents the proportion of variance for a dependent variable that's explained by an independent variable or variables in a regression model. It is a key output of regression analysis and ranges from 0 to 1, where a higher value generally indicates a better fit of the model to the data. Mathematically, R-squared is defined as:

$$R^2 = 1 - \frac{SS_{res}}{SS_{tot}}, \tag{6.3}$$

$$SS_{res} = \sum_{i=1}^{n} (T_i - t_i)^2, \tag{6.4}$$

$$SS_{tot} = \sum_{i=1}^{n} (T_i - \bar{T})^2, \tag{6.5}$$

where SS_{res} is the sum of squares of residuals, representing the variation that the model fails to capture, SS_{tot} is the total sum of squares, which measures the total variation in the observed data, T_i represents the actual TTT collected by GPR and t_i represents the TTT calculated by the hyperbolic fitting models at position x_i, $\bar{T}$ is the mean of the actual TTT, and n is the number of points on hyperbolic-reflection.

R-squared provides a measure of how well the observed outcomes are replicated by the model, based on the proportion of total variation of outcomes explained by the model. In this chapter, R-squared is employed to assess the robustness of hyperbolic fitting under varying conditions of integrity. By evaluating how R-squared changes as we systematically reduce the number of points on the hyperbolic reflection in two ways, uniform point deletion and biased point removal, we can infer the sensitivity of our depth and velocity estimations to the integrity of the hyperbolic reflection pattern, which is essential in GPR data interpretation.

6.4. Numerical Simulation

Similar to previous chapters, the numerical simulation was also conducted using gprMax. The TE mode was specifically chosen for simulation. This mode was facilitated by employing a Ricker wavelet centered at 900 MHz for signal excitation. The time window was set to 30 ns and the step interval at 0.01 m, with an antenna separation of 0.05 m, thereby collecting a comprehensive dataset of 171 A-scan data points. Within this simulation framework, a representative model was selected to illustrate our approach to quantifying hyperbolic integrity impact. The chosen model features a cylindrical pipe with a radius of 0.1 m, buried at a depth of 0.9 m within a medium with a relative permittivity of 5, corresponding to an EM wave velocity of 0.1341 m/ns.

Upon extracting the hyperbolic reflection within the GPR radargram, the raw dataset was obtained. This dataset was then manipulated to imitate varying degrees of hyperbolic integrity. As previously outlined, two distinct methodologies were employed to degrade the integrity: one by uniformly eliminating points across the hyperbolic reflection (del 1), and the other by progressively removing points from one side (del 2). To systematically explore the spectrum of reflection integrity, we established ten discrete levels—spanning deletions from 10% to 90% in increments of 10%, with an additional level at 95% deletion. Figure 6-1 displays the unaltered hyperbolic dataset alongside the outcomes post-deletion at the fifth and tenth levels for both methodologies.

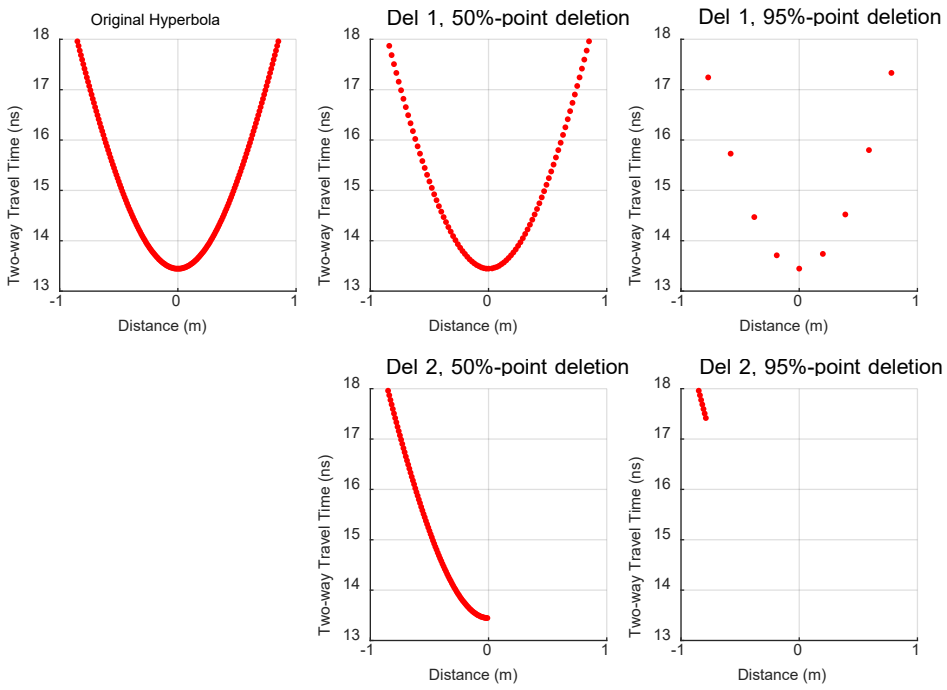

Figure 6-1. Original hyperbolic dataset with the datasets post-fifth and tenth deletion iterations utilizing two distinct methodologies for hyperbolic integrity disruption. "Del 1" and "Del 2" denote the first and second methods respectively, while "5th batch" and "10th batch" refer to the deletion of 50% and 95% of the original hyperbolic points, correspondingly.

6.4.1. Effects of Hyperbolic Fitting Models and Deletion Methods

To study the impact of varying hyperbolic integrity on parameter estimation, we employed optimization techniques to determine the empirical distributions of burial depth and wave velocity. The resulting distributions, depicted in Figure 6-2 and Figure 6-3, were analyzed for two hyperbolic fitting models across different integrity scenarios, specifically focusing on raw data and the effects after 50% (5th) and 95% (10th) point deletions.

The distribution analysis revealed that, under both models, parameter distributions typically conform to a normal distribution. Notably, the effect of point deletion on these distributions varied significantly with the deletion method used. For Model 1 (Figure 6-2), uniformly removing points across the hyperbolic reflection did not significantly alter the distribution of parameters. However, when adopting the biased point deletion, the distributions remained stable until 50% points were deleted. Beyond this, significant

shifts in both the mean and standard deviation were observed, suggesting a marked increase in the integrity impact.

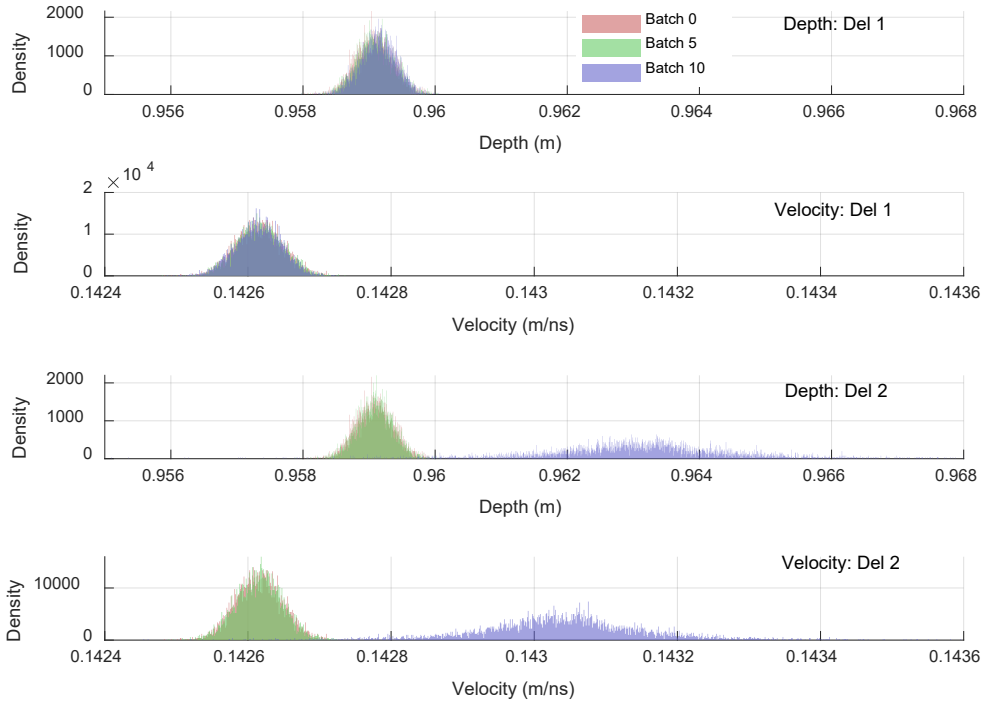

Figure 6-2. Empirical distributions of burial depth and wave velocity using Model 1.

In contrast to Model 1, the application of the initial deletion method exerts a marginal impact on parameter distribution within the framework of Model 5. The biased point deletion yields similar findings for both models, indicating that the removal of 50% of hyperbolic points does not substantially influence parameter distributions. Nevertheless, deleting 95% of the points obviously influences the parameters.

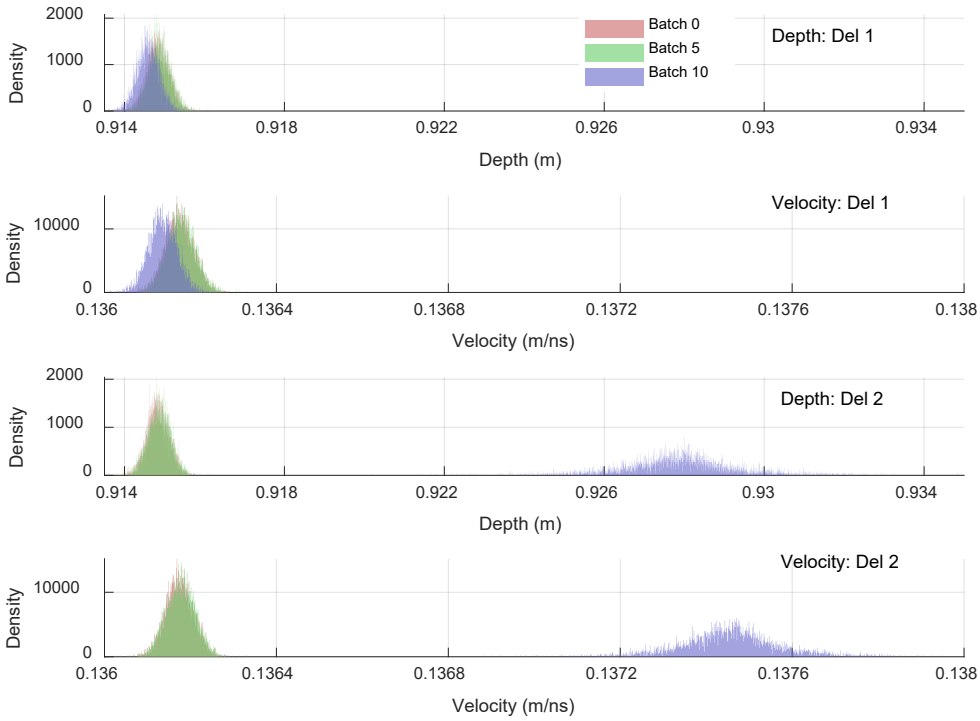

Figure 6-3. Empirical distributions of burial depth and wave velocity using Model 5.

Upon analyzing the parameter distributions across various deletion batches, statistical measures such as the mean, standard deviation, and R-squared offer insights into the impact associated with hyperbolic integrity.

Figure 6-4 and Figure 6-5 reinforce these observations, showing that the systematic removal of points does not substantially affect the mean values or model fit, as indicated by R-squared values, until a critical threshold of point deletion, indicated by arrows, is reached. Remarkably, removing up to 95% of the points results in minimal fluctuation in parameter estimates, leaving a sparse set of data points yet yielding stable estimates. This robustness highlights the hyperbolic fitting methods' resilience to data reduction but also points to significant impact when hyperbolic integrity is heavily compromised by biased point removal.

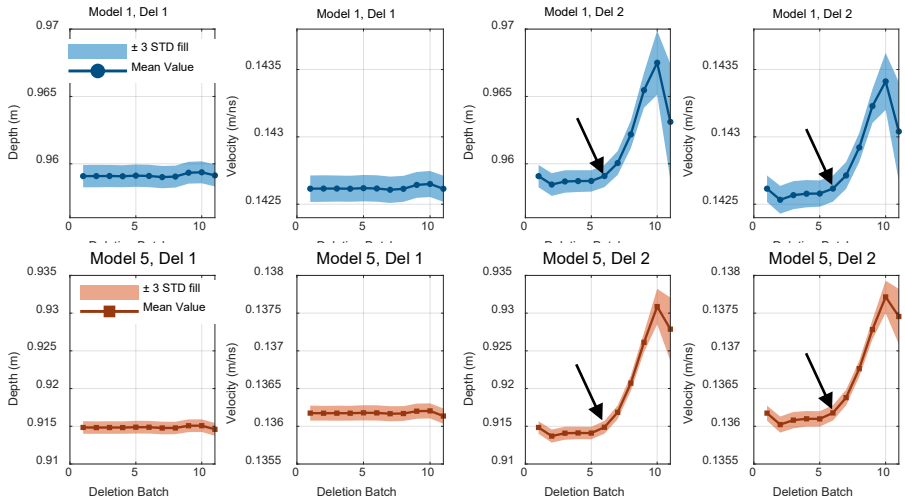

Figure 6-4. Variation in mean depth and wave velocity, including thrice the standard deviation, across different deletion batches.

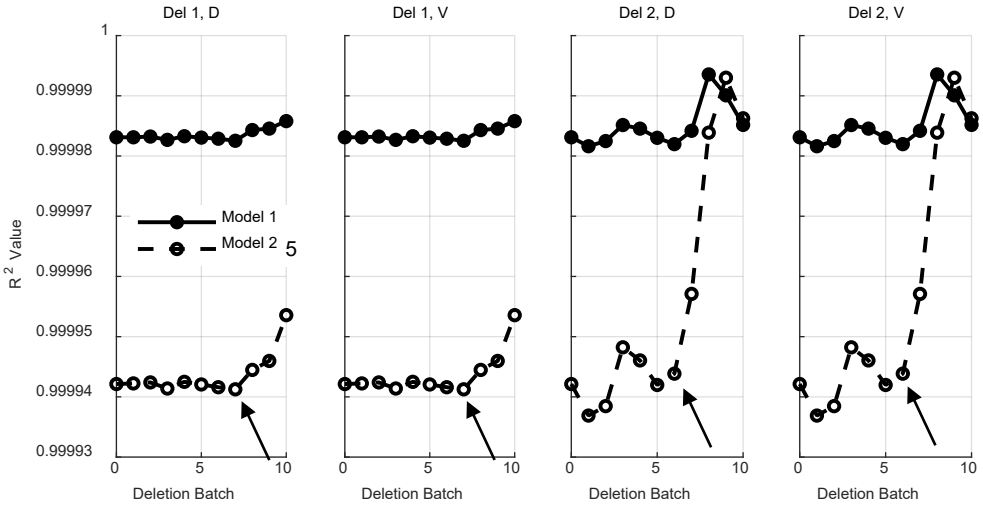

Figure 6-5. R-squared values derived from parameter estimations at varying levels of data deletion.

6.4.2. Effects of Burial Depth, Relative Permittivity, and Target Radius

Following an initial demonstration of the process for assessing hyperbolic integrity impact through the use of R-squared and mean value analysis, our investigation extends to the effects of burial depth, relative permittivity, and pipe radius on this impact. To conduct a comprehensive analysis, three sets of simulation models were generated, each varying one of these three critical parameters. The specific configurations of these models are displayed in Table 6-1, which outlines the range and increments of each variable under consideration.

Table 6-1. Three sets of simulation models with varying burial depth, relative permittivity, and pipe radius.

Parameters	Simulation Set 1		
	1	2	3
Depth (m)	0.3	0.9	1.5
Permittivity		5	
Radius (m)		0.1	
	Simulation Set 2		
Depth (m)		0.9	
Permittivity	3	5	9
Radius (m)		0.1	
	Simulation Set 3		
Depth (m)		0.9	
Permittivity		5	
Radius (m)	0.02	0.1	0.3

The impact of subsurface variations on the integrity of hyperbolic reflections has been examined through a systematic computation of parameter differentials. This computation was performed by incrementally reducing the number of points constituting the hyperbolic curve, while their referenced variations in burial depth, relative permittivity, and target radius were accounted for.

These differential metrics serve as robust indicators of the sensitivity of the estimations to modifications in the modeled subsurface conditions. For instance, when points are systematically deleted from the hyperbolic reflection to represent varying degrees of hyperbolic integrity, the resulting changes in parameter estimations can be precisely quantified. The mathematical expressions employed in this analysis are delineated as follows:

$$\Delta_{D_i^j} = D_i^{j+1} - D_i^j - \Delta_{\hat{D}^j} \tag{6.6}$$

$$\Delta_{v_i^j} = v_i^{j+1} - v_i^j - \Delta_{\hat{v}^j} \tag{6.7}$$

$$v_i^j = \frac{c_0}{\sqrt{\varepsilon^j}} \tag{6.8}$$

where D_i^j represents the mean depth of the j^{th} model at i^{th} deletion batch, v_i^j represents the mean wave velocity of the j^{th} model at i^{th} deletion batch, $\Delta_{\hat{D}^j}$ is the reference variation in depth between j^{th} and $(j+1)^{th}$ models, $\Delta_{\hat{v}^j}$ is the reference variation in wave velocity between j^{th} and $(j+1)^{th}$ models, c_0 is the wave velocity of the light in the vacuum, and ε^j is the permittivity of the j^{th} model.

Equation (6.6) captures the change in the estimated mean depth between two consecutive models after accounting for the input depth variation, while Equation (6.7) represents the analogous change in estimated mean wave velocity. Equation (6.8) provides the relationship between the wave velocity in the medium (v_i^j) and its relative permittivity (ε^j). These equations form the foundation of the proposed approach to systematically assess how burial depth, relative permittivity, and object radius influence hyperbolic integrity impact. The following sections present the outcomes of this analysis, highlighting the interdependencies and isolated impacts of each parameter on the fidelity of hyperbolic data interpretation.

Sensitivity to Depth Variation: Illustrated in Figure 6-6, we note that depth variations exert differential impacts on hyperbolic integrity impact based on the deletion method applied. Uniform point deletion maintains stability across a wide range of depths, indicating the robustness of hyperbolic fitting methods to depth changes. This robustness diminishes when points are removed unilaterally, with sensitivity to depth variations becoming obvious beyond the removal of 50% of points. Such sensitivity reduces with increasing depth, implying a depth-dependent influence on hyperbolic integrity impact.

Sensitivity to Relative Permittivity Variation: As depicted in Figure 6-7, changes in relative permittivity influence wave velocity estimates but have a negligible effect on

depth estimates across both deletion methods. This finding underscores the inherent model errors in hyperbolic fitting algorithms, affected by permittivity variations, yet reveals the algorithms' resilience to such changes in estimating burial depth.

Sensitivity to Radius Variation: Demonstrated in Figure 6-8, the sensitivity analysis reveals that adjustments in object radius have minimal impact on Model 5's estimates, showing the model's accuracy despite radius variations. Conversely, Model 1 exhibits sensitivity to radius changes, particularly under biased point deletion, highlighting a greater sensitivity to alterations in target radius, especially when points are removed beyond a 50% threshold.

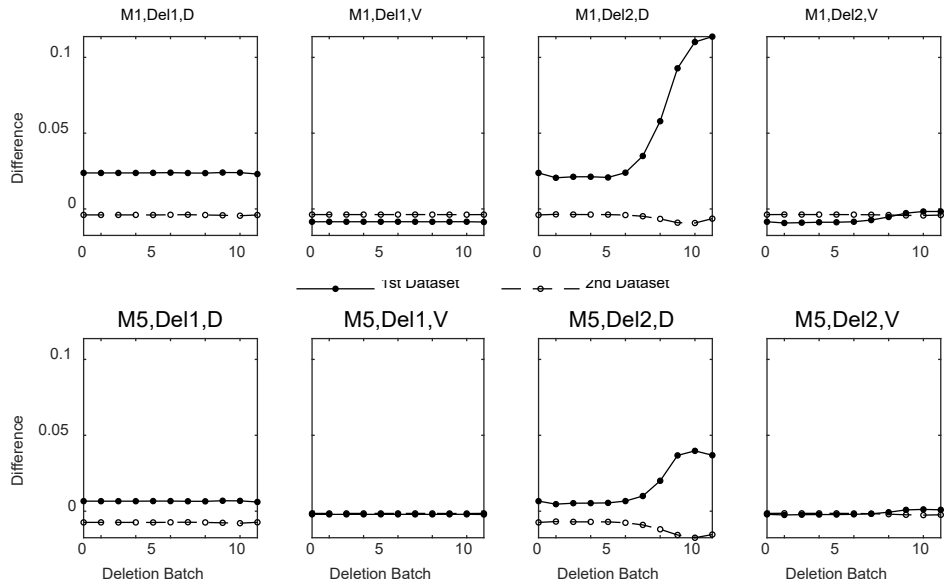

Figure 6-6. Differential impact on parameter estimates due to variations in burial depth with altered hyperbolic integrity. '1st Dataset' (solid lines): Illustrates the changes in estimated parameters when the burial depth is modified from 0.3m to 0.9m across varying levels of hyperbolic integrity disruption. '2nd Dataset' (dashed lines): Showcases the changes in estimated parameters with a further increase in burial depth from 0.9m to 1.5m, also across varying levels of hyperbolic integrity disruption.

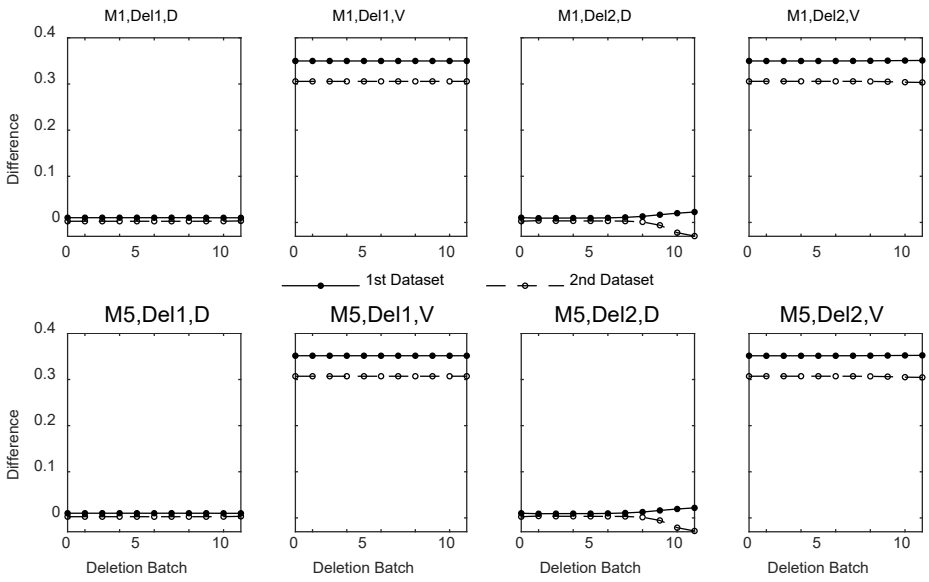

Figure 6-7. Differential impact on parameter estimates due to variations in relative permittivity with altered hyperbolic integrity. '1st Dataset' (solid) reflects adjustments from permittivity of 3 to 5, and '2nd Dataset' (dashed) from 5 to 9.

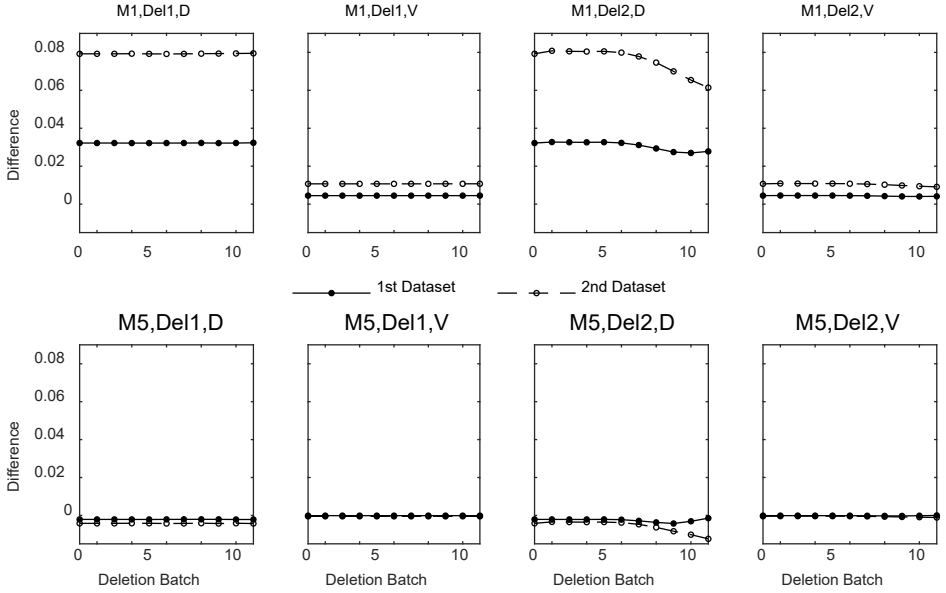

Figure 6-8. Differential impact on parameter estimates due to variations in object radius with altered hyperbolic integrity. '1st Dataset' (solid) reflects radius adjustments from 0.02m to 0.1m, and '2nd Dataset' (dashed) from 0.1m to 0.3m.

It is vital to acknowledge that the numerical simulations have not accounted for numerous variables that influence GPR detection in practical scenarios. For instance, an increase in depth typically deteriorates scattering losses and introduces additional

noise, whereas a higher dielectric permittivity may reflect increased moisture content or alterations in material composition. Such elements can impact the quality of GPR signals, consequently affecting the outcomes derived from the simulation experiments discussed herein. Bearing this in mind, the following section will adopt the same analytical approach to investigate hyperbolic curves acquired from field data.

6.5. Field Experiment

This section delves into field experiments conducted within a geophysical environment to assess the hyperbolic integrity impact. The fieldwork was executed at a dedicated research facility managed by IFSTTAR in France (Derobert and Pajewski, 2018; Dérobert and Pajewski, 2018). This facility featured three trenches, each filled with a unique mixture of silt, sand, and gravel. Within these trenches, a total of nine pipes were methodically buried at three different depths, creating layers that each contained an air-filled PVC pipe, a water-filled PVC pipe, and a metal pipe, all positioned parallel to one another. Details can be found in the research of Dérobert and Pajewski (Dérobert and Pajewski, 2018).

Same as chapter 3, the focus of the study was on metal pipes, due to the weaker reflections from PVC materials. Radius of the metal pipes are typically 0.04 m. They were buried at depths of 1.184 m and 2.395 m in the sand-layered trench. These metal pipes were selected for their pronounced curved reflections, which were essential for our analysis. The data was collected using a GSSI 4000 control unit paired with GSSI antennas with a central frequency of 270 MHz. The data collection was characterized by a step interval of 0.005 m, a time window of 100 ns, and a total of 1024 points per scan. Figure 6-9 presents the extracted hyperbolic reflection from the pipe buried at a depth of 2.395 m alongside reflections of varying integrity, obtained through the implementation of different point deletion methods.

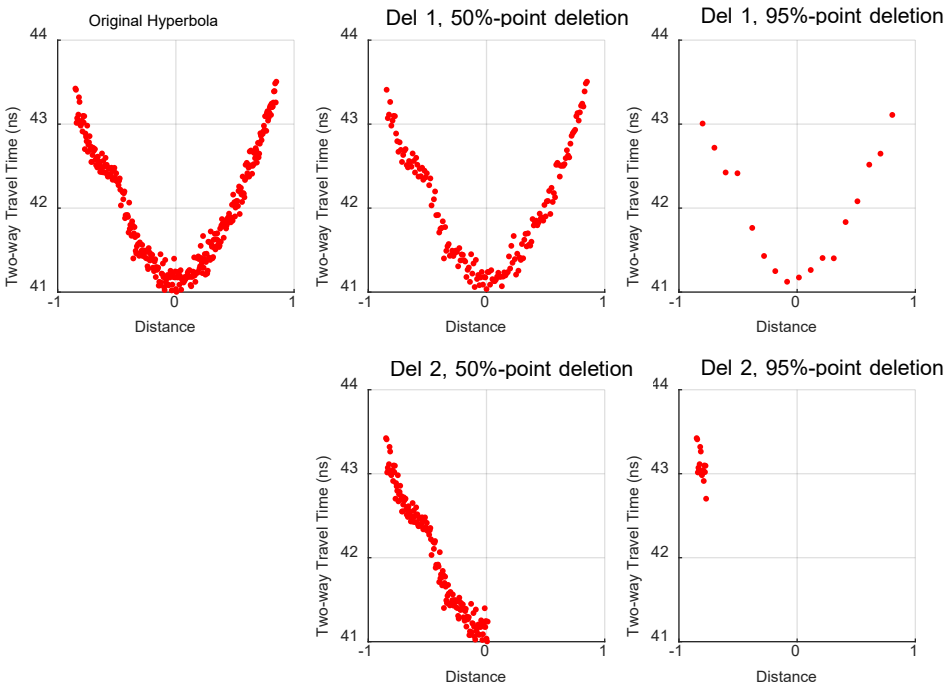

Figure 6-9. Original hyperbolic data for the metal pipe buried at 2.395 m, alongside datasets after the fifth and tenth deletion iterations, demonstrating two methods of hyperbolic integrity disruption.

Empirical distributions of depth and wave velocity estimates from the metal pipe at a depth of 2.395 m in the sand trench were analyzed using both Model 1 and Model 5, depicted in Figure 6-10 and Figure 6-11, respectively. Echoing the patterns observed in the simulation experiments, the parameter distributions conformed to normal distributions. A notable deviation from the simulation outcomes is the observable influence of the uniform point deletion method on parameter distributions in the field data. While parameter distributions largely overlap when up to 50% of points are removed, the distributions undergo a complete transformation with the deletion of 95% of the points. The biased point deletion's impact on parameter distribution is markedly more pronounced, with both the mean and standard deviation exhibiting significant shifts as the deletion percentage increases. Model 5's results mirror those of Model 1, underscoring a consistent pattern across both models.

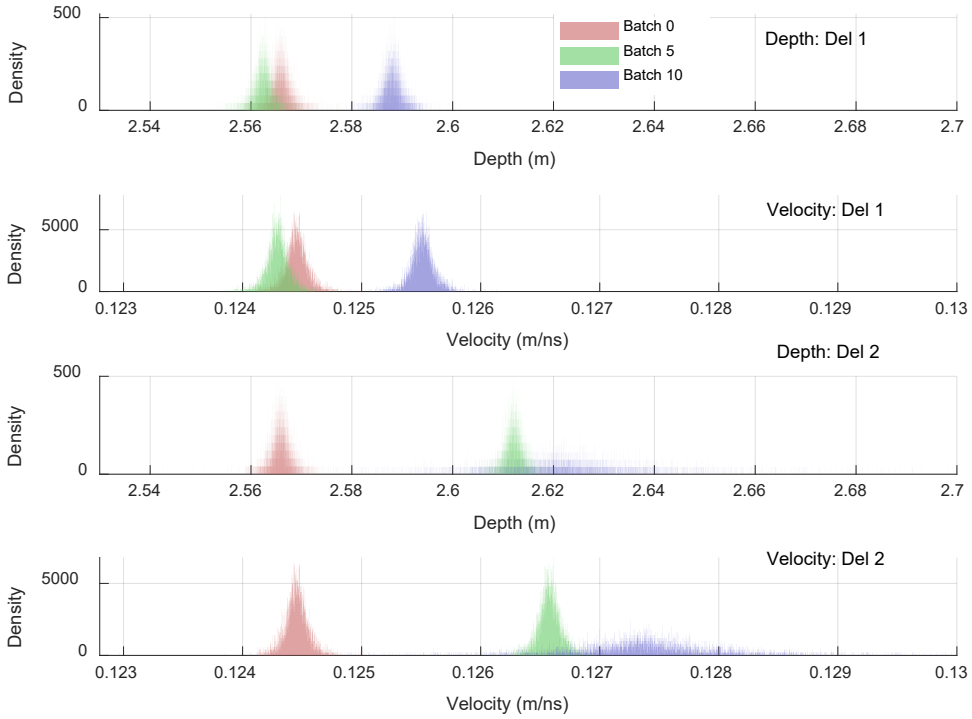

Figure 6-10. Field-derived empirical distributions of burial depth and wave velocity using Model 1.

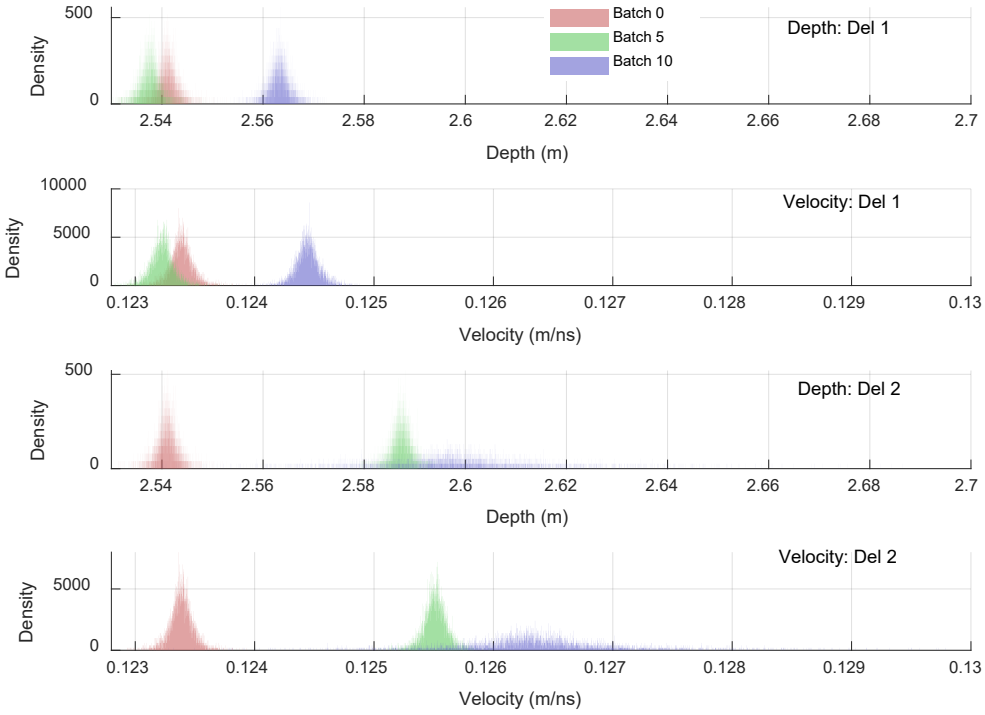

Figure 6-11. Field-derived empirical distributions of burial depth and wave velocity using Model 5.

To quantitatively analyze the impact of hyperbolic integrity in field experiments, the mean (Equation (4.1)), standard deviation (Equation (4.2)), and R-squared (Equation

(4.3)) were computed for hyperbolic reflections with varying integrity, as done in the simulation studies. Figure 6-12 illustrates the mean values and their corresponding standard deviations, multiplied by a factor of three.

The analysis reveals patterns similar to those in the simulation experiments; the integrity of the hyperbolic reflection compromised by the uniform point deletion does not significantly impact the parameter estimation, yielding relatively stable curves with minor fluctuations appearing only beyond the 80% deletion threshold. In contrast, the biased point deletion introduces significant variability in the results upon deletion of more than 40% of the points, with standard deviations increasing alongside the deletion percentage. This differs from the simulation experiments where notable mean value fluctuations manifested only after a 50% deletion, suggesting that the simulation's neglecting of scattering noise could influence the hyperbolic integrity impact. Additionally, comparing the mean value trends across both deletion methods, biased deletion of hyperbolic points introduces a substantially higher level of impact compared to uniform point deletion. It is noteworthy that the bands representing three standard deviations from the mean are virtually imperceptible except at the 95% deletion level using the biased point deletion, indicating a narrow parameter distribution focused around the mean and thus more reliable parameter estimations from hyperbolic fitting via the optimization method employed.

The R-squared values, depicted in Figure 6-13, corroborate these findings. The values remain consistently high, above 0.9, when points are deleted uniformly. For biased point deletion, a marked decrease in R-squared values is observed after deleting more than 40% of the points, signaling a substantial divergence between the fitted hyperbolic reflection and the actual data. Notably, the R-squared outcomes for Models 1 and 5 converge closely at deeper depths, suggesting that the influence of the pipe's radius and the antenna separation on hyperbolic fitting accuracy is minimal at this level.

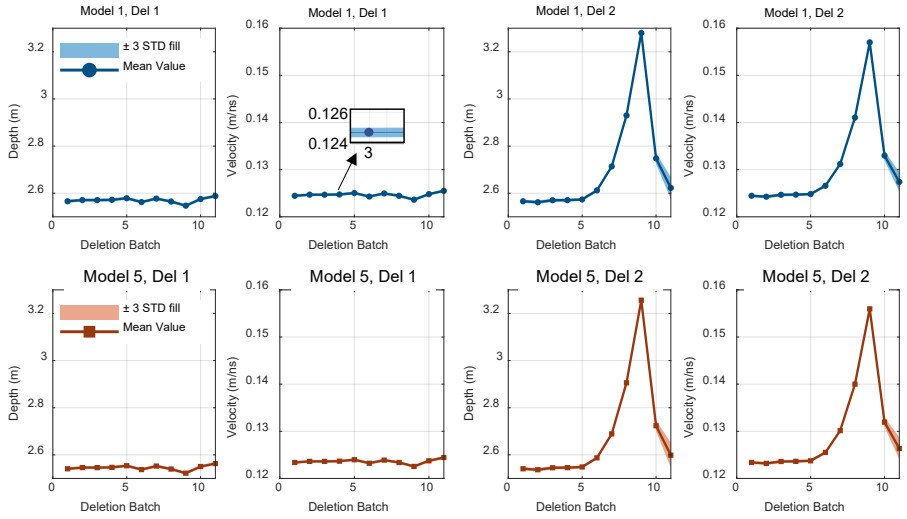

Figure 6-12. Mean values and thrice the standard deviation of hyperbolic reflections across various deletion batches from field experiment 1.

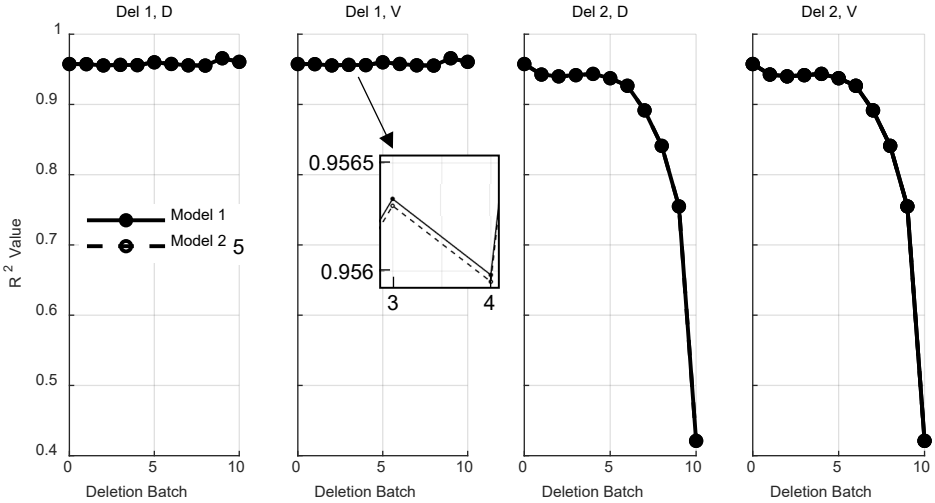

Figure 6-13. R-squared values for parameter estimates across different deletion batches from field experiment 1.

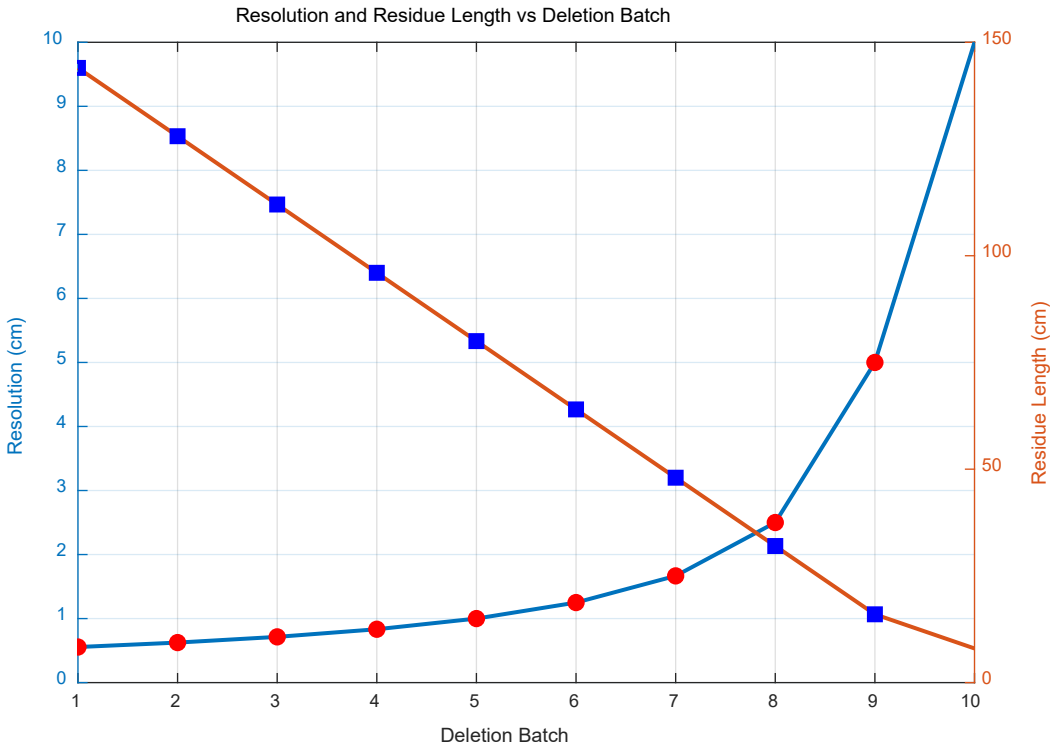

Figure 6-14. Resolution and Residue Length versus Deletion Batch. The resolution, measured in centimeters, represents the spacing between A-scans at different deletion batch and is shown by the bule line and red point. The red line and blue points depict the residue length, also in centimeters, of the remaining hyperbolic sections at different deletion batch.

Figure 6-14 graphically represents the effects of deletion operations on hyperbolic data integrity using two methods: the spacing between A-scans, which is indicative of horizontal resolution, and the residual length of the hyperbolic reflections. As depicted, the uniform point deletion operation results in an increase in the A-scan spacing, progressively expanding from 0.5 cm to 10 cm, which reflects a reduction in resolution with each batch. Simultaneously, the residual length of the hyperbolic reflections, related to the biased deletion method, demonstrates a notable decrease from 144 cm to 8 cm.

The second set of hyperbolic reflections was captured from a metal pipe buried at a depth of 1.184 meters in the sand trench. The empirical distributions of the parameters obtained using Models 1 and 5 across different deletion batches are presented in Figure 6-15 and Figure 6-16, respectively.

Comparing the first and second field data results, the parameter distributions show that the depth of burial does not significantly influence the impact resulting from the disruption of hyperbolic integrity via the uniform point deletion. The distributions of the intact data, the data with 50% point deletion, and the data with 95% point deletion remain relatively congruent, echoing the findings from the initial field experiment. However, with the biased point deletion, the variations in the parameter distributions become more pronounced as the deletion percentage increases, more so than in the first field experiment's results. This suggests that the depth of burial does impact the impact associated with the biased point deletion, a conclusion that aligns with the outcomes of the simulation experiments.

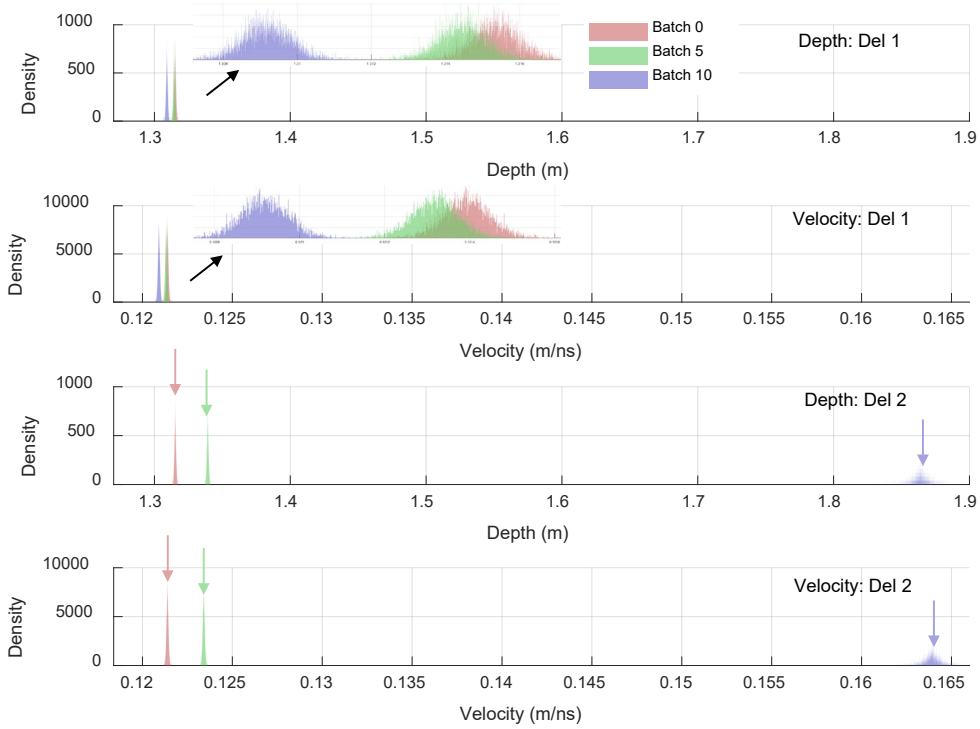

Figure 6-15. Empirical distributions of burial depth and wave velocity as estimated using Model 1 in field experiment 2.

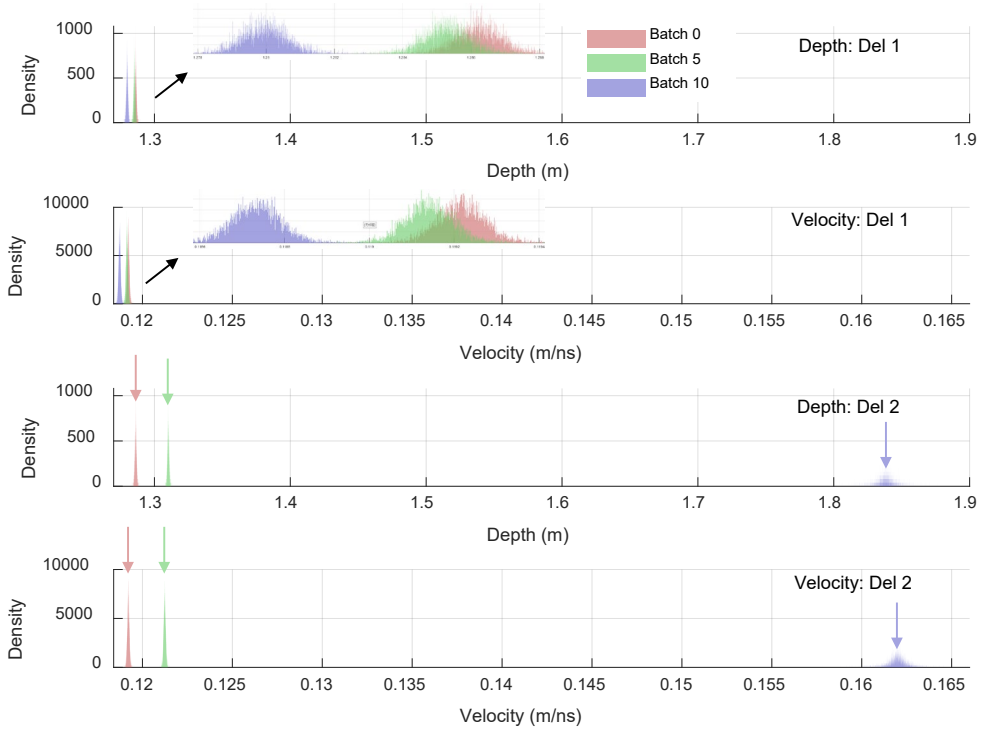

Figure 6-16. Empirical distributions of burial depth and wave velocity as estimated using Model 5 in field experiment 2.

The analysis of the mean values (as depicted in Figure 6-17) and R-square trends (shown in Figure 6-18) yield observations consistent with those from the first field experiment. The impact of the disrupting hyperbolic integrity through the biased point deletion are markedly more significant than those arising from the uniform point deletion. The hyperbolic reflections impacted by the biased point deletion display substantial instability and uncertainty, particularly when the deletion exceeds 40% of the points. At this level of disruption, the hyperbolic reflections become less reliable for the fitting algorithm, leading to unstable results. Notably, at this depth, there is no discernible performance difference between Models 1 and 5, suggesting that the depth of burial does not significantly differentiate their effectiveness.

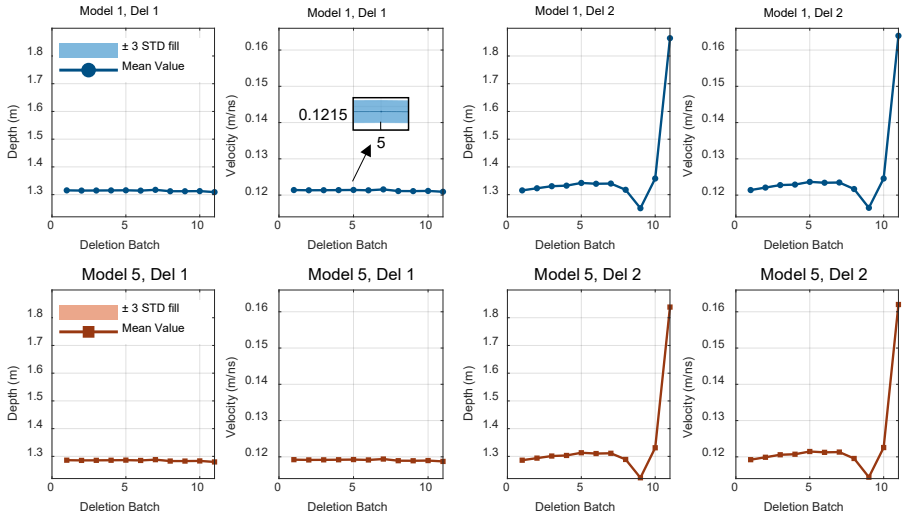

Figure 6-17. The mean value and corresponding 3 times standard deviation of the hyperbolic reflections at different deletion batches obtained from field experiment 2.

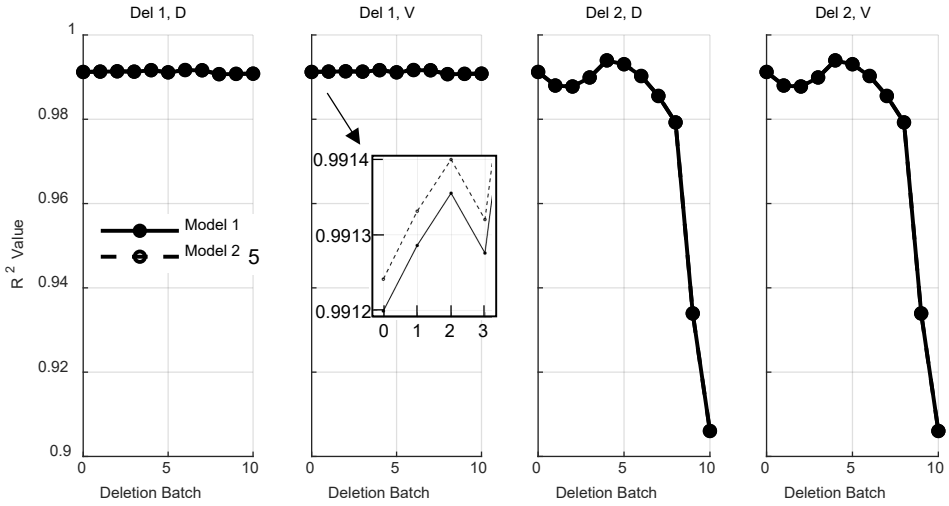

Figure 6-18. R-squared of the parameters estimated at different deletion batches obtained from field experiment 2.

6.6. Discussion

This chapter has undertaken a comprehensive analysis of the hyperbolic integrity impact within the context of GPR hyperbolic fitting. By conceptualizing the fitting as an optimization problem, we have employed two models to study the effects of alterations in hyperbolic integrity through uniform and biased point deletions. This methodology has enabled us to quantify the impact affecting parameter estimations of

burial depth and wave velocity, providing significant insights into the robustness of fitting techniques against data incompleteness.

The investigation of uniform point deletion reveals a remarkable resilience of fitting processes. Even with the deletion of up to 95% of data points, with a A-scan interval of 10 cm that can be seen in Figure 6-14, hyperbolic fitting's ability to accurately estimate subsurface parameters remains largely unaffected. This finding is particularly relevant in practical scenarios involving GPR array antennas measurement (Jia et al., 2022), where the arrangement of sparse antenna pairs can still yield sufficiently reliable hyperbolic data for fitting. This underscores the potential for direct deletion of aberrant data points in measurements and enhances the flexibility of GPR investigations in urban infrastructure assessments and archaeological site explorations.

Conversely, the analysis of biased point deletion highlights a threshold of hyperbolic integrity, below which the fitting algorithm's reliability diminishes. Specifically, when over 60% of the integrity is preserved, 64 cm of hyperbolic reflection that can be seen in Figure 6-14, parameter estimations remain dependable. This outcome is critical for urban underground pipeline detection (Lai et al., 2016a; Xie et al., 2018), where hyperbolic reflection often appears incomplete due to obstructive subsurface elements. Similarly, in planetary exploration (Zhang et al., 2020), the integrity of hyperbolic reflections may be compromised by scattering or nearby targets. The findings provide a quantitative basis for assessing the reliability of hyperbolic fitting under such conditions, thereby facilitating more accurate subsurface characterizations.

However, this study acknowledges several limitations. The exploration of hyperbolic integrity disruptions has been confined to two specific models, while real-world GPR measurements often encounter a broader spectrum of hyperbolic data incompleteness. Furthermore, although this study offers a methodological framework for estimating the impact of the hyperbolic integrity on the hyperbolic fitting, the variability and complexity of actual GPR environments necessitate further empirical validation.

6.7. Summary and Contribution

This chapter has examined the impact of hyperbolic integrity on the accuracy of parameter estimation using hyperbolic fitting methods in GPR applications. By framing hyperbolic fitting as an optimization problem, the research facilitated the derivation of empirical distributions for key parameters and allowed for a detailed assessment of the impact of the hyperbolic integrity. The major contributions and findings from this investigation are summarized as follows:

1. The study confirmed that the uniform point deletion of points on hyperbolic reflections has minimal impact on parameter estimation. This robustness was consistent across various subsurface conditions, including changes in burial depth, dielectric permittivity, and target radius.

2. Contrary to uniform point deletion, biased/one-side biased point deletion significantly decreased estimation stability, especially when over 40% of data points were removed. This scenario highlighted critical vulnerabilities in the hyperbolic fitting process, particularly when dealing with sparse data in complex subsurface environments.

3. The analysis contrasted two hyperbolic fitting models, revealing that changes in burial depth and target radius variably influenced their performance. Model 1 showed greater sensitivity to these parameters at shallow depths, whereas Model 5 maintained consistent accuracy, acknowledging the importance of model selection based on specific site conditions.

4. Alterations in dielectric permittivity were found to indirectly affect the outcomes of hyperbolic fitting, suggesting potential model errors that need to be addressed to enhance the accuracy of GPR investigations.

7. Chapter 7: Conclusion

The research systematically explored various hyperbolic fitting models and their optimizations to enhance subsurface utility detection accuracy. Through extensive research, key limitations in traditional hyperbolic fitting methods were identified, primarily their dependency on the assumption of homogeneous media, and addressed through the development of novel fitting and correction algorithms. Each chapter systematically tackled different aspects of the GPR data analysis, from basic hyperbolic fitting to complex adjustments for media heterogeneity and target orientation. The comprehensive analysis encompassed both numerical simulations and field experiments, enriching the understanding of GPR applications in diverse environments. Notably, the proposed methodologies demonstrate enhanced precision in depth and wave velocity estimations across diverse subsurface conditions, significantly improving the reliability of initial parameter inputs for full-waveform inversion (FWI) frameworks. This thesis strengthens the theoretical foundations of GPR analysis and provides practical guidelines and innovative tools for more accurate subsurface explorations, marking a significant advancement in geophysical survey techniques.

7.1. Main Finding

- Comparative Analysis of Hyperbolic Fitting Models for Subsurface Parameter Estimation (Chapter 3)

A rigorous evaluation of various hyperbolic fitting models used in GPR has shown how different configurations respond under varying conditions influenced by target radius, antenna separation, and material relative permittivity. Insights include the sensitivity of models to target characteristics, where accuracy varied significantly based on the target's radius relative to its depth. Despite theoretical advantages, increased depth often led to performance degradation due to signal attenuation. Variations in antenna separation had minimal impact on model performance within certain limits, but practical changes significantly affected signal strength and resolution. The analysis concludes with strategic recommendations for selecting appropriate hyperbolic fitting

models, emphasizing the need for tailored approaches based on specific application scenarios, operational constraints, and available data.

- Enhancing Parameter Estimation Accuracy through Angle-Corrected Hyperbolic Fitting Models (Chapter 4)

Incorporating target orientation in hyperbolic fitting has proven critical for improving the accuracy of parameter estimations from hyperbolic reflections of cylindrical objects. A unique cost function combining synthetic and real TTT data has been developed, enabling the C-value analysis which assesses the impact of pipeline orientation on fitting precision and introduces a robust metric for evaluating and optimizing hyperbolic fitting methods. Furthermore, a hybrid optimization strategy effectively estimates pipeline orientation, depth, and wave velocity, enhancing GPR data analysis applicability and accuracy. This method is applied through models requiring varying levels of prior information, validated by extensive simulation and field experiments. Additionally, this research extends to quantitatively examine the effects of varying pipeline radii and burial depths at different angles, thereby enriching the understanding of factors impacting parameter estimation accuracy and augmenting the robustness of fitting techniques. These methodologies advance GPR-based parameter estimation, providing a detailed framework for precise subsurface investigations and paving the way for further research in practical GPR applications.

- Depth-Weighted Velocity Correction (chapter 5)

Addressing the traditional limitations of single velocity inherent in hyperbolic fitting methods in layered materials with different dielectric properties, this chapter introduces a depth-weighted velocity correction algorithm designed to refine parameter estimation in multi-layered subsurface conditions. The research critically evaluates the errors in velocity estimation when hyperbolic fitting is applied directly to layered media, offering insights into the challenges of non-homogeneous environments. This novel algorithm significantly reduces velocity estimation errors and improves the accuracy of such estimates within target-contained layers, proving adaptable to various hyperbolic

fitting models based on available target radius and antenna separation. Furthermore, a comparative analysis of two fitting models incorporating this correction algorithm provides essential guidelines for model selection, tailored to the specific characteristics of layered subsurface scenarios. These guidelines assist practitioners in selecting the most suitable ray-path model in layered materials and, enhancing the precision of subsurface investigations and paving the way for more accurate and reliable GPR applications in complex geological settings.

- Impact of Data Integrity on Hyperbolic Fitting (chapter 6)

This chapter addresses the influence of hyperbolic data integrity on the accuracy of parameter estimations within GPR applications. The chapter unveils that uniform point deletion of points on hyperbolic reflections minimally impacts the estimation, demonstrating method robustness under varying subsurface conditions such as changes in burial depth, dielectric permittivity, and target radius. In contrast, biased point deletion markedly decreases the estimation stability, particularly with over 40% of data removed, exposing significant vulnerabilities in scenarios with sparse data. Comparative analysis of two fitting models illustrates differing sensitivities to subsurface characteristics, with one model showing heightened responsiveness at shallower depths while the other maintains consistent accuracy across varied conditions. Additionally, the research identifies that changes in dielectric permittivity indirectly influence fitting outcomes, pointing to potential model errors that need consideration for improving GPR data interpretation accuracy.

7.2. Challenges and Future Work

- Refining Model Selection in GPR Hyperbolic Fitting

The importance of selecting hyperbolic fitting models appropriate for specific GPR applications is highlighted, though challenges persist due to small sample sizes and the exclusion of noise effects. Future research should include larger datasets, consider the impact of noise, and explore global optimization algorithms. Investigating how antenna frequency and separation affect model performance is essential to enhance the accuracy

and applicability of GPR hyperbolic fitting techniques across different geological settings.

- Enhancing Accuracy in Hyperbolic Fitting for Pipe Orientation

The introduced methodologies for estimating pipe orientation demonstrate potential but face accuracy challenges at smaller oblique angles and with non-horizontal orientations. Future efforts should focus on improving accuracy for smaller angles and expanding analyses to include inclined and vertical orientations. Additionally, developing optimization algorithms that target global optima and are less susceptible to local minima will be crucial. Extending model validation to lower quality or incomplete hyperbolic data will ensure broader applicability.

- Improving Velocity Estimations in Layered Media Using Depth-Weighted Corrections

The proposed depth-weighted velocity correction algorithm improves velocity estimation but simplifies wave interactions at layer interfaces, potentially introducing errors in environments with significant dielectric contrasts. Future research should refine these assumptions and expand the algorithm's utility to more complex, multi-layered conditions, ensuring the algorithm accounting for the longer or shorter ray-path due to wave refraction and reflection governed by Snell's Law to enhance accuracy of velocity and object depth's measurements in stratified settings.

- Quantifying Impact in Hyperbolic Fitting with Data Integrity Disruptions

This research addresses the impact of hyperbolic integrity on fitting accuracy due to variation of B-scan's spatial resolution, acknowledging the limitation of focusing on only two models. The proposed methodologies require further empirical validation to handle the variability of real-world GPR measurements. Future studies should explore a wider range of data integrity scenarios and empirically test the methodologies to enhance the reliability and accuracy of subsurface investigations.

In conclusion, this PhD research has advanced the methodologies for estimating subsurface parameters through refined hyperbolic fitting techniques using GPR. The thesis addressed traditional limitations of hyperbolic fitting, integrating advanced optimization algorithms and innovative approaches like angle-corrected and depth-weighted velocity corrections. These enhancements have broadened the applicability of hyperbolic fitting to complex underground scenarios including layered subsurface structures and varying orientations of buried objects. Furthermore, the research developed methodologies to quantitatively assess the impact of the hyperbolic integrity on hyperbolic fitting in GPR data analysis. By empirically and numerically validating these methods, the research bridged theoretical models with practical applications, improving the reliability of subsurface evaluations.

Previous studies have utilized GPR to detect the presence or absence of subsurface anomalies, such as underground utilities, reinforcing bars, and historical substructures. Advancements in GPR technology have gradually transformed it from a mere detection tool into a precise measurement instrument. This study further advances GPR's application, enhancing its precision in providing accurate measurements across various environmental conditions. These improvements contribute to archaeological explorations and civil engineering, where accurate and reliable mapping of both known and unknown subsurface objects is essential.

Reference

Abdelmawla, A., Kim, S.S., 2020. Application of ground penetrating radar to estimate subgrade soil density. Infrastructures 5.

Abueladas, A.E.R., Akawwi, E., 2020. Ground-penetrating radar inspection of subsurface historical structures at the baptism (El-Maghtas) site, Jordan. Geoscientific Instrumentation, Methods and Data Systems 9, 491-497.

Agred, K., Klysz, G., Balayssac, J.P., 2018. Location of reinforcement and moisture assessment in reinforced concrete with a double receiver GPR antenna. Construction and Building Materials 188, 1119-1127.

Al-Nuaimy, W., Huang, Y., Nakhkash, M., Fang, M.T.C., Nguyen, V.T., Eriksen, A., 2000. Automatic detection of buried utilities and solid objects with GPR using neural networks and pattern recognition. Journal of Applied Geophysics 43, 157-165.

Amer-Yahia, C., Majidzadeh, T., 2012. Inspection of insulated concrete form walls with ground penetrating radar. Construction and Building Materials 26, 448-458.

Anderson, N.L., Torgashov, E., Kovin, O., 2010. Ground penetrating radar: Utility/rebar/cable detection and concrete/subgrade debonding, Symposium on the Application of Geophysics to Engineering and Environmental Problems 2010. Society of Exploration Geophysicists, pp. 9-21.

Annan, A.P., 2004. Ground penetrating radar applications, principles, procedures. Mississauga, Canada: Sensors and Software.

Arosio, D., Munda, S., Zanzi, L., Longoni, L., Papini, M., 2012. GPR investigations to assess the state of damage of a concrete water tunnel. Journal of Environmental and Engineering Geophysics 17, 159-169.

Aziz, A.S., Stewart, R.R., Green, S.L., Flores, J.B., 2016. Locating and characterizing burials using 3D ground-penetrating radar (GPR) and terrestrial laser scanning (TLS) at the historic Mueschke Cemetery, Houston, Texas. Journal of Archaeological Science: Reports 8, 392-405.

Berard, B.A., Maillol, J., 2008. Common-and multi-offset ground-penetrating radar study of a Roman villa, Tourega, Portugal. Archaeological Prospection 15, 32-46.

Bourgeois, J.M., Smith, G.S., 1996. A fully three-dimensional simulation of a ground-penetrating radar: fdtd theory compared with Experiment. IEEE Transactions on Geoscience and Remote Sensing 34, 36-44.

Booth, A.D., Pringle, J.K., 2016. Semblance analysis to assess GPR data from a five-year forensic study of simulated clandestine graves. Journal of Applied Geophysics 125, 37-44.

Bourdi, T., Rhazi, J.E., Boone, F., Ballivy, G., 2012. Modelling dielectric-constant values of concrete: An aid to shielding effectiveness prediction and ground-penetrating radar wave technique interpretation. Journal of Physics D: Applied Physics 45.

Cao, Q., Al-Qadi, I.L., Abufares, L., 2022. Pavement moisture content prediction: A deep residual neural network approach for analyzing ground penetrating radar. IEEE Transactions on Geoscience and Remote Sensing 60, 1-11.

Chan, E.Y.Y., Ho, J.Y.-e., 2019. Urban water and health issues in Hong Kong. Urban drought: Emerging water challenges in Asia, 241-262.

Chan, S.N., Chang, L., Choi, K.W., Lee, J.H., Fawell, J.K., Kwok, K.Y., 2020. Unraveling the causes of excess lead in drinking water supply systems of densely populated high-rise buildings in Hong Kong. Environmental Science & Technology 54, 14322-14333.

Chen, Y.D., 2001. Sustainable development and management of water resources for urban water supply in Hong Kong. Water international 26, 119-128.

Church, G., Bauder, A., Grab, M., Rabenstein, L., Singh, S., Maurer, H., 2019. Detecting and characterising an englacial conduit network within a temperate Swiss glacier using active seismic, ground penetrating radar and borehole analysis. Annals of Glaciology 60, 193-205.

Church, G., Grab, M., Schmelzbach, C., Bauder, A., Maurer, H., 2020. Monitoring the seasonal changes of an englacial conduit network using repeated ground-penetrating radar measurements. The Cryosphere 14, 3269-3286.

Conyers, L.B., 2016. Ground-penetrating radar mapping using multiple processing and interpretation methods. Remote Sensing 8, 562.

Cui, F., Li, S., Wang, L., 2018. The accurate estimation of GPR migration velocity and comparison of imaging methods. Journal of Applied Geophysics 159, 573-585.

Cui, X., Zhang, Z., Guo, L., Liu, X., Quan, Z., Cao, X., Chen, X., 2021. The root-soil water relationship is spatially anisotropic in shrub-encroached grassland in north china: Evidence from gpr investigation. Remote Sensing 13.

Daniels, D.J., 2004. Ground penetrating radar. Iet.

Dérobert, X., Berenger, B., 2010. Using ground-penetrating radar (GPR) to assess an eight-span post-tensioned viaduct: a case study, Non-Destructive Evaluation of Reinforced Concrete Structures. Elsevier, pp. 574-584.

Derobert, X., Pajewski, L., 2018. The GPR dataset of the IFSTTAR Geophysical Test Site, EGU General Assembly Conference Abstracts, p. 6548.

Dérobert, X., Pajewski, L., 2018. TU1208 Open Database of Radargrams: The Dataset of the IFSTTAR Geophysical Test Site, Remote Sensing.

Ding, C., Xiao, Z., Su, Y., Cui, J., 2021. Hyperbolic reflectors determined from peak echoes of ground penetrating radar. Icarus 358.

Dou, Q., Wei, L., Magee, D.R., Atkins, P.R., Chapman, D.N., Curioni, G., Goddard, K.F., Hayati, F., Jenks, H., Metje, N., Muggleton, J., Pennock, S.R., Rustighi, E., Swingler, S.G., Rogers, C.D.F., Cohn, A.G., 2016. 3D buried utility location using a marching-cross-section algorithm for multi-sensor data fusion. Sensors (Switzerland) 16.

Ellis, P., 1998. Chaos in the Underground: Spontaneous Collapse in a Tightly-Coupled System. Journal of Contingencies and Crisis Management 6, 137-152.

Forth, R., 2004. Groundwater and geotechnical aspects of deep excavations in Hong Kong. Engineering Geology 72, 253-260.

Foss, M.M., Leckenby, R.J., 1987. Coal mine hazard detection using in-seam ground-penetrating-radar transillumination. US Department of the Interior, Bureau of Mines.

Fan, G.X., Liu, Q.H., 2000. An FDTD algorithm with perfectly matched layers for general dispersive media. IEEE Transactions on Antennas and Propagation 48, 637-646.

Garg, S., Misra, S., 2021. Efficiency of NDT techniques to detect voids in grouted post-tensioned concrete ducts. Nondestructive Testing and Evaluation 36, 366-387.

Gehrig, M.D., Morris, D.V., Bryant, J.T., 2004. Ground penetrating radar for concrete evaluation studies. Technical Presentation Paper for Performance Foundation Association, 197-200.

Getzlaff, M., 2007. Fundamentals of magnetism. Springer Science & Business Media.

Giannakis, I., Giannopoulos, A., Warren, C., 2019. A Machine Learning-Based Fast-Forward Solver for Ground Penetrating Radar with Application to Full-Waveform Inversion. IEEE Transactions on Geoscience and Remote Sensing 57, 4417-4426.

Gürel, L., Oğuz, U., 2000. Three-dimensional FDTD modeling of a ground-penetrating radar. IEEE Transactions on Geoscience and Remote Sensing 38, 1513-1521.

Giannakis, I., Zhou, F., Warren, C., Giannopoulos, A., 2021. Inferring the shallow layered structure at the Chang'E-4 landing site: a novel interpretation approach using lunar penetrating radar. Geophysical Research Letters 48, e2021GL092866.

Giannakis, I., Zhou, F., Warren, C., Giannopoulos, A., 2022. On the Limitations of Hyperbola Fitting for Estimating the Radius of Cylindrical Targets in Nondestructive Testing and Utility Detection. IEEE Geoscience and Remote Sensing Letters 19.

Giannopoulos, A., 1998. The investigation of transmission-line matrix and finite-difference time-domain methods for the forward problem of ground probing radar. University of York.

Giannopoulos, A., 2005. Modelling ground penetrating radar by GprMax. Construction and building materials, 19, pp.755-762.

Guo, H., Lee, S., Louie, P., Ho, K., 2004. Characterization of hydrocarbons, halocarbons and carbonyls in the atmosphere of Hong Kong. Chemosphere 57, 1363-1372.

Gurnett, D., Huff, R., Morgan, D., Persoon, A., Averkamp, T., Kirchner, D., Duru, F., Akalin, F., Kopf, A., Nielsen, E., 2008. An overview of radar soundings of the Martian ionosphere from the Mars Express spacecraft. Advances in Space Research 41, 1335-1346.

He, W., Lai, W.W.-L., 2024. Angle-corrected GPR hyperbolic fitting models for improved parameter estimation. Tunnelling and Underground Space Technology 147, 105741.

He, W., Wai-Lok Lai, W., 2024. Unified optimization-based analysis of GPR hyperbolic fitting models. Tunnelling and Underground Space Technology 146, 105633.

Illawathure, C., Parkin, G., Lambot, S., Galagedara, L., 2020. Evaluating soil moisture estimation from ground-penetrating radar hyperbola fitting with respect to a systematic time-domain reflectometry data collection in a boreal podzolic agricultural field. Hydrological Processes 34, 1428-1445.

Jazayeri, S., Klotzsche, A., Kruse, S., 2018. Improving estimates of buried pipe diameter and infilling material from ground-penetrating radar profiles with full-waveform inversion. Geophysics 83, H27-H41.

Jacob, R.W., Urban, T., 2016. Ground-penetrating radar velocity determination and precision estimates using common-midpoint (CMP) collection with hand-picking, semblance analysis and cross-correlation analysis: A case study and tutorial for archaeologists. Archaeometry 58, 987-1002.

Jafrasteh, B., Fathianpour, N., 2017. Automatic extraction of geometrical characteristics hidden in ground-penetrating radar sectional images using simultaneous perturbation artificial bee colony algorithm. Geophysical Prospecting 65, 324-336.

Janků, M., Cikrle, P., Grošek, J., Anton, O., Stryk, J., 2019. Comparison of infrared thermography, ground-penetrating radar and ultrasonic pulse echo for detecting delaminations in concrete bridges. Construction and Building Materials 225, 1098-1111.

Jaufer, R.M., Ihamouten, A., Goyat, Y., Todkar, S.S., Guilbert, D., Assaf, A., Dérobert, X., 2022. A Preliminary Numerical Study to Compare the Physical Method and Machine Learning Methods Applied to GPR Data for Underground Utility Network Characterization. Remote Sensing 14.

Jaw, S.W., Hashim, M., 2013. Locational accuracy of underground utility mapping using ground penetrating radar. Tunnelling and Underground Space Technology 35, 20-29.

Jia, W., Wang, S., Min, S., Zhang, Y., 2022. Electromagnetic energy focusing technology with GPR array transmitting antenna for high resolution detection. Measurement 203, 112000.

Jiles, D., 2015. Introduction to magnetism and magnetic materials. CRC press.

Jol, H.M., 2008. Ground penetrating radar theory and applications. elsevier.

Kaniewski, Piotr, and Tomasz Kraszewski. 2023. Estimation of Handheld Ground-Penetrating Radar Antenna Position with Pendulum-Model-Based Extended Kalman Filter. Remote Sensing 15, 3: 741.

Kaufmann, M.S., Klotzsche, A., Vereecken, H., van Der Kruk, J., 2020. Simultaneous multichannel multi-offset ground-penetrating radar measurements for soil characterization. Vadose zone journal 19, e20017.

Kennedy, J., Eberhart, R., 1995. Particle swarm optimization, Proceedings of ICNN'95-international conference on neural networks. IEEE, pp. 1942-1948.

Kijima, H., Hattori, T., 2016. Estimation results on the location error when using cable locator. WSEAS Transactions on systems 15, 11-18.

King, R.W.P., Smith, G.S., Owens, M., Wu, T.T., 1981. Antennas in matter: Fundamentals, theory, and applications. NASA STI/Recon Technical Report A 81, 29690.

Kovetz, A., 2000. Electromagnetic theory. Oxford University Press.

Kravitz, B., Mooney, M., Karlovsek, J., Danielson, I., Hedayat, A., 2019. Void detection in two-component annulus grout behind a pre-cast segmental tunnel liner using Ground Penetrating Radar. Tunnelling and Underground Space Technology 83, 381-392.

Lai, W.W.-L., Derobert, X., Annan, P., 2018. A review of Ground Penetrating Radar application in civil engineering: A 30-year journey from Locating and Testing to Imaging and Diagnosis. Ndt & E International 96, 58-78.

Lai, W.W.L., Chang, R.K.W., Sham, J.F.C., Pang, K., 2016a. Perturbation mapping of water leak in buried water pipes via laboratory validation experiments with high-frequency ground penetrating radar (GPR). Tunnelling and Underground Space Technology 52, 157-167.

Lai, W.W.L., Kind, T., Sham, J.F.C., Wiggenhauser, H., 2016b. Correction of GPR wave velocity at different oblique angles between traverses and alignment of line objects in a common offset antenna setting. NDT and E International 82, 36-43.

Landau, L.D., Bell, J.S., Kearsley, M., Pitaevskii, L., Lifshitz, E., Sykes, J., 2013. Electrodynamics of continuous media. elsevier.

Lau, P.K.-W., Cheung, B.W.-Y., Lai, W.W.-L., Sham, J.F.-C., 2021. Characterizing pipe leakage with a combination of GPR wave velocity algorithms. Tunnelling and Underground Space Technology 109, 103740.

Leng, Z., Al-Qadi, I.L., 2014. An innovative method for measuring pavement dielectric constant using the extended CMP method with two air-coupled GPR systems. NDT & E International 66, 90-98.

Lei, W., Hou, F., Xi, J., Tan, Q., Xu, M., Jiang, X., Liu, G., Gu, Q., 2019. Automatic hyperbola detection and fitting in GPR B-scan image. Automation in Construction 106.

Lei, W., Luo, J., Hou, F., Xu, L., Wang, R., Jiang, X., 2020. Underground cylindrical objects detection and diameter identification in GPR B-scans via the CNN-LSTM framework. Electronics (Switzerland) 9, 1-16.

Li, C., Li, M.-J., Zhao, Y.-G., Liu, H., Wan, Z., Xu, J.-C., Xu, X.-P., Chen, Y., Wang, B., 2011. Layer recognition and thickness evaluation of tunnel lining based on ground penetrating radar measurements. Journal of Applied Geophysics 73, 45-48.

Li, S., Cui, X., Guo, L., Zhang, L., Chen, X., Cao, X., 2022. Enhanced Automatic Root Recognition and Localization in GPR Images Through a YOLOv4-Based Deep Learning Approach. IEEE Transactions on Geoscience and Remote Sensing 60.

Liang, Z.-s., Sun, J., Chau, H.K.-m., Echo, I., Leong, M., Wu, D., Chen, G.-h., Jiang, F., 2019a. Experimental and modelling evaluations of sulfide formation in a mega-sized deep tunnel sewer system and implications for sewer management. Environment international 131, 105011.

Liang, Z.-S., Zhang, L., Wu, D., Chen, G.-H., Jiang, F., 2019b. Systematic evaluation of a dynamic sewer process model for prediction of odor formation and mitigation in large-scale pressurized sewers in Hong Kong. Water research 154, 94-103.

Lin, C., Wang, X., Nie, L., Sun, H., Xu, Z., Du, Y., Liu, L., 2020. Comprehensive geophysical investigation and analysis of lining leakage for water-rich rock tunnels: a case study of Kaiyuan Tunnel, Jinan, China. Geotechnical and Geological Engineering 38, 3449-3468.

Liu, H., Huang, X., Han, F., Cui, J., Spencer, B.F., Xie, X., 2019. Hybrid Polarimetric GPR Calibration and Elongated Object Orientation Estimation. IEEE Journal of Selected Topics in Applied Earth Observations and Remote Sensing 12, 2080-2087.

Liu, H., Lin, C., Cui, J., Fan, L., Xie, X., Spencer, B.F., 2020a. Detection and localization of rebar in concrete by deep learning using ground penetrating radar. Automation in construction 118, 103279.

Liu, H., Lu, H., Lin, J., Han, F., Liu, C., Cui, J., Spencer, B.F., 2020b. Penetration properties of ground penetrating radar waves through rebar grids. IEEE Geoscience and Remote Sensing Letters 18, 1199-1203.

Liu, H., Zhong, J., Ding, F., Meng, X., Liu, C., Cui, J., 2022. Detection of early-stage rebar corrosion using a polarimetric ground penetrating radar system. Construction and Building Materials 317, 125768.

Liu, J., Zollinger, D.G., Lytton, R.L., 2008. Detection of delamination in concrete pavements using ground-coupled ground-penetrating radar technique. Transportation research record 2087, 68-77.

Liu, Q., Cui, X., Liu, X., Chen, J., Chen, X., Cao, X., 2018. Detection of root orientation using ground-penetrating radar. IEEE Transactions on Geoscience and Remote Sensing 56, 93-104.

Liu, Q.H., Fan, G.X., 1999. Simulations of GPR in dispersive media using a frequency-dependent PSTD algorithm. IEEE Transactions on Geoscience and Remote Sensing 37, 2317-2324.

Liu, R., Xu, Y., Chen, R., Zhao, J., Xu, X., 2023. An Improved Hyperbolic Method and Its Application to Property Inversion in Martian Tianwen-1 GPR Data. IEEE Transactions on Geoscience and Remote Sensing 61.

Liu, T., Klotzsche, A., Pondkule, M., Vereecken, H., Su, Y., Van Der Kruk, J., 2018. Radius estimation of subsurface cylindrical objects from ground-penetrating-radar data using full-waveform inversion. Geophysics 83, H43-H54.

Loizos, A., Plati, C., 2007. Accuracy of pavement thicknesses estimation using different ground penetrating radar analysis approaches. NDT & e International 40, 147-157.

Lowrie, W., Fichtner, A., 2020. Fundamentals of geophysics. Cambridge university press.

Luo, T.X., Lai, W.W., Chang, R.K., Goodman, D., 2019. GPR imaging criteria. Journal of Applied Geophysics 165, 37-48.

Matriche, Y., Feliachi, M., Zaoui, A., Abdellah, M., 2014. FDTD and improved PSO methods of coupling for identification and localization of buried objects using GPR B-scan response. International Journal of Remote Sensing 35, 7499-7518.

Miccinesi, L., Beni, A., Monchetti, S., Betti, M., Borri, C., Pieraccini, M., 2021. Ground penetrating radar survey of the floor of the Accademia gallery (Florence, Italy). Remote Sensing 13, 1273.

Mirjalili, S., Mirjalili, S.M., Hatamlou, A., 2016. Multi-Verse Optimizer: a nature-inspired algorithm for global optimization. Neural Computing and Applications 27, 495-513.

Mott, N.F., 1936. The electrical conductivity of transition metals. Proceedings of the Royal Society of London. Series A-Mathematical and Physical Sciences 153, 699-717.

Ni, S.-H., Huang, Y.-H., Lo, K.-F., Lin, D.-C., 2010. Buried pipe detection by ground penetrating radar using the discrete wavelet transform. Computers and Geotechnics 37, 440-448.

Osumi, N., Ueno, K., 1985. Microwave holographic imaging of underground objects. IEEE Transactions on Antennas and Propagation 33, 152-159.

Paola, F., Friedrich, R., 2003. Frequency domain analysis of the polarimetric ground-penetrating radar response of landmines and minelike targets, Proc.SPIE, pp. 437-447.

Patsia, O., Giannopoulos, A., Giannakis, I., 2023a. Background Removal, Velocity Estimation, and Reverse-Time Migration: A Complete GPR Processing Pipeline Based on Machine Learning. IEEE Transactions on Geoscience and Remote Sensing, 1-1.

Patsia, O., Giannopoulos, A., Giannakis, I., 2023b. GPR Full-Waveform Inversion With Deep-Learning Forward Modeling: A Case Study From Non-Destructive Testing. IEEE Transactions on Geoscience and Remote Sensing 61.

Parkinson, G., Ékes, C., 2008. Ground penetrating radar evaluation of concrete tunnel linings, 12th International Conference on Ground Penetrating Radar. University of Birmingham Birmingham.

Parrillo, R., Roberts, R., Haggan, A., 2006. Bridge deck condition assessment using ground penetrating radar, ECNDT Conference Proceeding, Berlin, Germany, pp. 25-29.

Pérez-Gracia, V., González-Drigo, R., Di Capua, D., 2008. Horizontal resolution in a non-destructive shallow GPR survey: An experimental evaluation. NDT & E International 41, 611-620.

Pérez, J.P.A., Pueyo, S.C., López, B.C., 2011. Automatic gain control. Springer.

Persico, R., Leucci, G., Matera, L., de Giorgi, L., Soldovieri, F., Cataldo, A., Cannazza, G., De Benedetto, E., 2015. Effect of the height of the observation line on the the diffraction curve in GPR prospecting. Near Surface Geophysics 13, 243-252.

Pitt, D., Levine, N., Yan, X., 1999. Unity of objective, diversity of approach: deregulatory telecom developments in Hong Kong and China. IEEE Communications Magazine 37, 100-105.

Pollock, D.G., Dupuis, K.J., Lacour, B., Olsen, K.R., 2008. Detection of voids in prestressed concrete bridges using thermal imaging and ground-penetrating radar. Washington State Transportation Center (TRAC).

Puntu, J.M., Chang, P.-Y., Lin, D.-J., Amania, H.H., Doyoro, Y.G., 2021. A comprehensive evaluation for the tunnel conditions with ground penetrating radar measurements. Remote Sensing 13, 4250.

Ramírez-Nicolás, M., Sanchez-Cano, B., Witasse, O., Blelly, P.-L., Vázquez, L., Lester, M., 2016. The effect of the induced magnetic field on the electron density vertical profile of the Mars′ ionosphere: A Mars Express MARSIS radar data analysis and interpretation, a case study. Planetary and Space Science 126, 49-62.

Ramírez-Blanco, M., García-García, F., Rodríguez-Abad, I., Martínez-Sala, R., Benlloch, J., 2008. Ground-penetrating radar survey for subfloor mapping and analysis of structural damage in the Sagrado Corazón de Jesús Church, Spain. Archaeological prospection 15, 285-292.

Rappaport, C.M., 2007. Accurate Determination of Underground GPR Wavefront and B-Scan Shape From Above-Ground Point Sources. IEEE Transactions on Geoscience and Remote Sensing 45, 2429-2434.

Reynolds, J.M., 2011. An introduction to applied and environmental geophysics. John Wiley & Sons.

Ristić, A., Govedarica, M., Pajewski, L., Vrtunski, M., Bugarinović, Ž., 2020. Using ground penetrating radar to reveal hidden archaeology: The case study of the Württemberg-Stambol Gate in Belgrade (Serbia). Sensors 20, 607.

Ryu, H.-H., Bae, J.-Y., Song, K.-I., Lee, S.-Y., 2023. Characterizing Multichannel Conduit Signal Properties Using a Ground Penetrating Radar: An FDTD Analysis Approach. Journal of The Korean Geotechnical Society 39, 75-91.

Saarenketo, T., Scullion, T., 2000. Road evaluation with ground penetrating radar. Journal of applied geophysics 43, 119-138.

Sagnard, F., 2017. Development of data processing tools for the analysis of radargrams in utility detection using ground penetrating radar. Journal of Telecommunications and Information Technology 2017, 55-68.

Sagnard, F., Tarel, J.P., 2016. Template-matching based detection of hyperbolas in ground-penetrating radargrams for buried utilities. Journal of Geophysics and Engineering 13, 491-504.

Schneider, W.A., 1984. The common depth point stack. Proceedings of the IEEE 72, 1238-1254.

Seol, S.J., Kim, J.H., Song, Y., Chung, S.H., 2001. Finding the strike direction of fractures using GPR. 49, 300-308.

Sham, J.F., Lai, W.W., 2016a. Development of a new algorithm for accurate estimation of GPR's wave propagation velocity by common-offset survey method. NDT & E International 83, 104-113.

Sham, J.F.C., Lai, W.W.L., 2016b. Development of a new algorithm for accurate estimation of GPR's wave propagation velocity by common-offset survey method. NDT & E International 83, 104-113.

Shen, H., Yan, Y., Li, X., Wan, X., Li, Q., Li, Y., 2019. Enhancement of GPR diffracted waves processing: A case study from Taiyuan, China. Journal of Environmental and Engineering Geophysics 24, 237-247.

Shihab, S., Al-Nuaimy, W., 2005. Radius estimation for cylindrical objects detected by ground penetrating radar. Subsurface Sensing Technologies and Applications 6, 151-166.

Tanikawa, T., Hirano, Y., Dannoura, M., Yamase, K., Aono, K., Ishii, M., Igarashi, T., Ikeno, H., Kanazawa, Y., 2013. Root orientation can affect detection accuracy of ground-penetrating radar. Plant and Soil 373, 317-327.

ter Huurne, R.B., Olde Scholtenhuis, L.L., Dorée, A.G., van Oers, B., 2024. Using formative interventions to study emerging technologies in construction practices: the case of the Ground Penetrating Radar. Construction Management and Economics, 1-20.

Tong, L.F.J., 2013. An empirical study of factors driving complaint behavior intentions of retail-customers in the Hong Kong telecommunications services industry. The University of Newcastle.

Travassos, X., Avila, S., Adriano, R.d.S., Ida, N., 2018. A review of ground penetrating radar antenna design and optimization. Journal of microwaves, optoelectronics and electromagnetic applications 17, 385-402.

Tsung-Hsien, L., Mendel, J.M., 1998. Azimuth and elevation direction finding using arbitrary array geometries. IEEE Transactions on Signal Processing 46, 2061-2065.

Wallace, M., Ng, K., 2016. Development and application of underground space use in Hong Kong. Tunnelling and Underground Space Technology 55, 257-279.

Wan, S.K., Kumaraswamy, M.M., Liu, D.T., 2009. Contributors to construction debris from electrical and mechanical work in Hong Kong infrastructure projects. Journal of Construction Engineering and Management 135, 637-646.

Wang, M., Wen, J., Li, W., 2020. Qualitative research: The impact of root orientation coarse roots detection using ground-penetrating radar (GPR). BioResources 15, 2237-2257.

Wang, S., Zhao, S., Al-Qadi, I.L., 2018. Continuous real-time monitoring of flexible pavement layer density and thickness using ground penetrating radar. NDT & E International 100, 48-54.

Warren, C., Giannopoulos, A., Giannakis, I., 2016. gprMax: Open source software to simulate electromagnetic wave propagation for Ground Penetrating Radar. Computer Physics Communications 209, 163-170.

Willet, D.A., Rister, B., 2002. Ground penetrating radar: pavement layer thickness evaluation. University of Kentucky Transportation Center.

Wunderlich, T., Wilken, D., Majchczack, B.S., Segschneider, M., Rabbel, W., 2022. Hyperbola Detection with RetinaNet and Comparison of Hyperbola Fitting Methods in GPR Data from an Archaeological Site. Remote Sensing 14.

Xie, F., 2021. Unified uncertainty models for depth estimation of objects in ground penetrating radar survey.

Xie, F., Lai, W.W.L., Dérobert, X., 2021a. GPR-based depth measurement of buried objects based on constrained least-square (CLS) fitting method of reflections. Measurement 168, 108330.

Xie, F., Lai, W.W.L., Dérobert, X., 2021b. GPR uncertainty modelling and analysis of object depth based on constrained least squares. Measurement: Journal of the International Measurement Confederation 183.

Xie, F., Lai, W.W.L., Dérobert, X., 2022. Building simplified uncertainty models of object depth measurement by ground penetrating radar. Tunnelling and Underground Space Technology 123, 104402.

Xie, F., Wu, C.G.-W., Lai, W.W.-L., Sham, J.F.-C., 2018. Correction of multi-frequency GPR wave velocity with distorted hyperbolic reflections from GPR surveys of underground utilities. Tunnelling and Underground Space Technology 76, 76-91.

Xu, X., Xia, T., Venkatachalam, A., Huston, D., 2013. Development of high-speed ultrawideband ground-penetrating radar for rebar detection. Journal of Engineering Mechanics 139, 272-285.

Yee, K., 1966. Numerical solution of initial boundary value problems involving Maxwell's equations in isotropic media. IEEE transactions on antennas and propagation, 14, 302-307.

Yelf, R., 2004. Where is true time zero?, Proceedings of the Tenth International Conference on Grounds Penetrating Radar, 2004. GPR 2004. IEEE, pp. 279-282.

Yilmaz, Ö., 2001. Seismic data analysis: Processing, inversion, and interpretation of seismic data. Society of exploration geophysicists.

Yuan, C., Cai, H., 2020. Spatial reasoning mechanism to enable automated adaptive trajectory planning in ground penetrating radar survey. Automation in Construction 114.

Yue, D.P.T., Tang, S.L., 2011. Sustainable strategies on water supply management in Hong Kong. Water and Environment Journal 25, 192-199.

Zajc, M., Grebenc, A., 2023. Using Ground Penetrating Radar (GPR) for detecting a crypt beneath a paved church floor. Geologija 66, 275-283.

Zhang, J., Lu, Y., Yang, Z., Zhu, X., Zheng, T., Liu, X., Tian, Y., Li, W., 2022. Recognition of void defects in airport runways using ground-penetrating radar and shallow CNN. Automation in Construction 138, 104260.

Zhang, L., Li, J., Zeng, Z., Xu, Y., Liu, C., Chen, S., 2020. Stratigraphy of the Von Kármán Crater Based on Chang'E-4 Lunar Penetrating Radar Data. Geophysical Research Letters 47, e2020GL088680.

Zhang, P., Guo, X., Muhammat, N., Wang, X., 2016. Research on probing and predicting the diameter of an underground pipeline by GPR during an operation period. Tunnelling and Underground Space Technology 58, 99-108.

Zhang, X., Han, L., Robinson, M., Gallagher, A., 2021. A Gans-Based Deep Learning Framework for Automatic Subsurface Object Recognition from Ground Penetrating Radar Data. IEEE Access 9, 39009-39018.

Zhao, S., Al-Qadi, I.L., 2016. Development of an analytic approach utilizing the extended common midpoint method to estimate asphalt pavement thickness with 3-D ground-penetrating radar. NDT & E International 78, 29-36.

Zhou, X., Chen, Q., Lyu, S., Chen, H., 2022. Ellipse Inversion Model for Estimating the Orientation and Radius of Pipes From GPR Image. IEEE Journal of Selected Topics in Applied Earth Observations and Remote Sensing 15, 8299-8308.

Zhu, H., Huang, M., Zhang, Q.B., 2024. TunGPR: Enhancing data-driven maintenance for tunnel linings through synthetic datasets, deep learning and BIM. Tunnelling and Underground Space Technology 145.